

Report PME-FM-89-1 ✓

4
FILE COPY

AD-A215 378

**INFLUENCE OF WALL STRAIN RATE, POLYMER CONCENTRATION
AND CHANNEL HEIGHT UPON DRAG REDUCTION AND
TURBULENT STRUCTURE**

Kenneth J. Harder and William G. Tiederman
School of Mechanical Engineering
Purdue University
West Lafayette, Indiana 47907

November, 1989

Technical Report for Period 01 December 1980 - 30 November 1989

Approved for public release; distribution unlimited

Prepared for

OFFICE OF NAVAL RESEARCH
800 North Quincy Street
Arlington, VA 22217-5000

DTIC
ELECTE
DEC 04 1989
S B D

REPORT DOCUMENTATION PAGE		READ INSTRUCTIONS BEFORE COMPLETING FORM
1. REPORT NUMBER PME-FM-89-1	2. GOVT ACCESSION NO.	3. RECIPIENT'S CATALOG NUMBER
4. TITLE (and Subtitle) Influence of Wall Strain Rate, Polymer Concentration and Channel Height Upon Drag Reduction and Turbulent Structure		5. TYPE OF REPORT & PERIOD COVERED Technical Report for Dec. 1, 1988 through Nov. 30, 1989
7. AUTHOR(s) Kenneth J. Harder, William G. Tiederman		6. PERFORMING ORG. REPORT NUMBER
8. CONTRACT OR GRANT NUMBER(s) N00014-83K-0183		10. PROGRAM ELEMENT, PROJECT, TASK AREA & WORK UNIT NUMBERS 4322-754
9. PERFORMING ORGANIZATION NAME AND ADDRESS School of Mechanical Engineering Purdue University West Lafayette, Indiana 47907		11. CONTROLLING OFFICE NAME AND ADDRESS Office of Naval Research 800 North Quincy Street Arlington, VA 22217-5000
14. MONITORING AGENCY NAME & ADDRESS (if different from Controlling Office)		12. REPORT DATE November 1989
		13. NUMBER OF PAGES 115
		15. SECURITY CLASS. (of this report)
		15a. DECLASSIFICATION/DOWNGRADING SCHEDULE
16. DISTRIBUTION STATEMENT (of this Report) APPROVED FOR PUBLIC RELEASE: DISTRIBUTION UNLIMITED		
17. DISTRIBUTION STATEMENT (of the abstract entered in Block 20, if different from Report)		
18. SUPPLEMENTARY NOTES		
19. KEY WORDS (Continue on reverse side if necessary and identify by block number) Drag reduction; turbulent wall flows		
20. ABSTRACT (Continue on reverse side if necessary and identify by block number) This study investigated fully developed, low polymer concentration, drag-reduced flows in two dimensional channels. Water flows at equal wall shear stress were also measured for comparison with the drag-reduced flows. The first objective of this study was to determine the dependence of drag reduction and turbulent structure upon wall strain rate, average polymer concentration and channel height. The second objective was to test a scale-up procedure for predicting drag reduction in one channel based on results in another channel. A two-level factorial design was		

used to model the effect of wall strain rate and polymer concentration on drag reduction. The wall strain rate varied from 1000 to 4000 s^{-1} and the average polymer concentration varied from 3 to 5 ppm. Experiments were conducted in two channels with aspect ratios of 10. The distance between the large walls (channel height) was 2.5 and 6.0 cm. Since it was not possible to attain high shear rates in the 6.0 cm channel the effect of channel height was determined only for the lowest wall shear rate. A two-component laser velocimeter was used to measure the turbulent structure and pressure drop measurements were used to determine the amount of drag reduction.

For the low polymer concentrations used in this study, drag reduction of up to 40% was attained. Drag reduction was shown to depend upon wall strain rate, polymer concentration, and channel height. However, none of the turbulent structure quantities showed a similar dependence. These quantities were found to depend only on the amount of drag reduction. The slope and intercept of the mean velocity profile changed with drag reduction. Because the slope of the mean velocity profile changed, the scale-up method did not work. The level of the RMS of the fluctuating streamwise velocity increased in drag-reduced flows while the RMS of the fluctuating normal velocity decreased. The production of the streamwise normal stress and the Reynolds shear stress decreased in drag-reduced flows. This indicates that the pressure-strain correlation may be affected by polymers. Measurements of the average period of the turbulence production cycle confirms that the ratio of the average period of the production cycle for a drag-reduced flow to the average period for a water flow at equal wall shear stress increases with drag reduction in a manner similar to the increase in streak spacing. For most drag-reduced flows, the Reynolds shear stress levels were unaffected. However, in one case, the level of the Reynolds shear stress decreased drastically in the near-wall region indicating the presence of some additional terms in the momentum balance that were not present in the other flows. The low threshold uv motions were damped in drag-reduced flows while the high threshold motions were unaffected.

TABLE OF CONTENTS

	Page
LIST OF TABLES	iv
LIST OF FIGURES	v
LIST OF SYMBOLS	xi
CHAPTER 1 - INTRODUCTION	1
CHAPTER 2 - APPARATUS AND PROCEDURE	7
2.1 Experimental Facilities	7
2.2 Polymer Solution Preparation	9
2.3 Drag Reduction Measurement	10
2.4 Laser Velocimeter	11
2.5 Data Acquisition	14
2.6 Data Analysis	15
2.7 Factorial Design	17
2.8 Burst Detection Analysis	20
CHAPTER 3 - RESULTS	23
3.1 Effect of Wall Strain Rate and Polymer Concentration on Drag Reduction	23
3.2 Evaluation of Shear Velocity	27
3.3 Water Flow	30
3.4 Drag-Reduced Flow Results	46
3.5 Turbulent Burst Structure	70
CHAPTER 4 - RECAPITULATION AND CONCLUSIONS	81
REFERENCES	86
APPENDIX	89

Accession For	
NTIS	<input checked="" type="checkbox"/>
DTIC TAB	<input type="checkbox"/>
Unannounced	<input type="checkbox"/>
Justification	
By	
Distribution/	
Availability Codes	
Dist	Avail and/or Special
A-1	

LIST OF TABLES

Table	Page
2.1. Typical LDV parameters.	13
2.2. Experimental conditions for the factorial design	20
3.1. Parameters for the log law, $U^+ = \frac{1}{\kappa} \ln y^+ + B$	50

LIST OF FIGURES

Figure	Page
2.1. Schematic of the flow loop.	8
2.2. Factorial design space; o, linear design points; x, additional points for quadratic design.	19
2.3. Probability distribution for the grouping parameter	21
3.1. Dependence of drag reduction upon wall strain rate and polymer concentration; linear model: italicized numbers, 6.0 cm channel results; other, 2.5 cm channel results.	24
3.2. Dependence of drag reduction upon wall strain rate and polymer concentration; quadratic model: italicized numbers, 6.0 cm channel results; other, 2.5 cm channel results.	26
3.3. Effect of Reynolds number on the local to average shear stress ratio.	28
3.4. Estimated shear velocity for water flow, $\frac{d\bar{U}}{dy} \Big _w = 1000 \text{ s}^{-1}$, 2.5 cm channel: * , u_τ ; +, viscous contribution; O turbulent contribution; =====, 95% confidence interval; —, u_τ mean.	29
3.5. Mean velocity profiles for water flows: a) 2.5 cm channel, $Re_h = 14,430$; b) 2.5 cm channel, $Re_h = 20,260$; c) 2.5 cm channel, $Re_h = 30,420$; d) 6.0 cm channel, $Re_h = 34,640$	32
3.6. Root-mean-square velocity fluctuation profiles for water flows: +, 2.5 cm channel, $Re_h = 14,430$; o, 2.5 cm channel, $Re_h = 20,260$; x, 2.5 cm channel, $Re_h = 30,420$; * , 6.0 cm channel, $Re_h = 34,640$; —, Walker (1988).	33
3.7. Near-wall behavior of the root-mean-square velocities: +, 2.5 cm channel, $Re_h = 14,430$; o, 2.5 cm channel, $Re_h = 20,260$; x, 2.5 cm channel, $Re_h = 30,420$; * , 6.0 cm channel, $Re_h = 34,640$; —, Kreplin and Eckelmann (1979); - - -, $v'^+ = 0.005 y^{+2}$ (Finnicum and Hanratty, 1985).	35

Figure	Page
3.8. Turbulence intensity profiles: +, 2.5 cm channel, $Re_h = 14,430$; o, 2.5 cm channel, $Re_h = 20,260$; x, 2.5 cm channel, $Re_h = 30,420$; *, 6.0 cm channel, $Re_h = 34,640$	36
3.9. Reynolds shear stress variation, 2.5 cm channel, $Re_h = 14,430$; *, Reynolds stress; —, $\tau_w^*(1-y/a)$	37
3.10. Near-wall behavior of the Reynolds stresses: +, 2.5 cm channel, $Re_h = 14,430$; o, 2.5 cm channel, $Re_h = 20,260$; x, 2.5 cm channel, $Re_h = 30,420$; *, 6.0 cm channel, $Re_h = 34,640$	38
3.11. Near-wall behavior of the Reynolds stresses with calculated value from Equation 3.8: a) 2.5 cm channel, $Re_h = 14,430$; b) 2.5 cm channel, $Re_h = 20,260$; c) 2.5 cm channel, $Re_h = 30,420$; d) 6.0 cm channel, $Re_h = 34,640$; o, experimental data; — from Equation 3.7.	40
3.12. Correlation coefficient profiles: +, 2.5 cm channel, $Re_h = 14,430$; o, 2.5 cm channel, $Re_h = 20,260$; x, 2.5 cm channel, $Re_h = 30,420$; *, 6.0 cm channel, $Re_h = 34,640$	41
3.13. $\overline{u^2}$ production profiles for water flows: a) 2.5 cm channel, $Re_h = 14,430$; b) 2.5 cm channel, $Re_h = 20,260$; c) 2.5 cm channel, $Re_h = 30,420$; d) 2.5 cm channel, $Re_h = 34,640$; —, \overline{uv} from Equation 3.7.	45
3.14. \overline{uv} production profiles for water flow: +, 2.5 cm channel, $Re_h = 14,430$; o, 2.5 cm channel, $Re_h = 20,260$; *, 6.0 cm channel, $Re_h = 34,640$	47
3.15. Mean velocity profiles: a) typical drag-reduced flow; b) strongly non-Newtonian drag-reduced flow; *, drag-reduced data; +, water flow data at equal wall shear; —, standard law of the wall; ---, fitted law of the wall; -.-, Virk ultimate asymptote.	49
3.16. Dependence of the reciprocal of the log-law slope on drag reduction.	51
3.17. Root-mean-square velocities: a) typical drag-reduced case; b) strongly non-Newtonian drag-reduced case; *, u'^+ ; +, v'^+ ; —, water flow at equal τ_w	53
3.18. y^+ for peak in u' , 2.5 cm channel results only.	54
3.19. Variation of peak location for u'^+ as a function of drag reduction.	55
3.20. Reynolds shear stress distribution: *, typical drag-reduced flow; ---, water flow at equal wall shear stress; —, $\tau_w^*(1-y/a)$	56

Figure	Page
3.21. Difference in the shear stress as estimated by the sum of the viscous and Reynolds stresses and the streamwise pressure gradient for strongly non-Newtonian flow case: o, Reynolds shear stress; +, sum of Reynolds and viscous shear stresses; —, estimated $\tau_w^+(1-y/a)$	58
3.22. Correlation coefficient distribution: a) typical drag-reduced flow ; b) strongly non-Newtonian drag-reduced flow; +, drag-reduced; —, water flow at equal τ_w	59
3.23. $\overline{u^2}$ production for typical drag-reduced flow: * , experimental results; — — —, results obtained from calculating \overline{uv} from Equation 3.7	61
3.24. $\overline{u^2}$ production profiles for typical drag-reduced flow and water flow at equal τ_w : * , drag-reduced flow; —, water flow.	62
3.25. y^+ location for peak in $\overline{uv} \frac{d\overline{U}}{dy}$, 2.5 cm channel results only.	63
3.26. y^+ location of the peak value of $\overline{uv} \frac{d\overline{U}}{dy}$ as a function of drag reduction.	64
3.27. Variation of integrated production profiles with Reynolds number: +, water flow; o, drag-reduced flow; — — —, $1.3 \pm 15\%$ at 95% confidence.	66
3.28. Variation of integrated production profiles with drag reduction.	67
3.29. \overline{uv} production profiles.	69
3.30. Typical mean burst period as a function of threshold; 2.5 cm channel, $\left. \frac{d\overline{U}}{dy} \right _w = 1000 \text{ s}^{-1}$, $\overline{C} = 3 \text{ ppm}$	73
3.31. Burst period for water flow with inner scaling as a function of Reynolds number.	74
3.32. Variation in the ratio of the average burst period in a drag-reduced flow to the average burst period in a water flow at equal τ_w	76
3.33. Variation in the ratio of the average burst period in a drag-reduced flow to the average burst period in a water flow at equal wall shear stress as a function of the design variables.	77

Figure	Page
3.34. Probability density for the rate of occurrence of quadrant 2 events as a function of threshold: * , water flow, $\frac{d\bar{U}}{dy} \Big _w = 2500 \text{ s}^{-1}$; +, 4 ppm drag-reduced flow at equal wall shear stress; $y^+ = 40$ for both flows.	78
3.35. Probability density for the rate of occurrence of quadrant 4 events as a function of threshold: * , water flow, $\frac{d\bar{U}}{dy} \Big _w = 2500 \text{ s}^{-1}$; +, 4 ppm drag-reduced flow at equal wall shear stress; $y^+ = 40$ for both flows.	79
Appendix	
Figure	
A.1. Mean velocity profiles for 6.0 cm channel, $\frac{d\bar{U}}{dy} \Big _w = 1000 \text{ s}^{-1}$: a) 5 ppm polymer flow; b) 3 ppm polymer flow; +, water flow at equal τ_w	96
A.2. Mean velocity profiles for 2.5 cm channel: a) $\frac{d\bar{U}}{dy} \Big _w = 1000 \text{ s}^{-1}$, 5 ppm polymer flow; b) $\frac{d\bar{U}}{dy} \Big _w = 2500 \text{ s}^{-1}$, 4 ppm polymer flow; +, water flow at equal τ_w	97
A.3. Mean velocity profiles for 2.5 cm channel: $\frac{d\bar{U}}{dy} \Big _w = 4000 \text{ s}^{-1}$, 3 ppm polymer flow; +, water flow at equal τ_w	98
A.4. RMS velocity profiles for 6.0 cm channel, $\frac{d\bar{U}}{dy} \Big _w = 1000 \text{ s}^{-1}$: a) 5 ppm polymer flow; b) 3 ppm polymer flow; —, water flow at equal τ_w	99
A.5. RMS velocity profiles for 2.5 cm channel: a) $\frac{d\bar{U}}{dy} \Big _w = 1000 \text{ s}^{-1}$, 5 ppm polymer flow; b) $\frac{d\bar{U}}{dy} \Big _w = 2500 \text{ s}^{-1}$, 4 ppm polymer flow; —, water flow at equal τ_w	100
A.6. RMS velocity profiles for 2.5 cm channel: $\frac{d\bar{U}}{dy} \Big _w = 4000 \text{ s}^{-1}$, 3 ppm polymer flow; —, water flow at equal τ_w	101

Appendix Figure	Page
A.7. Reynolds shear stress profiles for 6.0 cm channel, $\frac{d\bar{U}}{dy} \Big _w = 1000 \text{ s}^{-1}$: a) 5 ppm polymer flow; b) 3 ppm polymer flow; c) water flow.	102
A.8. Reynolds shear stress profiles for 2.5 cm channel: a) $\frac{d\bar{U}}{dy} \Big _w = 1000 \text{ s}^{-1}$, 5 ppm polymer flow; b,c) $\frac{d\bar{U}}{dy} \Big _w = 2500 \text{ s}^{-1}$; 4 ppm polymer flow, water flow, respectively.	103
A.9. Reynolds shear stress profiles for 2.5 cm channel, $\frac{d\bar{U}}{dy} \Big _w = 4000 \text{ s}^{-1}$: a) 3 ppm polymer flow; b) water flow.	104
A.10. Shear velocity profiles for 6.0 cm channel, $\frac{d\bar{U}}{dy} \Big _w = 1000 \text{ s}^{-1}$: a) 5 ppm polymer flow; b) 3 ppm polymer flow; c) water flow.	105
A.11. Shear velocity profiles for 2.5 cm channel: a) $\frac{d\bar{U}}{dy} \Big _w = 1000 \text{ s}^{-1}$, 5 ppm polymer flow; b,c) $\frac{d\bar{U}}{dy} \Big _w = 2500 \text{ s}^{-1}$; 4 ppm polymer flow, water flow, respectively.	106
A.12. Shear velocity profiles for 2.5 cm channel, $\frac{d\bar{U}}{dy} \Big _w = 4000 \text{ s}^{-1}$: a) 3 ppm polymer flow; b) water flow.	107
A.13. Correlation coefficient profiles for 6.0 cm channel: a) $\frac{d\bar{U}}{dy} \Big _w = 1000 \text{ s}^{-1}$, 5 ppm polymer flow; b) 3 ppm polymer flow; —, water flow at equal τ_w	108
A.14. Correlation coefficient profiles for 2.5 cm channel: a) $\frac{d\bar{U}}{dy} \Big _w = 1000 \text{ s}^{-1}$, 5 ppm polymer flow; b) $\frac{d\bar{U}}{dy} \Big _w = 2500 \text{ s}^{-1}$, 4 ppm polymer flow; —, water flow at equal τ_w	109
A.15. Correlation coefficient profiles for 2.5 cm channel, $\frac{d\bar{U}}{dy} \Big _w = 4000 \text{ s}^{-1}$: +, 3 ppm polymer flow; —, water flow.	110

Appendix
Figure

Page

- A.16. $\overline{u^2}$ production profiles for 6.0 cm channel, $\frac{d\overline{U}}{dy}|_w = 1000 \text{ s}^{-1}$: a) 5 ppm polymer flow; b) 3 ppm polymer flow; —, water flow. 111
- A.17. $\overline{u^2}$ production profiles for 2.5 cm channel: a) $\frac{d\overline{U}}{dy}|_w = 1000 \text{ s}^{-1}$, 5 ppm polymer flow; b) $\frac{d\overline{U}}{dy}|_w = 2500 \text{ s}^{-1}$, 4 ppm polymer flow; —, water flow at equal τ_w 112
- A.18. $\overline{u^2}$ production profiles for 2.5 cm channel, $\frac{d\overline{U}}{dy}|_w = 4000 \text{ s}^{-1}$: *, 3 ppm polymer flow; —, water flow. 113

LIST OF SYMBOLS

Symbol	Description
A_{nn}	coefficients of proposed models
B	intercept of the law of the wall
\bar{C}	average polymer concentration
$DR, \%DR$	percent drag reduction
H	threshold for uv quadrant two detection technique
L	threshold for modified u level detection technique
ΔP_p	pressure drop in a polymer or drag-reduced flow
ΔP_w	pressure drop for a water flow
$\frac{\Delta P}{\Delta x}$	pressure gradient in the streamwise direction
Re_h	Reynolds number based on channel height and mass averaged velocity
R_{uv}	correlation coefficient for turbulent momentum transport, $R_{uv} = \overline{uv}/u'v'$
RMS	root mean square
\bar{T}_B	average period of the burst cycle
\bar{T}_{BP}	average period of the burst cycle for a polymer flow
\bar{T}_{BW}	average period of the burst cycle for a water flow
U, V	instantaneous velocities in the x and y directions respectively
U_{AVG}	mass-averaged velocity
U_o	center-line velocity
U_1, U_2	measured velocity components
X_1, X_2	normalized coordinates for factorial design
a	channel half-height

Symbol	Description
d_m	diameter of the laser velocimeter measurement volume
$\frac{d\bar{U}}{dy} \big _w$	wall strain rate
h	channel height
l_m	spanwise length of the laser velocimeter measurement volume
ppm	parts per million
r	correlation coefficient for proposed models
u, v	instantaneous velocity fluctuations in the x and y directions respectively: $u=U-\bar{U}$, $v=V-\bar{V}$
u_1, u_2	instantaneous fluctuations in the measured velocity components: $u_1=U_1-\bar{U}_1$, $u_2=U_2-\bar{U}_2$
u_τ	shear velocity, $u_\tau = \sqrt{\tau_w/\rho}$
x, y	streamwise and wall-normal directions, respectively
x_1, x_2	coordinate system for measured velocity components
\varnothing	liters
κ	von Karman constant in the law of the wall
λ	streak spacing
μ	dynamic viscosity
ν	kinematic viscosity
ρ	density
$\rho(N_i)$	probability density for rate of occurrence of quadrant i events
τ	shear stress
τ_w	wall shear stress
τ_w^*	wall shear stress calculated from addition of viscous and Reynolds stresses
$\left[\tau_w \right]_{2D}$	wall shear stress calculated from pressure drop for infinite aspect ratio two-dimensional channel
θ	angle velocity components measured relative to the flow direction

Symbol	Description
	Superscripts
+	normalized with inner variables u_τ and v
-	time average
'	root mean square (RMS)

CHAPTER 1 - INTRODUCTION

Over the past several decades, the phenomenon of drag reduction has received much attention. Drag reduction is of interest to those in industrial and military circles. For example, by reducing drag in piping networks, an industrial plant can reduce the cost of pumping. From a military standpoint, drag-reduced ships require less work from the propeller, saving energy and reducing noise. In the scientific community, the phenomenon of drag reduction allows experimenters to observe changes in the turbulence structure and from observing these changes, it is hoped that the nature of turbulent flows can be better understood. There are several methods in which drag reduction can be obtained. Savill and Mumford (1988) installed flat plates, called Large Eddy Break-Up devices (LEBUs), in a boundary layer and obtained drag reduction on the surface below it. These LEBUs are thought to reduce drag by interfering with the interaction of the outer flow with the inner flow. Hershey et al. (1975) have shown that surfactants are effective drag reducers. Walsh and Weinstein (1979) measured less drag on ribbed surfaces than on a surface without ribs under the same flow conditions. Bewersdorf (1984) injected a high concentration polymer thread down the center of a pipe and observed significant drag reduction. In Bewersdorf's (1984) experiment, the polymer thread never fully mixed with the solvent (heterogeneous flow). Reischman and Tiederman (1975) showed that a well mixed (homogeneous) polymer solution also

yielded substantial drag reduction. This study will focus on drag reduction in the flow of a homogeneous, dilute polymer solution.

From experiments in a pipe, Wells and Spangler (1967) found that the polymer must be in the near-wall region for drag reduction to occur. Wu and Tulin (1972) obtained similar results by injecting polymer in their flat plate boundary layer. Tiederman et al. (1985) showed that when polymer is confined to the viscous sublayer, no drag reduction occurs and, therefore, the viscous sublayer plays a passive role in the interaction of the inner and outer parts of a turbulent boundary layer. McComb and Rabie (1982) also found that drag reduction occurs only when polymer is present in the buffer zone of the pipe.

The studies of Corino and Brodkey (1969) and Kim et al. (1971) found that most of the turbulent kinetic energy generation and turbulent transport occur during the "burst-sweep" event. Coherent structures in the very near-wall region ($y^+ \leq 5$) called streaks move slowly downstream. At some point, these streaks begin to move away from the wall until at $y^+ \approx 15$ they oscillate and eject away from the wall. This ejection of fluid from the slow moving wall streak is called a "burst". The sweep event occurs when high-speed fluid from the outer flow rushes toward the wall and interacts with the slower fluid. It is thought that these burst and sweep events occur in a quasi-periodic manner. Because the burst event is quasi-periodic and occurs in the near-wall region where drag-reducing solutions have the greatest effect, experimenters have concentrated on measuring the statistical quantities associated with the burst event, particularly the average streak spacing and average burst period.

Oldaker and Tiederman (1977) demonstrated that the average streak spacing increased in a linear fashion with drag reduction for homogeneous drag-reduced flows. Luchik and Tiederman (1988) showed that the ratio of the average time between bursts increased with drag reduction in the same manner as the increase in the streak spacing. From this information, they deduced that the burst rate from a streak in a well mixed, low concentration, drag-reduced flow is equal to the burst rate from a water flow. For the case of the well mixed, low concentration, drag-reduced flow, Luchik and Tiederman (1988) also showed that only the small amplitude uv motions in quadrants two and four are damped.

Reischman and Tiederman (1975) found that the buffer zone was thickened in drag-reduced flows offsetting the logarithmic zone upward while the viscous sublayer thickness was not changed. Virk (1975) proposed that the slope and intercept of the logarithmic portion of the mean velocity profile will change until, at maximum drag reduction, the logarithmic zone disappears and the buffer zone extends to the centerline of the pipe.

The root-mean-square (RMS) of the streamwise and wall-normal velocities also show definite trends in drag-reduced flows. Reischman and Tiederman (1975) show that the streamwise RMS velocity (u') level increases throughout the entire boundary layer. The peak in u' also moves outward in both physical and non-dimensional distance for a drag-reduced flow. Luchik and Tiederman (1988) and Willmarth et al. (1987) showed a decrease in both the physical and non-dimensional levels of the wall-normal RMS velocity in the inner region of a drag-reduced flow.

Luchik and Tiederman (1988) also found that for a drag-reduced flow, the peak in the Reynolds shear stress, \overline{uv} , moved away from the wall and was broader in extent than that of a water flow at equal wall shear stress. Willmarth et al. (1987), however, found that for $y^+ < 200$, \overline{uv} was decreased significantly from the Newtonian value such that the sum of the viscous and Reynolds shear stress no longer added up to the shear stress as deduced from the momentum equation. Therefore, they proposed the existence of an additional retarding force in a polymer flow. The experiments of Willmarth et al. (1987) and Luchik and Tiederman (1988) were homogeneous, low concentration polymer flows. Bewersdorf (1984) saw results similar to those of Willmarth et al. (1987) in a pipe flow where a very high concentration polymer solution was injected at the centerline. However, Bewersdorf (1984) did not have a well mixed solution at the measurement station. "Threads" of polymer were reported throughout the flow.

Since the polymer additives also affect heat transfer characteristics, velocity measurement devices such as hot-wire and hot-film probes will yield significant error if used in these flows. Because the laser Doppler velocimeter (LDV) is a non-invasive velocity sensor and unaffected by the polymer additives, it is the measurement device of choice in polymer flows. Most experimenters have measured only one component of velocity (the streamwise component) with the LDV system. Reischman and Tiederman (1975) reported measurements in a rectangular channel, McComb and Rabie (1982) and Bewersdorf (1984) reported streamwise velocity measurements in a pipe. More recently, Luchik and Tiederman (1988), Willmarth et al. (1987) and Walker (1988) reported two-component measurements in rectangular channels.

A primary goal of research in this field is to model the flow and thus be able to

predict various characteristics (i.e. drag reduction, bursting rate) given some flow condition or configuration. Granville (1985) proposed a method for predicting drag-reduction in one pipe based on results in another pipe. In this method, the slope of the logarithmic portion of the mean velocity is assumed to be constant. This assumption may or may not be valid as will be seen in a later section of this report. It is also not clear whether dependent variables are functions of several independent variables or simply the amount of drag reduction. For example, Luchik and Tiederman (1988) found that the ratio of the average burst period for a drag-reduced flow to the average burst period for a water flow at equal wall shear stress depends upon drag reduction. However, Walker et al. (1986), using a factorial design, found that drag reduction immediately downstream of the injectors (up to 30 channel heights) depends mainly upon injection flow rate and injection concentration.

Efforts to determine an appropriate set of dimensionless parameters that correlate dependent variables in drag-reducing flows have not yet been successful. The primary reason for this lack of success is the absence of rheological measurements and/or theory that accurately describe the elastic and elongational properties of dilute polymer solutions. Consequently the independent variables in this study will be dimensional.

In this study, turbulent flow in two channels of different height was investigated. The polymer was injected far enough upstream (greater than 30 channel heights) so that the polymer was well mixed at the measurement location. The flow was also fully developed at the measurement station. Since the well mixed polymer concentrations were very low (3-5 ppm), the shear viscosity for the drag-reduced flows and a water flow were essentially the same. The first objective of this study was to determine the dependence of drag reduction upon three independent variables. These variables are the

strain rate at the wall ($\left. \frac{d\bar{U}}{dy} \right|_w$), the average, well mixed polymer concentration in the channel (\bar{C}) and the channel height (h). The second objective was to determine if the changes in the turbulence structure depended upon these three variables or simply upon the amount of drag reduction. Finally, the third objective was to determine whether or not Granville's (1985) method of predicting drag reduction in a pipe could be extended to two-dimensional channel flow. In this study, the term "turbulence structure" refers to all statistical quantities of a turbulent flow (mean velocities, RMS velocities, turbulent stresses, etc.) and the turbulent burst structure quantities. A factorial design (discussed later) was used to determine the dependence of the quantities of interest upon wall strain rate and average polymer concentration. A laser Doppler velocimeter was used to make the velocity measurements.

Chapter two of this thesis contains information about the apparatus and experimental procedure used in this study. Chapter three contains the typical results for a drag-reduced flow and the corresponding water flows. The other drag-reduced flow results, which were necessary to establish trends are presented in the appendix. Chapter four recapitulates and shows conclusions drawn from the results.

CHAPTER 2 - APPARATUS AND PROCEDURE

2.1 Experimental Facilities

A recirculating water flow loop, shown schematically in Figure 2.1, was driven by up to four centrifugal pumps operating in parallel. A stilling tank at each end of the channel test sections isolated them from the hydrodynamic disturbances of the flow loop. The upstream tank contained a perforated plate and a screen-sponge-screen section downstream of the inlet to create a uniform flow entering the contraction at the outlet of the tank. The flow then entered a section containing closely packed drinking straws just upstream of the channel test sections. The downstream tank also contained a perforated plate for damping disturbances and a cooling coil to maintain constant temperature.

Two rectangular channels were used in this flow loop. The larger of the two channels was 6.0 cm high by 57.5 cm wide and was over one hundred channel heights long. Polymer solutions were injected through flush-mounted angled slots that were located over forty channel heights upstream of the test location. The smaller of the two channels was 2.5 cm high by 25 cm wide and was approximately one hundred and ninety channel heights long. The injection slots for this channel were located one hundred channel heights upstream of the test location. A removable contraction section

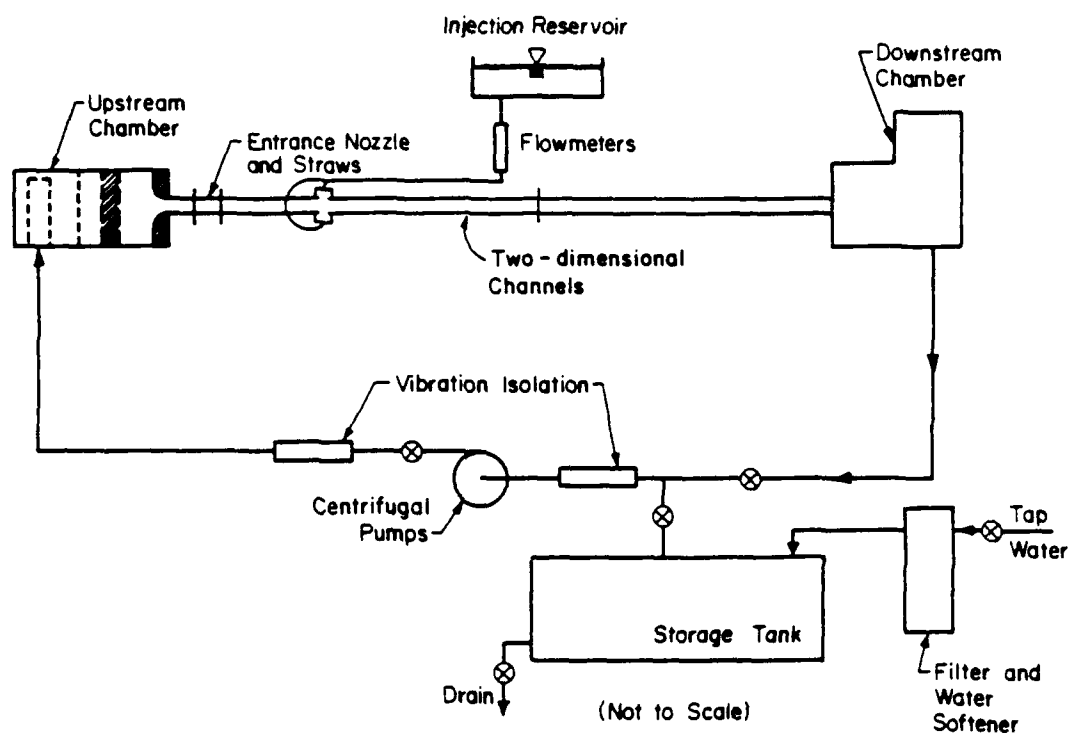


Figure 2.1. Schematic of the flow loop.

was inserted into the outlet of the upstream tank in order to reduce the flow area from 6.0 cm by 57.5 cm to 2.5 cm by 25 cm. For both channels, the polymer solution was injected far enough upstream so that the polymer solutions was well mixed with the channel water at the test locations.

2.2 Polymer Solution Preparation

Since a different batch of polymer was used for each experiment, it was necessary to employ standard procedures for making and testing each batch to ensure that the results were repeatable. The polymer used in this study was an aqueous solution of SEPARAN AP-273, a polyacrylimide manufactured by Dow Chemical. To prepare the polymer solution, the polymer powder was first suspended in 200–300 ml of isopropyl alcohol and then mixed in deaerated, filtered tap water at 38°C. This initial solution was allowed to hydrate for at least 12 hours before diluting to the desired concentration of 1000 ppm. This final mixture was then allowed to hydrate for another 12 hours.

Three repeatability checks were performed on each batch of polymer. The shear viscosity was checked on a Wells-Brookfield LVT-SCP3 cone and plate viscometer over a shear rate range of 11–115 s^{-1} . The pH of the polymer solutions as well as the tap water were also monitored for each batch. To test the drag reducing capability of each batch, a sample was diluted to 100 ppm and forced through a 1.405 cm ID pipe at various flowrates. Only batches that yielded consistent results were used in the channel flow experiments.

2.3 Drag Reduction Measurement

The amount of drag reduction for each experiment was determined from pressure drop measurements. The pressure drop was measured with a micromanometer that used carbon tetrachloride as the working fluid. Using this micromanometer, the sensitivity of the pressure drop measurements was 0.015 mm of water.

Before each experiment, the softened, filtered tap water was deaerated by partially closing a valve upstream of the pumps and circulating the water. The water would cavitate in the valve, forcing the air out of solution. The air then could be collected in and bled out of the upstream stilling tank. Pressure drop measurements were then taken at various locations in the channel to ensure that the flow was fully developed. Finally, the pressure drop measurements were used to determine the experimental flow conditions through the use of Dean's(1978) correlations.

Since the flow is fully developed and two dimensional at the test location, Dean (1978) recommends that the average shear stress should be calculated from

$$\left[\bar{\tau}_w \right]_{2D} = \frac{\Delta P}{\Delta x} a \quad (2.1)$$

where $\frac{\Delta P}{\Delta x}$ is the pressure drop over the streamwise distance Δx , $a = h/2$ and h is the channel height. The drag reduction was determined by,

$$DR = \frac{\Delta P_w - \Delta P_p}{\Delta P_w} \quad (2.2)$$

where ΔP_w is the pressure drop in water flow and ΔP_p is the pressure drop in a

polymer flow at equal Reynolds number. Once the polymer passed through the channel and was recirculated, it ceased to be a drag reducer. Luchik(1985) hypothesized that high shears in the pumps destroyed the polymer chains, thus destroying the drag reducing capability of the polymer.

2.4 Laser Velocimeter

2.4.1 Two component laser velocimeter

A three beam, two color laser Doppler velocimeter (LDV) was used to obtain two component velocity data. The LDV was a TSI model 9100-8 system that incorporated a Lexel model 85, 500 mW argon-ion laser. This three beam system consisted of one blue (488 nm), one green (514.5 nm), and one blue-green beam that contained both wavelengths. The blue and green beams were frequency shifted by 40 MHz by placing a single Bragg cell ahead of the dichroic color separator. Frequency shifting allows the system to measure flow reversals and eliminates the possibility of fringe biasing. The LDV also included electronic down mixing, 2.27x beam expansion and 250 mm focusing lens.

The standard 9100-8 system was modified (see Walker,1988) so that the blue-green beam was on the optical axis and the blue and green beams were at nominally ± 45 degrees. In this configuration, velocity components were measured at ± 45 degrees to the streamwise flow direction. The advantage of this configuration is that velocity measurements can be made very near the wall. A disadvantage of this technique is that the velocity components are measured in a plane parallel to the flow, but inclined at

about 3° in the spanwise direction. This introduces some error into quantities related to the normal velocity. However, as shown by Walker(1988), this error is negligible for $y^+ > 5$. The superscript "+" used here denotes scaling with the shear velocity u_τ and the kinematic viscosity ν .

The transmitting optics table was equipped with a traverse that allowed movement of the probe volume in the vertical direction. The traverse consisted of two enhanced aluminum mirrors, with the upper mirror and transmitting lens mounted on a vertical translation stage that was positioned by two, two-inch micrometers. The micrometers had a least count of 0.013 mm. The location of the probe volume in relation to the channel wall was determined by using a TSI model 9140 receiving optics assembly and a model 10096 eyepiece. By moving the probe volume towards the wall and observing (with the eyepiece) the bright spot created when it hit the wall, the location of the probe volume with respect to the wall could be determined to within 0.025 mm. See Table 2.1 for the relevant LDV parameters.

The receiving optics for this system were those of a standard TSI two component system. Scattered light was collected in the forward scatter mode using a 250 mm focal length lens. A 2.27x telescope was placed behind this lens to enhance spatial resolution. A TSI model 9143 field stop assembly with a 50 μm diameter aperture was used to ensure spatial coincidence of the two measured velocities and allow finer spatial resolution. Light passing through the aperture was passed through a color separator and collected by two photomultiplier tubes.

Table 2.1. Typical LDV parameters.

Beam	Blue	Green
half angle, degrees	2.51	2.78
fringe spacing, μm	5.58	5.31
nondimensional probe volume diameter, d_m^+	1.8-2.8	1.8-2.8
nondimensional probe volume length, l_m^+	10-15	10-15

In order to reduce the spanwise extent of the probe volume, the entire receiving optics assembly was rotated off the optical axis in the horizontal plane. Finer resolution was obtained by viewing the probe volume off axis, thus reducing its spanwise extent. The reduced spanwise length of the probe volume was essential in obtaining accurate data for the burst records.

The flow was seeded with homogenized whole milk which contains fat particles that are about $0.3 \mu\text{m}$ in diameter (George and Lumley 1973). The flow was seeded so that there would be only one particle in the probe volume at a time.

2.4.2 One component laser velocimeter

A one component LDV (TSI model 9100-6) was used for making burst record measurements in the three 4000 s^{-1} strain rate flows since high enough rates could not be achieved with the two component system. The one component system incorporated many of the same elements as the two component system, so the details will not be

discussed. The one component system used the green line (514.5 nm) of the argon-ion laser because it provided better signal quality than the blue line (488 nm). As with the two component system, off axis collection of the scattered light was implemented to reduce the spanwise extent of the probe volume. A 250 mm lens was used to focus and cross the beams. Since the one component system operated in the same configuration as the two component system, the parameters for the green line in Table 2.1 apply to the one component system. Details of the one component system can be found in the TSI 9100-6 manual.

2.5 Data Acquisition

Output from the photomultiplier tubes was high-pass filtered at 25 MHz to remove pedestal frequencies and was electronically down mixed to an effective shift frequency of 0.5 MHz by a TSI model 9186 down mixer. Each signal was then sent to a TSI model 1980 signal processor for further conditioning and frequency determination. The signals were high-pass filtered at 30 kHz and low-pass filtered at 1 MHz, creating a band pass equivalent to roughly ± 2.5 m/s for the two component system. A coincidence window ensured that data from both processors were from the same particle. A Masscomp 5520 computer acquired the data from a TSI model 1998 master interface. The data were sampled at equal time intervals ranging from 0.003 s to 0.01 s in order to remove velocity bias. Time-average statistics were calculated from records of 10,000 independent realizations.

2.6 Data Analysis

The calculation of the streamwise and normal velocities and their statistical quantities was the first task to be performed on the measured velocities. The one component data required little processing, since the measured velocity was the streamwise velocity. However, the two component velocity data needed further processing, since the measured velocities were not the streamwise and normal velocities. In order to make the necessary calculations on the two component data, the method described by Walker(1988) for reducing the two component data is shown here.

The first step was to resolve the measured velocities, U'_1 and U'_2 into orthogonal components. The measured velocities were resolved into orthogonal velocity components, U_1 and U_2 in the following manner:

$$U_1 = U'_1 \quad (2.3)$$

$$U_2 = \frac{1}{\cos\theta_i} U'_2 + \tan\theta_i U'_1. \quad (2.4)$$

The quantity θ_i is the actual angle between the velocity components and is determined from beam geometry measurements. From the orthogonal pair of velocities, U_1 and U_2 , all other velocity statistics were determined.

For any θ measured relative to the flow direction, the streamwise and normal velocity components are determined from

$$U = U_2 \cos\theta + U_1 \sin\theta \quad (2.5)$$

$$V = U_2 \sin \theta - U_1 \cos \theta. \quad (2.6)$$

Here θ is determined by taking the time average of Equation 2.5 and setting $\bar{V} = 0$, so that

$$\theta = \tan^{-1} \left[\frac{\bar{U}_1}{\bar{U}_2} \right] \quad (2.7)$$

One value of θ was used for all y-locations. This value was determined from outer flow measurements, where signal quality was best.

The calculation of the second moments for the rotated coordinate system is more complicated than the mean velocity calculations. The equations for the second moments are:

$$\overline{u^2} = \overline{u_1^2} \sin^2 \theta + \overline{u_2^2} \cos^2 \theta + 2\overline{u_1 u_2} \cos \theta \sin \theta \quad (2.8)$$

$$\overline{v^2} = \overline{u_1^2} \cos^2 \theta + \overline{u_2^2} \sin^2 \theta - 2\overline{u_1 u_2} \cos \theta \sin \theta \quad (2.9)$$

$$\overline{uv} = \left[\overline{u_2^2} - \overline{u_1^2} \right] \sin \theta \cos \theta + \overline{u_1 u_2} \left[\sin^2 \theta - \cos^2 \theta \right] \quad (2.10)$$

As shown by Equation 2.1, the average shear stress in a fully developed flow is proportional to pressure drop. However, in a rectangular channel, the wall shear stress is not the same at each location on the perimeter surrounding the flow area. Hence the shear stress in the vicinity of the test location will differ from the average shear stress. In order to make a more accurate estimate of local wall shear stress, it is possible to use velocity data to make the calculation. In this case, the shear stress varies linearly from a maximum at the wall to zero at the channel half-height and is given by:

$$\tau = \mu \frac{d\bar{U}}{dy} - \rho \bar{u}\bar{v} = \tau_w(1-y/a) \quad (2.11)$$

where τ is the total shear stress at a point in the flow, τ_w is the wall shear stress, and a is the channel half-height. Using the definition of the shear velocity, $u_\tau = \sqrt{\frac{\tau_w}{\rho}}$ and rearranging Equation 2.11, yields:

$$u_\tau = \left[\frac{\mu \frac{d\bar{U}}{dy} - \bar{u}\bar{v}}{1-y/a} \right]^{1/2} \quad (2.12)$$

By measuring the turbulent shear stress, $\bar{u}\bar{v}$ and calculating the derivative of the mean velocity from the data, it is possible to estimate the wall shear stress (and the shear velocity) at the center of the channel where the flow is not affected by the secondary flows in the corners. Since the well mixed concentration of polymer in the channel is low (3–5 ppm) in the measurement location, the difference in the shear viscosities of water and polymer flows are minimal (see Virk 1975). Therefore, the water properties are used in all calculations.

2.7 Factorial Design

In order to estimate the dependence of drag reduction upon wall strain rate and average polymer concentration in the channel, a factorial design was implemented (Hunter, 1961). The factorial design method has the advantage of providing the required result with the minimal amount of experimentation. The first step in implementing the factorial design was to define a range of interest for both independent variables. For this study, the wall strain rates ranged from 1000 to 4000 s⁻¹ and the well

mixed polymer concentrations ranged from 3–5 ppm. A set of normalized coordinates were then defined with the center of the range coinciding with the origin of these coordinates. The normalized coordinates were defined as:

$$X_1 = \frac{\left. \frac{d\bar{U}}{dy} \right|_w - 1500 \text{ s}^{-1}}{2500 \text{ s}^{-1}} \quad (2.13)$$

and

$$X_2 = \frac{\bar{C} - 4 \text{ ppm}}{1 \text{ ppm}}. \quad (2.14)$$

Figure 2.2 displays the normalized coordinates in relation to the dimensional coordinate system; the experimental conditions for this study are shown in Table 2.2. The wall strain rates shown in Table 2.2 were deduced from the infinite aspect ratio formula,

$$\left. \frac{d\bar{U}}{dy} \right|_w = \frac{\Delta Ph}{2\mu\Delta x}. \quad (2.15)$$

A regression model of the form

$$DR = A_0 + A_1 X_1 + A_2 X_2 + A_{12} X_1 X_2 \quad (2.16)$$

was then fit to the data.

In order to extend the region of applicability of the model and obtain a better appreciation of the response function, a quadratic form can be used. The quadratic model has the form

$$DR = A_0 + A_1 X_1 + A_2 X_2 + A_{11} X_1^2 + A_{22} X_2^2 + A_{12} X_1 X_2. \quad (2.17)$$

To estimate all of the coefficients in this model, the linear model is augmented by four

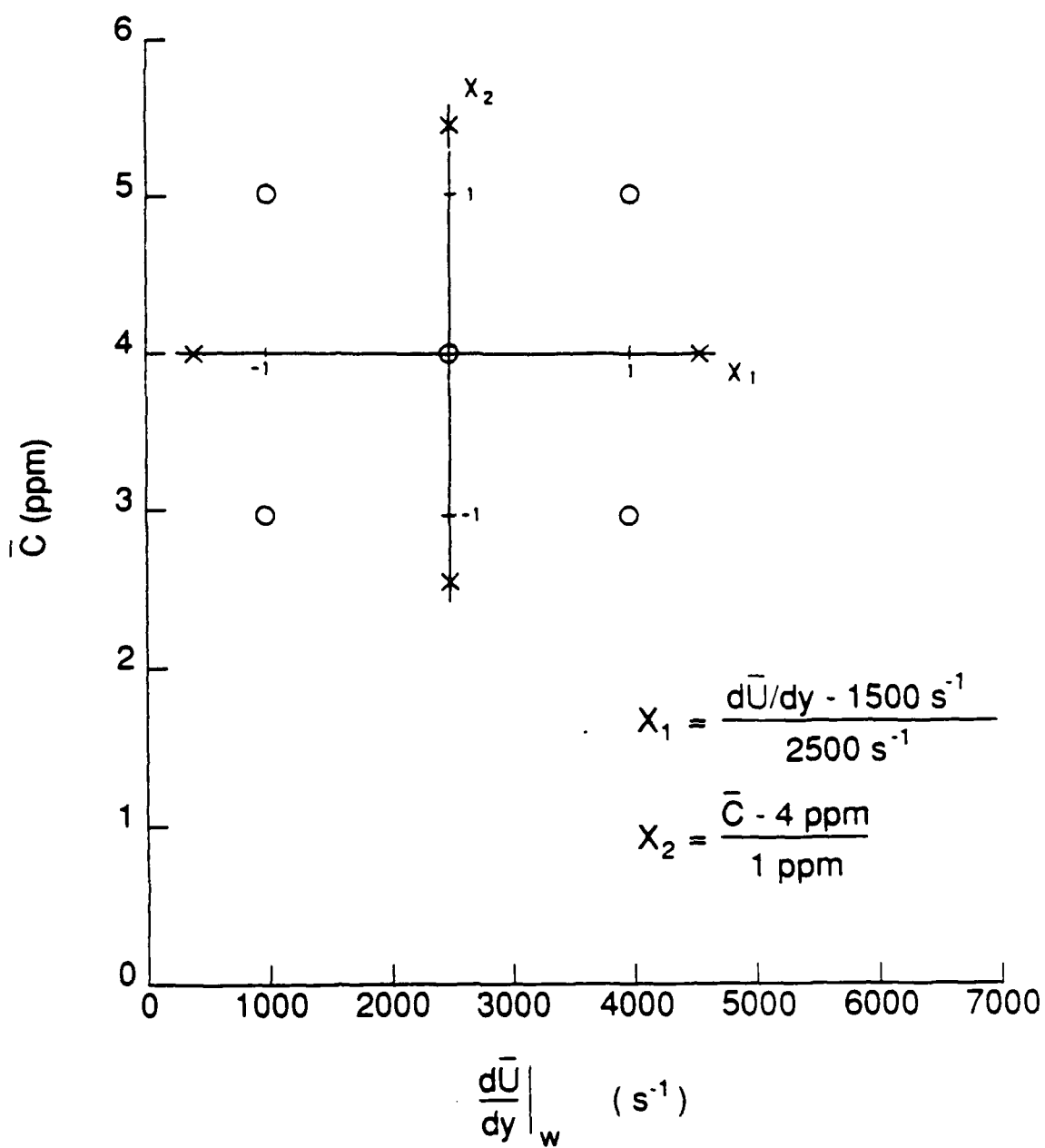


Figure 2.2. Factorial design space; o, linear design points; x, additional points for quadratic design.

additional design points. Figure 2.2 also shows these additional normalized design points in relation to dimensional coordinates. Table 2.2 also contains these four new design points, which are the last four entries, in addition to the linear model design points.

Table 2.2. Experimental conditions for the factorial design

X_1	X_2	$\frac{d\bar{U}}{dy} \Big _w \text{ (s}^{-1}\text{)}$	$\bar{C} \text{ (ppm)}$
-1	-1	1000	3
-1	1	1000	5
0	0	2500	4
1	-1	4000	3
1	1	4000	5
0	$-\sqrt{2}$	2500	2.6
$-\sqrt{2}$	0	380	4
0	$\sqrt{2}$	2500	5.4
$\sqrt{2}$	0	4620	4

2.8 Burst Detection Analysis

In order to determine the period of the burst cycle for a flow, longtime velocity records which included the time between data points were taken. The velocity records were at least 1000 burst cycles long for each particular flow condition to ensure a good average for the period of the burst cycle. To deduce the burst cycle period, a probability plot such as one shown in Figure 2.3 was constructed. From such a plot, a grouping parameter must be found so that ejections from the same burst can be grouped together. To find this grouping parameter, the plot is first divided into three straight

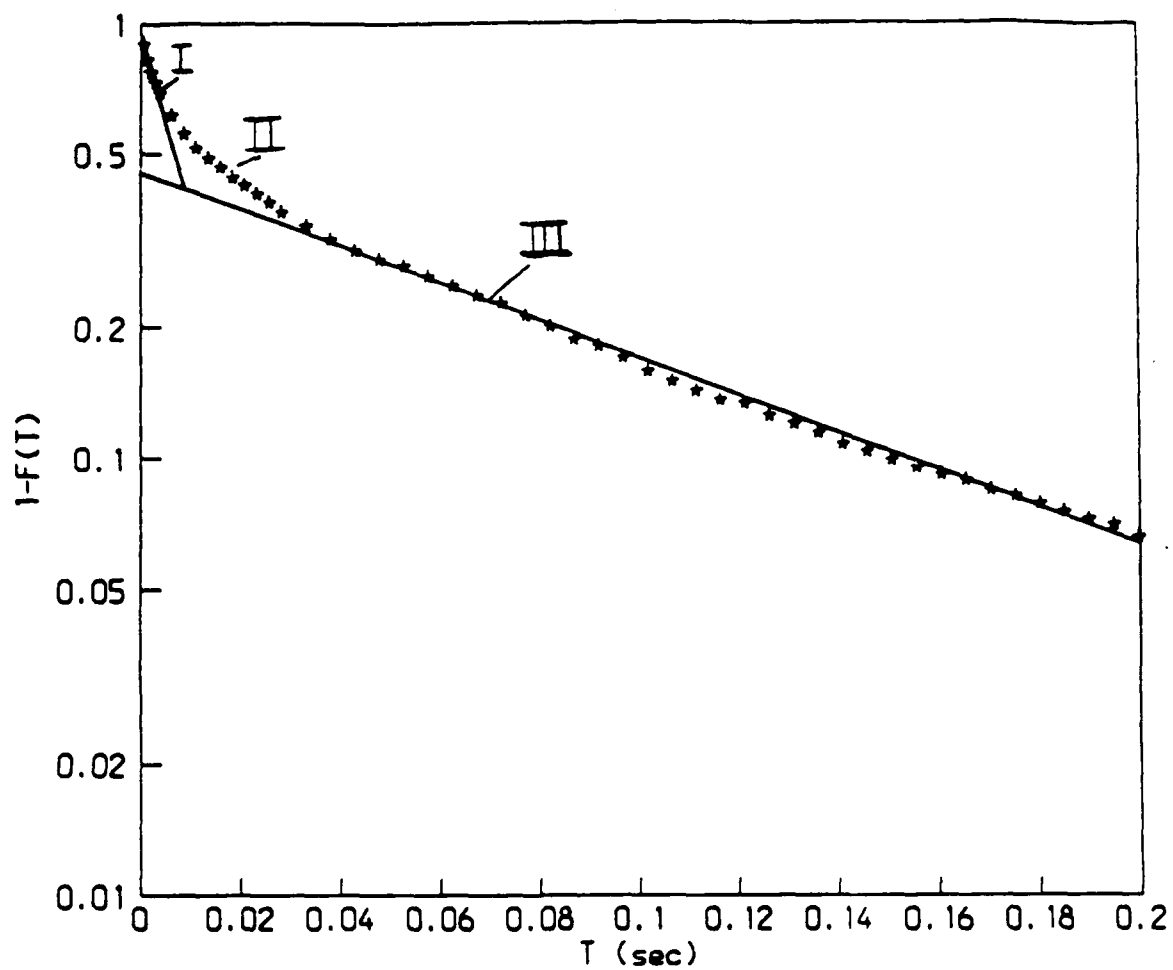


Figure 2.3. Probability distribution for the grouping parameter

line regions. The first region defines ejections that are from the same burst. The third region defines ejections that are from different bursts and the second region is an overlap of the first and third regions. Tiederman(1988) used the time corresponding to the intersection of lines drawn through regions I and III as the value of the grouping parameter. A modification to this method was used in this study to obtain the grouping parameter. The endpoints of region II were defined (points that are clearly not in regions I or III) and the average of the the times corresponding to these two points was used as the grouping parameter. Since the grouping parameter cannot be determined exactly, twenty-five percent of the range of region II on either side of the grouping parameter is assigned as the range of uncertainty for the grouping parameter.

CHAPTER 3 - RESULTS

3.1 Effect of Wall Strain Rate and Polymer Concentration on Drag Reduction

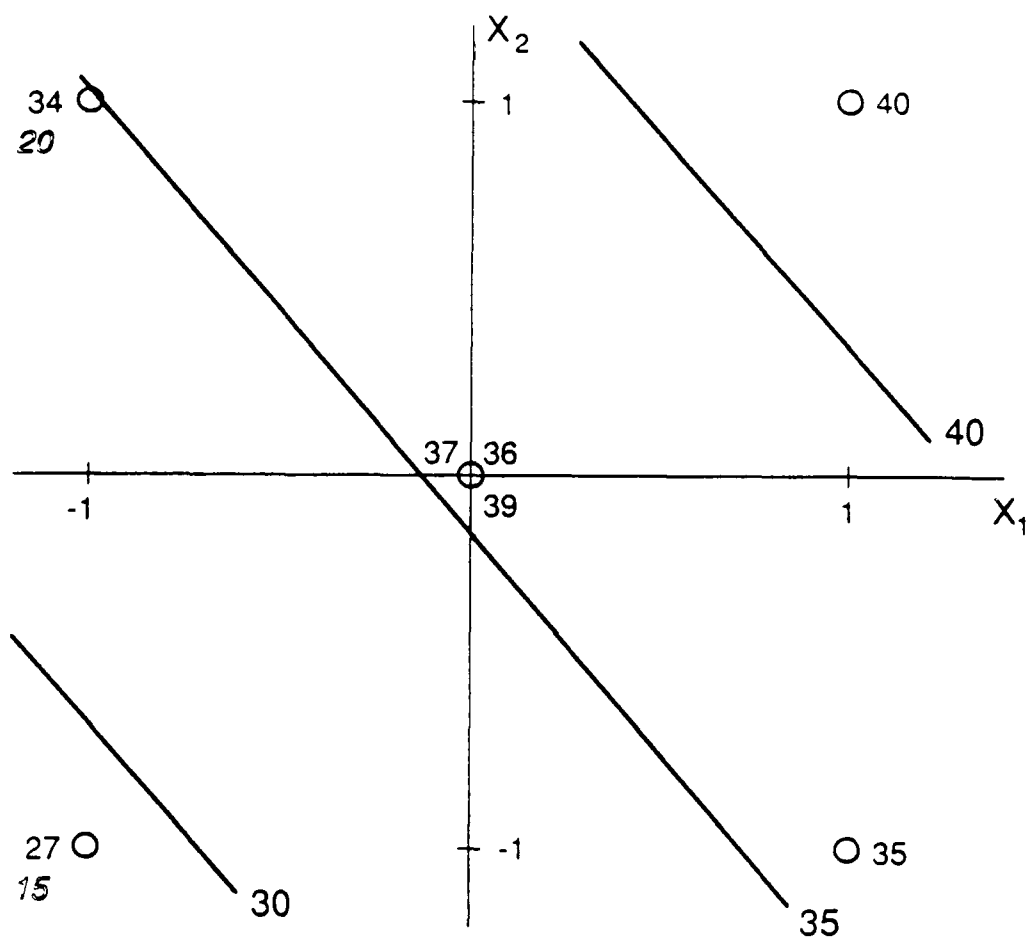
Pressure drop measurements at each of the flow conditions specified in the factorial design yielded the drag reduction results in Figure 3.1. Due to limited pumping capacity, data could only be obtained in the 6.0 cm channel at a wall strain rate of 1000 s^{-1} . Since the regression analysis requires data at all values of the design, only the 2.5 cm channel data could be used to evaluate the effect of wall strain rate and concentration. The flow condition corresponding to the origin of the design space was repeated several times in order to estimate the error involved in the measurement. A linear dependence of drag reduction upon the variables was assumed, and a least-squares regression analysis yielded the model:

$$\text{DR} = 35.4 + 3.5X_1 + 3.0X_2 - 0.5X_1X_2 \quad (3.1)$$

A statistical tool called the F-test was used to determine the significance of the model and its individual terms. The F-test revealed that the influence of the cross correlation term is not larger than the error of measurement. Hence the X_1X_2 term is not significant and the linear model becomes:

$$\text{DR} = 35.4 + 3.5X_1 + 3.0X_2 \quad (3.2)$$

This model yields a correlation coefficient of 0.9986.



$$DR = 35.4 + 3.5 X_1 + 3.0 X_2$$

$$r = 0.9986$$

Figure 3.1. Dependence of drag reduction upon wall strain rate and polymer concentration; linear model: italicized numbers, 6.0 cm channel results; other, 2.5 cm channel results.

In an attempt to obtain a better fitting model and to extend the region of applicability, a quadratic dependence of drag reduction on the variables was assumed. This new model requires four more points on the design plot in addition to the five from the linear model. These four points in addition to the five points from the linear model are shown in Figure 3.2. The regression analysis yields:

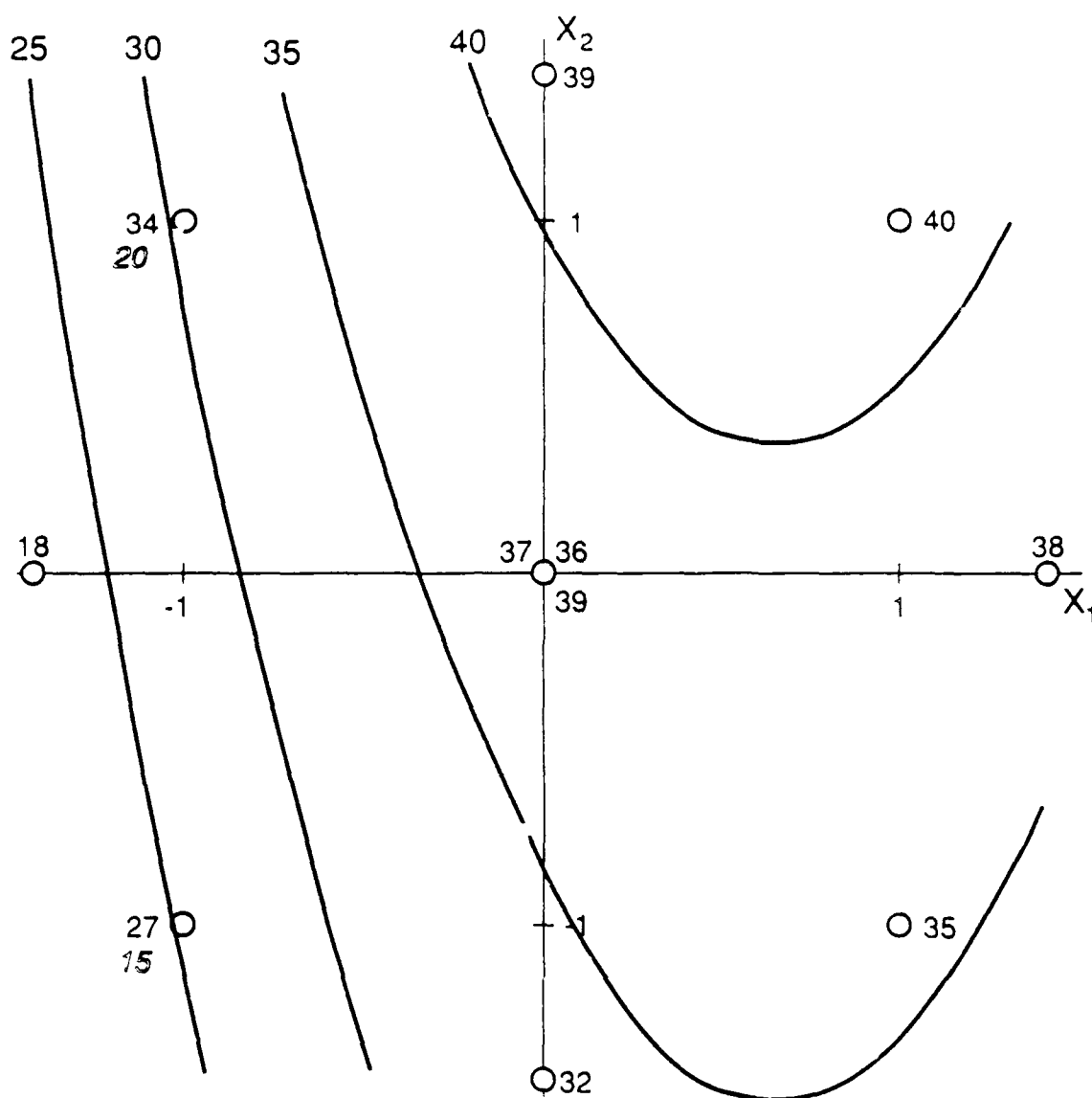
$$DR = 37.3 + 5.3X_1 + 2.7X_2 - 4.1X_1^2 - 0.35X_2^2 - 0.5X_1X_2 \quad (3.3)$$

The F-test for this model determined that the effects of the cross correlation term, X_1X_2 and the X_2^2 term are not significant. The final form of the quadratic model which had a correlation coefficient of 0.9984 was:

$$DR = 37.3 + 5.29X_1 + 2.74X_2 - 4.1X_1^2 \quad (3.4)$$

As seen by these results, the quadratic model does not provide a better fit than the linear model over the range where the linear model is valid. For this reason, it was decided that the velocity data would be made at the flow conditions corresponding to the linear design.

Results from the 6.0 cm channel (shown on both Figures 3.1 and 3.2) show that for the same wall strain rate and polymer concentration, the drag reduction is different in the two channels. From these results, it is seen that drag reduction clearly depends upon all three variables, although the dependence upon channel height has not been defined.



$$DR = 37.3 + 5.3 X_1 + 2.7 X_2 - 4.1 X_1^2$$

$$r = 0.9984$$

Figure 3.2. Dependence of drag reduction upon wall strain rate and polymer concentration; quadratic model: italicized numbers, 6.0 cm channel results; other, 2.5 cm channel results.

3.2 Evaluation of Shear Velocity

It is of primary importance to have an accurate value of wall shear stress. For this study, Equations 2.1 and 2.11 estimate wall shear stress (hence shear velocity) from pressure drop and from the sum of the viscous and Reynolds stresses respectively. Figure 3.3 shows the relationship between the local wall shear stress, τ_w^* , and the average wall shear stress, $\left[\bar{\tau}_w\right]_{2D}$. In all flows, $\left[\bar{\tau}_w\right]_{2D}$ was from 10-30 % higher than τ_w^* . It is hypothesized that endwall effects are responsible for the significant difference in the shear stress estimates. Because of the difference in the local and average shear stresses, it was necessary to choose one shear stress to normalize the velocity statistics. It was decided that τ_w^* would be used for normalizations. It is not only a better estimate of the shear stress at the channel mid-span location, but it also is independent of the channel aspect ratio.

Figure 3.4 shows a typical variation of the local shear velocity with the distance from the wall for the water flow in the 2.5 cm channel at a wall strain rate of 1000 s^{-1} . The shear velocity, estimated as the average of all of the points, had a value of $0.0294 \text{ m/s} \pm 0.0017 \text{ m/s}$ at 95% confidence.

Figure 3.3 reveals that most of the drag-reduced flows yielded results similar to those for the water flows. For these dilute, well-mixed polymer flows, the Newtonian assumption was valid. However, for the drag-reduced flow at 4000 s^{-1} and 5 ppm in the 2.5 cm channel, a plot such as Figure 3.4 yielded such widely scattered values for the shear velocity that a good average was impossible to estimate. Willmarth et al. (1987) obtained similar results for their drag-reducing channel flow. Apparently some non-

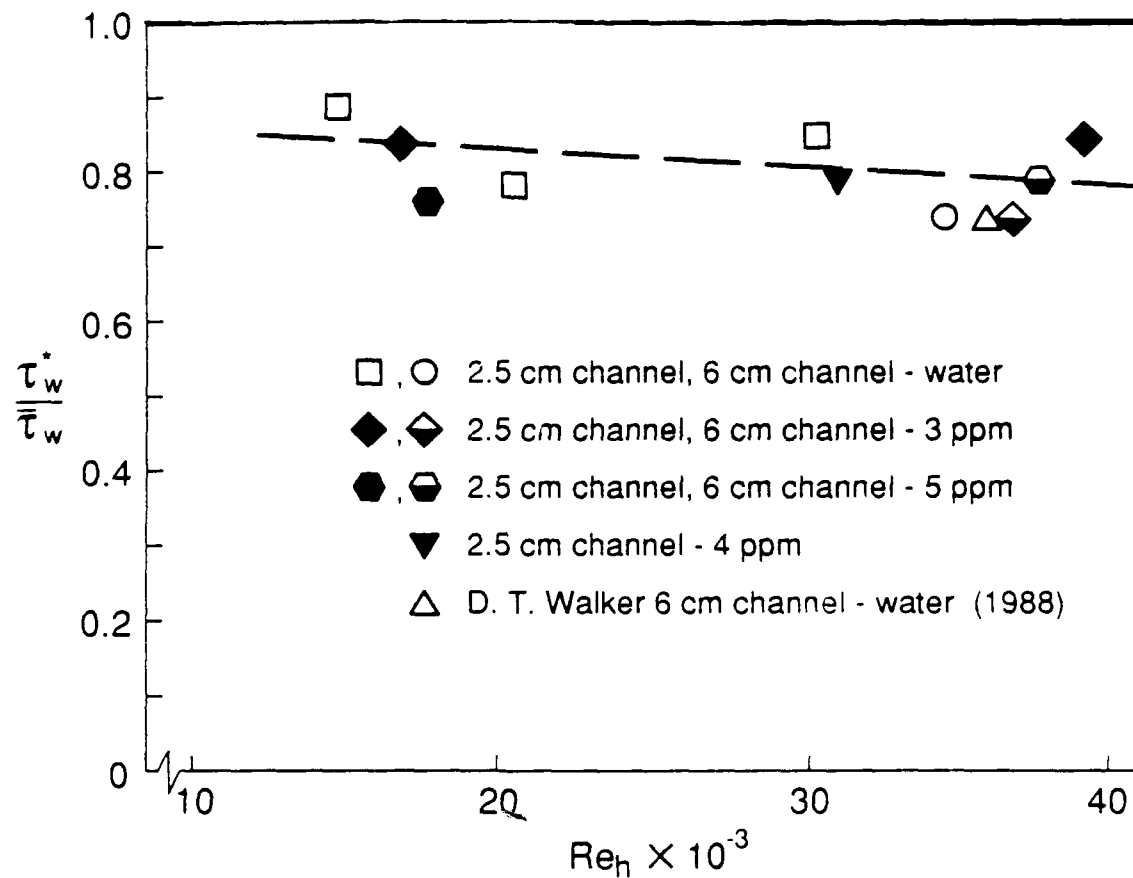


Figure 3.3. Effect of Reynolds number on the local to average shear stress ratio.

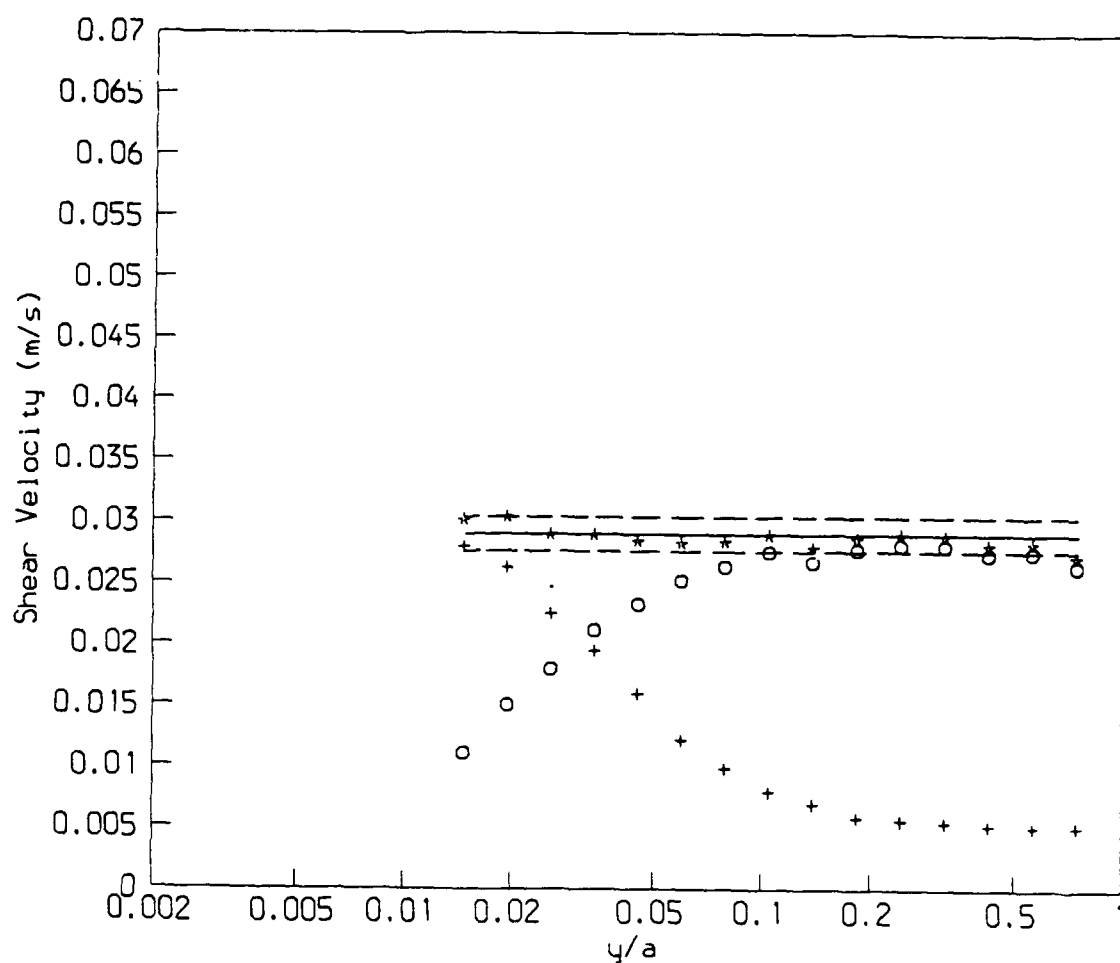


Figure 3.4. Estimated shear velocity for water flow, $\frac{d\bar{U}}{dy} \Big|_w = 1000 \text{ s}^{-1}$, 2.5 cm channel:
 *, u_τ ; +, viscous contribution; O turbulent contribution; =====, 95% confidence interval; —, u_τ mean.

Newtonian factor is involved and Equation 2.11 cannot be used to estimate τ_w^* . It is possible to fit a line through the data on Figure 3.3 and extrapolate a value for the ratio of the stresses for the 4000 s^{-1} , 5 ppm flow ($Re_h = 41,610$) and from the measured pressure drop estimate τ_w^* . This was done so that the velocity statistics for all flows can be normalized in the same way.

3.3 Water Flow

Water flow measurements were made for each of the wall strain rates in the experimental design (three in the 2.5 cm channel and one in the 6.0 cm channel). These measurements were made to verify the standard nature of the water flows and to have a base for comparison with drag-reduced flows.

The standard water flow case has been well studied by other experimenters. Kreplin and Eckelmann (1979) measured the three fluctuation velocity components in an oil channel, where due to the high viscosity of the oil, they obtained excellent spatial resolution. Hussain and Reynolds (1975) made streamwise velocity measurements in an air channel flow with an exceptionally large development length ($l/h = 196$) and large aspect ratio (18:1). Previous measurements in the 2.5 cm channel and the 6.0 cm channel have been made by Luchik (1985) and Walker (1988) respectively.

3.3.1 Mean Velocity Profiles

Figure 3.5 shows the mean velocity profiles for all water flows normalized with the corresponding shear velocity. The two solid lines on each plot represent the behavior of the flow in the linear sublayer:

$$U^+ = y^+ \quad (3.5)$$

and the logarithmic (overlap) zone:

$$U^+ = \frac{1}{\kappa} \ln y^+ + B. \quad (3.6)$$

In the second equation, the value of κ , the von Karman constant, was 0.40 for all water flows. However the intercept, B , varied from flow to flow as shown on Figure 3.5.

3.3.2 Second Moments

Figure 3.6 shows the behavior of the root-mean-square (RMS) of the fluctuating streamwise and normal velocities as a function of distance from the wall. These results show that in all of the water flows, u'^+ peaks at 2.76 for a $y^+ \approx 15$. The RMS of the normal velocity peaks at a $y^+ \approx 75$ with a value of 1.12. These results show some scatter for $y^+ > 100$ but closer examination reveals that the variation correlates with Reynolds number. These results agree with those of Wei (1987) who shows that the fluctuating quantities in the outer region do not scale with inner variables and that there is a Reynolds number dependence. However, in contrast with Wei (1987) inner scaling does correlate the data for all Reynolds number in the wall region. The results of this study show similar trends as those of (Walker, 1988) but are about 7% lower across the channel half-height. These results agree well in trend with the numerical simulation of Kim et al. (1987) and the experiments of Hussain and Reynolds (1975) but the values here are slightly higher.

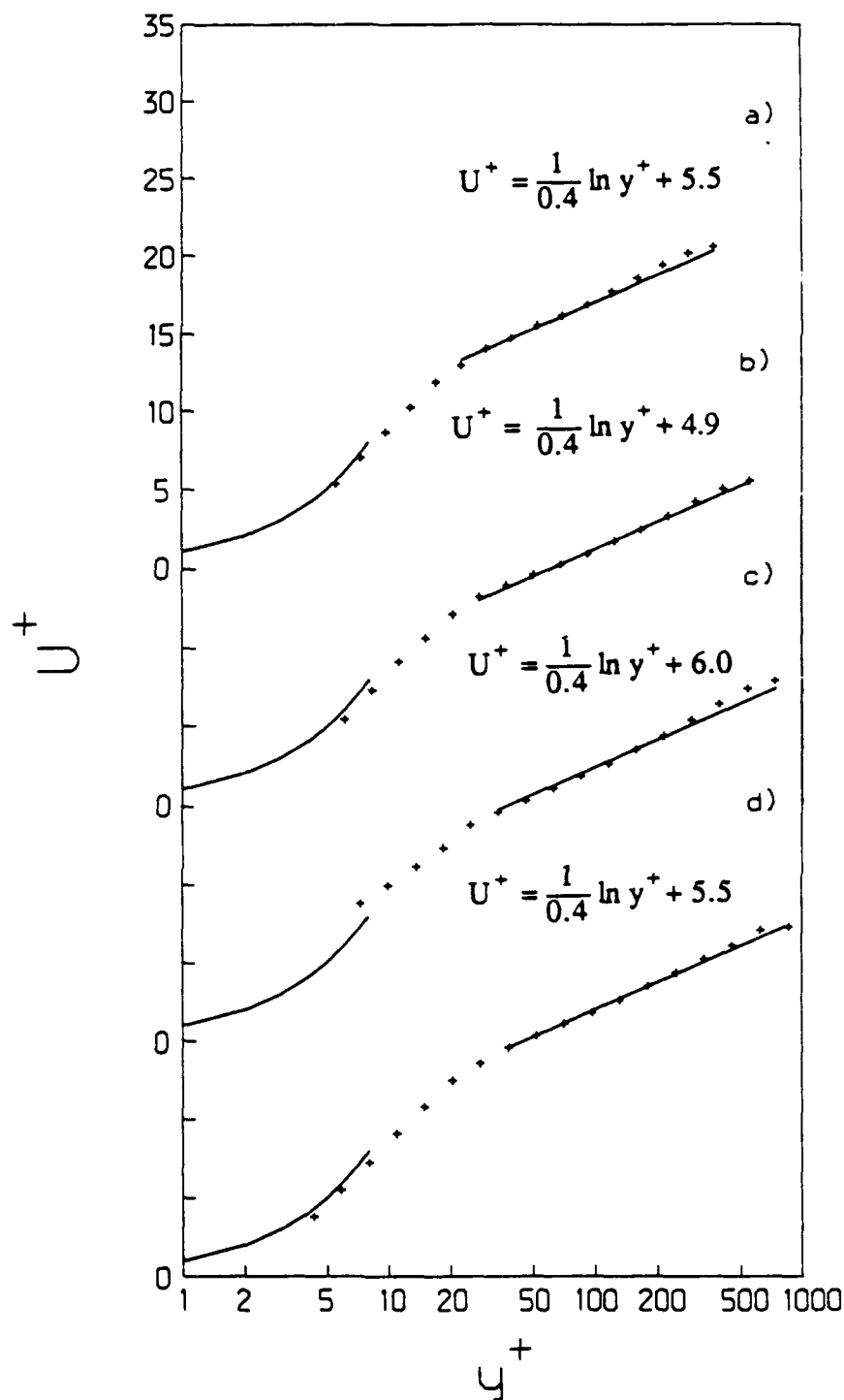


Figure 3.5. Mean velocity profiles for water flows: a) 2.5 cm channel, $Re_h = 14,430$; b) 2.5 cm channel, $Re_h = 20,260$; c) 2.5 cm channel, $Re_h = 30,420$; d) 6.0 cm channel, $Re_h = 34,640$.

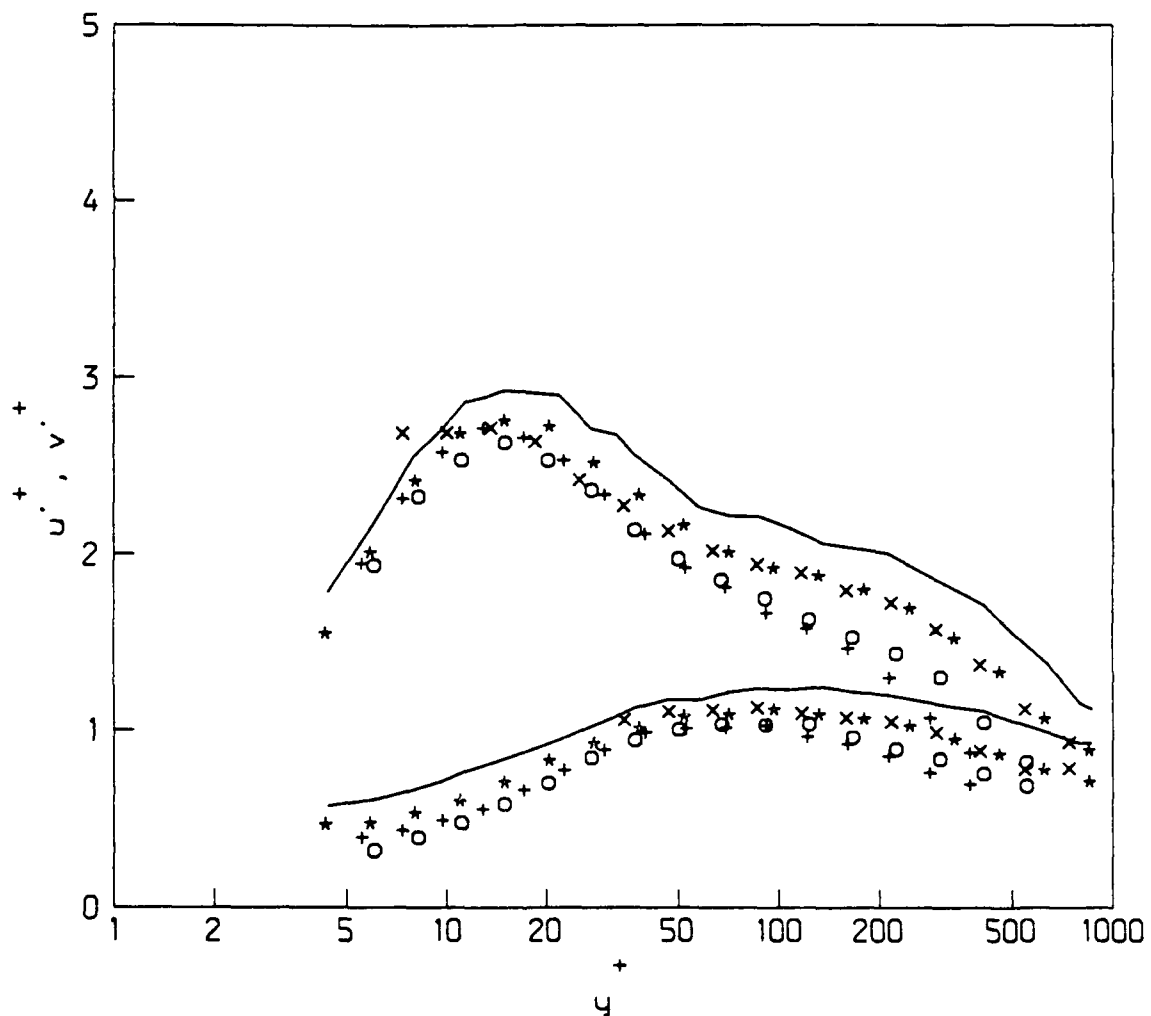


Figure 3.6. Root-mean-square velocity fluctuation profiles for water flows: +, 2.5 cm channel, $Re_h = 14,430$; o, 2.5 cm channel, $Re_h = 20,260$; x, 2.5 cm channel, $Re_h = 30,420$; *, 6.0 cm channel, $Re_h = 34,640$; —, Walker (1988).

The near-wall behavior of the rms velocities are shown in Figure 3.7. The data follow the expected trend in u'^+ as the wall is approached. The v'^+ data follow the expected trends for $y^+ \geq 10$. Finnicum and Hanratty (1985) show that in the near-wall region ($y^+ < 10$), v'^+ should vary as y^{+2} . Since the results diverge from the expected trend, v'^+ quantities are questionable for $y^+ \leq 10$. The near-wall results do agree with those of Kreplin and Eckelmann (1979) and further away from the wall, the Reynolds number effect becomes evident.

Turbulence intensity profiles are shown in Figure 3.8. At the centerline of the channel, the turbulence intensities were about 4%, which agree with the trends shown by Hinze (1975). The streamwise turbulence intensity attains a value of 0.4 as the wall is approached. This is higher than that of Kim et al. (1987) but agrees with Walker (1988). As before, the normal turbulence intensity behaves as expected except in the near-wall region.

In a fully developed channel flow, the total shear stress varies linearly from a maximum at the wall to zero at the centerline according to Equation 2.9.

$$\tau = \mu \frac{d\bar{U}}{dy} - \rho \bar{u}v = \tau_w^* (1 - y/a). \quad (2.9)$$

Figure 3.9 shows the variation of the turbulent stress, $\bar{u}v$, normalized with the shear velocity as a function of distance from the wall. The trend of the data is in agreement with the literature.

Figure 3.10 shows the $\bar{u}v$ data from the water flow in semi-log coordinates, which allows closer inspection of the near-wall region. These results show that in the 2.5 cm

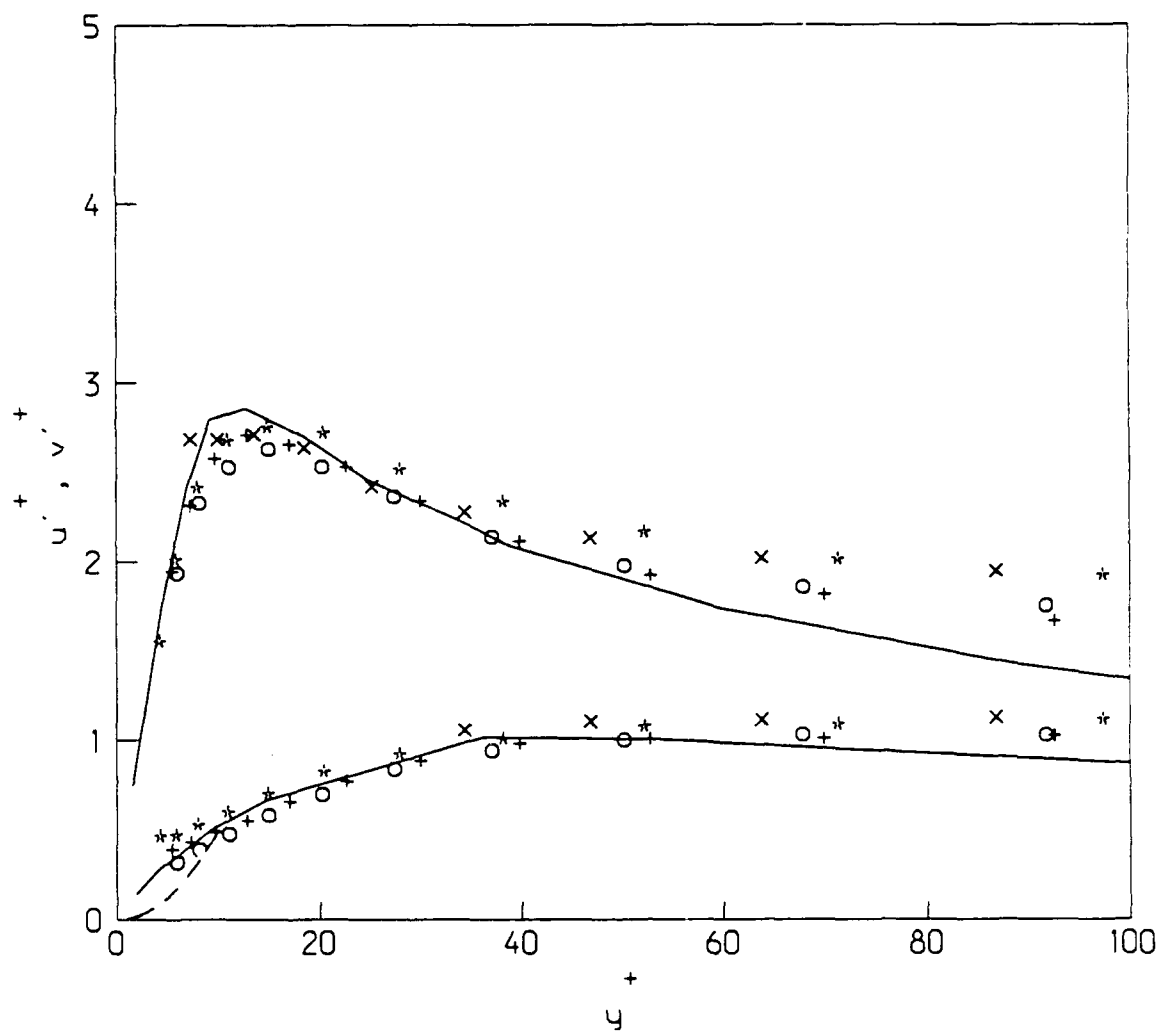


Figure 3.7. Near-wall behavior of the root-mean-square velocities: +, 2.5 cm channel, $Re_h = 14,430$; o, 2.5 cm channel, $Re_h = 20,260$; x, 2.5 cm channel, $Re_h = 30,420$; *, 6.0 cm channel, $Re_h = 34,640$; —, Kreplin and Eckelmann (1979); ---, $v'^+ = 0.005 y^{+2}$ (Finnicum and Hanratty, 1985).

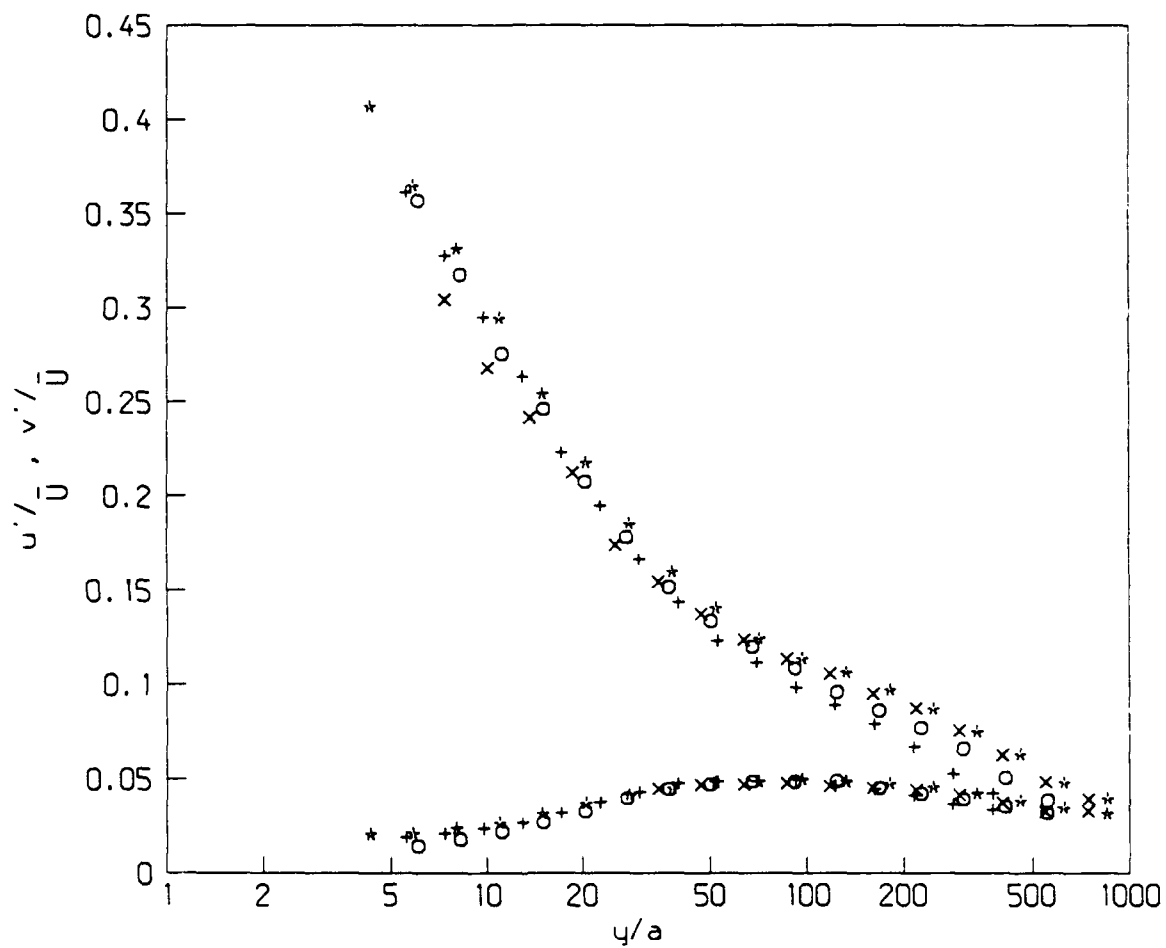


Figure 3.8. Turbulence intensity profiles: +, 2.5 cm channel, $Re_h = 14,430$; o, 2.5 cm channel, $Re_h = 20,260$; x, 2.5 cm channel, $Re_h = 30,420$; *, 6.0 cm channel, $Re_h = 34,640$.

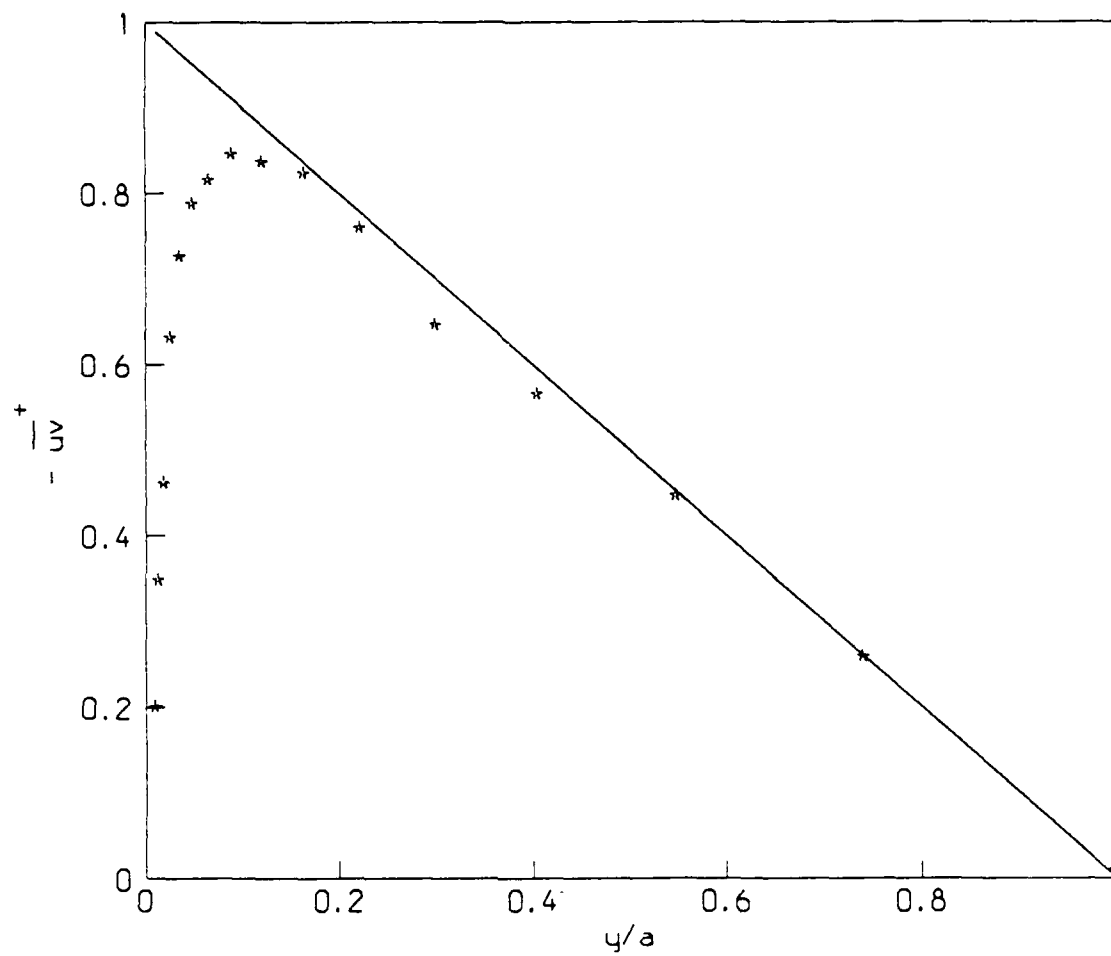


Figure 3.9. Reynolds shear stress variation, 2.5 cm channel, $Re_h = 14,430$: *, Reynolds stress; —, $\tau_w^*(1-y/a)$.

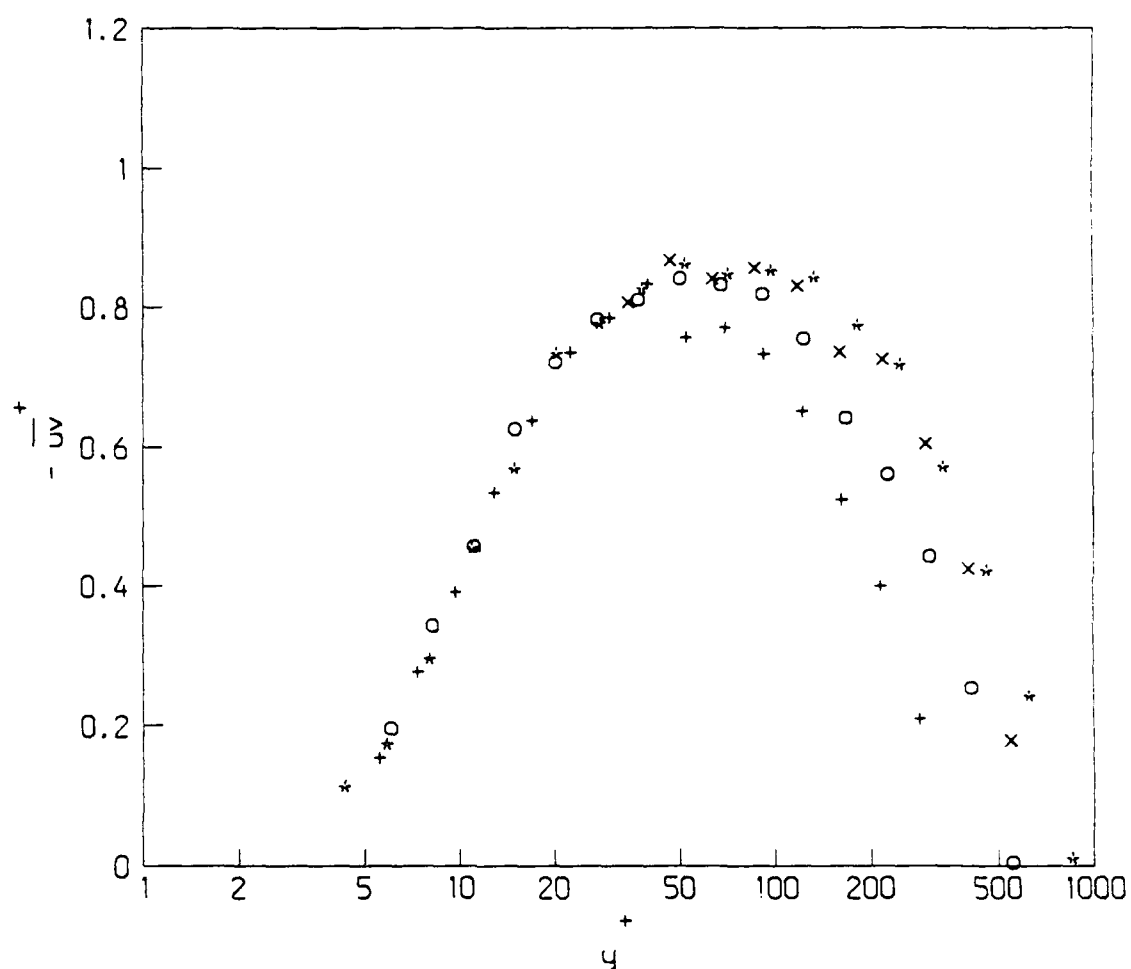


Figure 3.10. Near-wall behavior of the Reynolds stresses: +, 2.5 cm channel, $Re_h = 14,430$; o, 2.5 cm channel, $Re_h = 20,260$; x, 2.5 cm channel, $Re_h = 30,420$; *, 6.0 cm channel, $Re_h = 34,640$.

channel, as the wall strain rate (Reynolds number) increases, a region in y^+ develops where the turbulent stress is essentially constant for each flow. The higher Reynolds number flows show such a region, while the lower Reynolds number flows do not. This is the constant stress region that Sreenivasan (1988) uses to define the logarithmic zone of the mean velocity profile. It is important to note that the constant stress region is not a stringent condition for a logarithmic zone, especially at low Reynolds number. Sreenivasan points out that a region where the Reynolds stress is at least 70% of the peak can be used to determine the log zone without losing accuracy.

Equation 2.9 can be rearranged to solve for the Reynolds stress, given τ_w^* and a derivative of the mean velocity profile. The new equation has the form:

$$-\rho \overline{uv} = \tau_w^* (1 - y/a) - \mu \frac{d\overline{U}}{dy} \quad (3.7)$$

Figure 3.11 presents the same data as Figure 3.10 with the addition of \overline{uv} (shown as solid lines) as calculated by Equation 3.7. The fit between the experimental and calculated stresses is good with the exception of some scatter around the peak stresses.

The correlation coefficient, R_{uv} for all water flows is shown in Figure 3.12. The correlation coefficient is a measure of the how much the u and v velocity fluctuations contribute to the net momentum transport. The results show that the correlation coefficient decreases with increasing Reynolds number, a trend in agreement with Wei (1987). The peak decreases from 0.43 to 0.37 as the Reynolds number increases from 14,430 to 30,640. The present results agree with the numerical work of Kim et al. (1987) who obtained a peak value of about 0.45 at a Reynolds number ≈ 5600 .

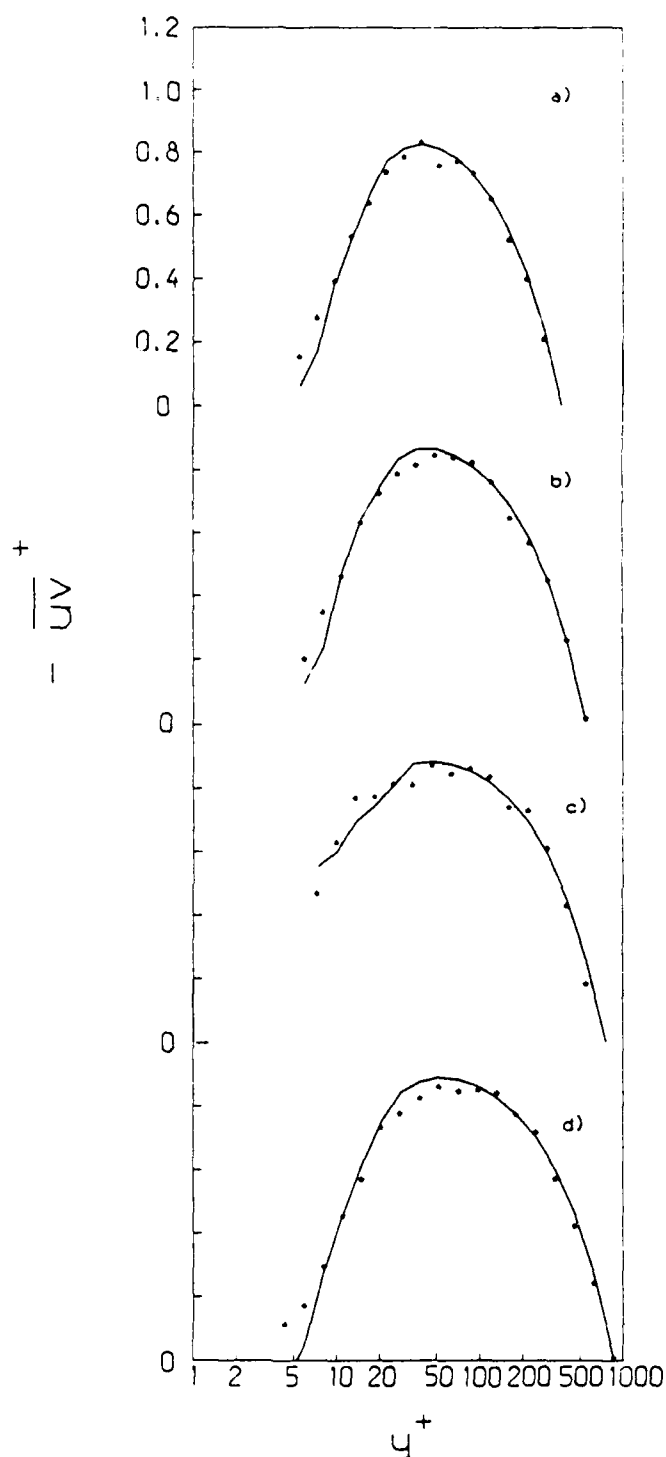


Figure 3.11. Near-wall behavior of the Reynolds stresses with calculated value from Equation 3.8: a) 2.5 cm channel, $Re_h = 14,430$; b) 2.5 cm channel, $Re_h = 20,260$; c) 2.5 cm channel, $Re_h = 30,420$; d) 6.0 cm channel, $Re_h = 34,640$; o, experimental data; — from Equation 3.7.

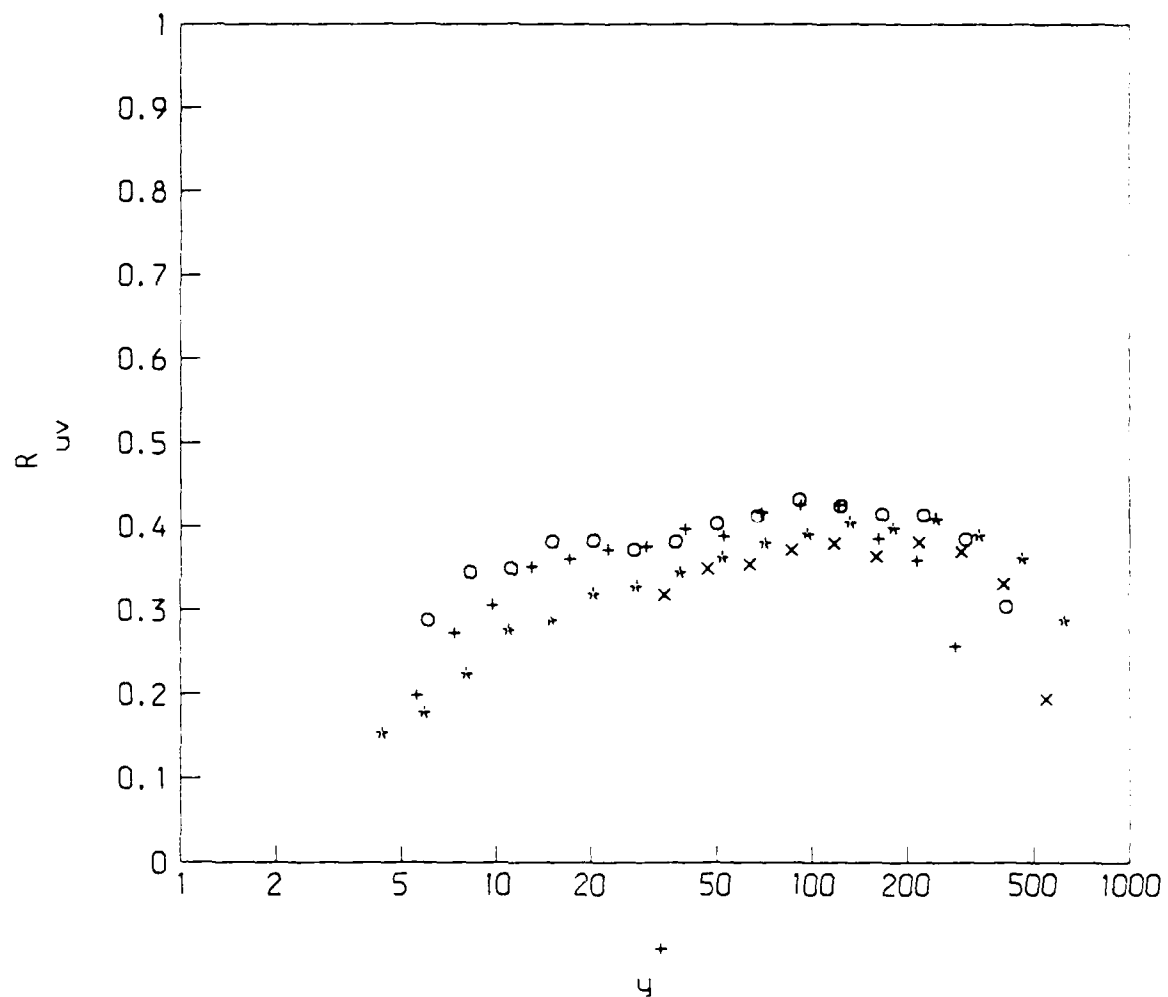


Figure 3.12. Correlation coefficient profiles: +, 2.5 cm channel, $Re_h = 14,430$; o, 2.5 cm channel, $Re_h = 20,260$; x, 2.5 cm channel, $Re_h = 30,420$; *, 6.0 cm channel, $Re_h = 34,640$.

3.3.3 Reynolds Stress Production

In this section, the transport equations for the elements of the Reynolds stress tensor, $\overline{u_i u_j}$, are introduced. The derivation of these equations is a straightforward process and can be seen in Bradshaw (1978). These equations are not conservation equations in the thermodynamic sense, but the terms in the equations represent production, destruction, and transport of $\overline{u_i u_j}$ in a differential control volume. The general form of these equations as presented by Walker (1988) is shown in Equation 3.8.

$$\begin{aligned}
 \frac{\partial \overline{u_i u_j}}{\partial t} + \overline{U}_1 \frac{\partial \overline{u_i u_j}}{\partial x_1} = & \text{I} \left[\overline{u_i u_1} \frac{\partial \overline{U}_j}{\partial x_1} + \overline{u_j u_1} \frac{\partial \overline{U}_i}{\partial x_1} \right] \\
 & \text{II} + \frac{p'}{\rho} \left[\frac{\partial u_i}{\partial x_j} + \frac{\partial u_j}{\partial x_i} \right] \\
 & \text{III} - \frac{\partial}{\partial x_1} (\overline{u_i u_j u_1}) - \frac{1}{\rho} \left[\frac{\partial}{\partial x_i} (\overline{p' u_j}) + \frac{\partial}{\partial x_j} (\overline{p' u_i}) \right] \\
 & \text{V} + \nu \frac{\partial^2 \overline{u_i u_j}}{\partial x_1^2} - 2\nu \left[\frac{\partial u_i}{\partial x_1} \frac{\partial u_j}{\partial x_1} \right] \text{VI}
 \end{aligned} \tag{3.8}$$

The left hand side of Equation 3.8 represents the net rate of transport $\overline{u_i u_j}$ out of a unit control volume. On the right hand side, term I represents the rate of generation of $\overline{u_i u_j}$ by the interaction of the Reynolds stresses with the mean velocity gradients in the flow. Term II is the "pressure-strain" or redistribution term. It tends to make the turbulence more isotropic by equalizing the normal stresses and reducing the shear stresses. Terms

III and IV account for the transport of Reynolds stresses by turbulent velocity and pressure fluctuations respectively. Term V represents transport of Reynolds stresses due to viscous action and term VI represents the destruction of $\overline{u_i u_j}$ through viscous fluctuations.

Equation 3.8 can now be specialized for the three non-zero Reynolds stresses of this study. For the streamwise normal-stress $\overline{u^2}$ the result is Equation 3.9.

$$\begin{aligned}
 0 = & \overset{\text{I}}{-2 \overline{u v} \frac{\partial \overline{U}}{\partial y}} + \overset{\text{II}}{2 \frac{p'}{\rho} \left[\frac{\partial u}{\partial x} \right]} - \overset{\text{III}}{\frac{\partial}{\partial y} \overline{(u^2 v)}} \\
 & \overset{\text{V}}{+ v \frac{\partial^2 \overline{u^2}}{\partial y^2}} - \overset{\text{VI}}{2v \left[\overline{\left(\frac{\partial u}{\partial x} \right)^2} + \overline{\left(\frac{\partial u}{\partial y} \right)^2} + \overline{\left(\frac{\partial u}{\partial z} \right)^2} \right]}
 \end{aligned} \tag{3.9}$$

The production of $\overline{u^2}$ is the first term on the right hand side. Term I is balanced primarily by the destruction due to viscous fluctuations (term VI) and the redistribution to the other stresses through the pressure-strain term (term II). Notice that there is no transport of $\overline{u^2}$ due to pressure fluctuations. The equation for the wall-normal normal stress $\overline{v^2}$ is shown as Equation 3.10.

$$\begin{aligned}
 0 = & \overset{\text{II}}{2 \frac{p'}{\rho} \left[\frac{\partial v}{\partial y} \right]} - \overset{\text{III}}{\frac{\partial \overline{(v^3)}}{\partial y}} - \overset{\text{IV}}{\frac{2}{\rho} \frac{\partial}{\partial y} \overline{(p' v)}} \\
 & \overset{\text{V}}{+ v \frac{\partial^2 \overline{v^2}}{\partial y^2}} - \overset{\text{VI}}{2v \left[\overline{\left(\frac{\partial v}{\partial x} \right)^2} + \overline{\left(\frac{\partial v}{\partial y} \right)^2} + \overline{\left(\frac{\partial v}{\partial z} \right)^2} \right]}
 \end{aligned} \tag{3.10}$$

For $\overline{v^2}$, there is no type I production term. The major source term is the pressure-strain correlation (term II) which increases $\overline{v^2}$ by extracting energy from $\overline{u^2}$. This source is balanced primarily by the viscous destruction term (term VI). Finally, the equation for the Reynolds shear stress, \overline{uv} , is:

$$\begin{aligned}
 0 = & \overset{\text{I}}{-\overline{v^2} \frac{\partial \overline{U}}{\partial y}} + \overset{\text{II}}{\frac{p'}{\rho} \left[\frac{\partial u}{\partial y} + \frac{\partial v}{\partial x} \right]} - \overset{\text{III}}{\frac{\partial}{\partial y} (\overline{uv^2})} \\
 & - \overset{\text{IV}}{\frac{1}{\rho} \left[\frac{\partial}{\partial x} (\overline{p'v}) + \frac{\partial}{\partial y} (\overline{p'u}) \right]} + \overset{\text{V}}{v \frac{\partial^2 \overline{uv}}{\partial y^2}} \\
 & - \overset{\text{VI}}{2\nu \left[\left[\frac{\partial u}{\partial x} \frac{\partial v}{\partial x} \right] + \left[\frac{\partial u}{\partial y} \frac{\partial v}{\partial y} \right] + \left[\frac{\partial u}{\partial z} \frac{\partial v}{\partial z} \right] \right]}
 \end{aligned} \tag{3.11}$$

As in Equation 3.9, the major production term for \overline{uv} is term I. Spalart (1988) points out that the pressure-strain term (term II) is primarily responsible for destruction of the shear stress, while the viscous dissipation term (term VI) accounts for very little destruction.

For this study, all normal Reynolds stresses are created from energy extracted from the $\overline{u^2}$ stress. Therefore the production term for $\overline{u^2}$, namely $\overline{uv} \frac{d\overline{U}}{dy}$, is also called the production term. Figure 3.13 shows the $\overline{u^2}$ production profile for all water flows normalized with shear velocity and kinematic viscosity. Also shown on each plot is a line representing production calculated using values of \overline{uv} calculated from Equation 3.7. There is excellent agreement between the calculated and experimental data, except for some scatter for $y^+ < 10$. The data show a peak at about a $y^+ \approx 10$ and peak values of

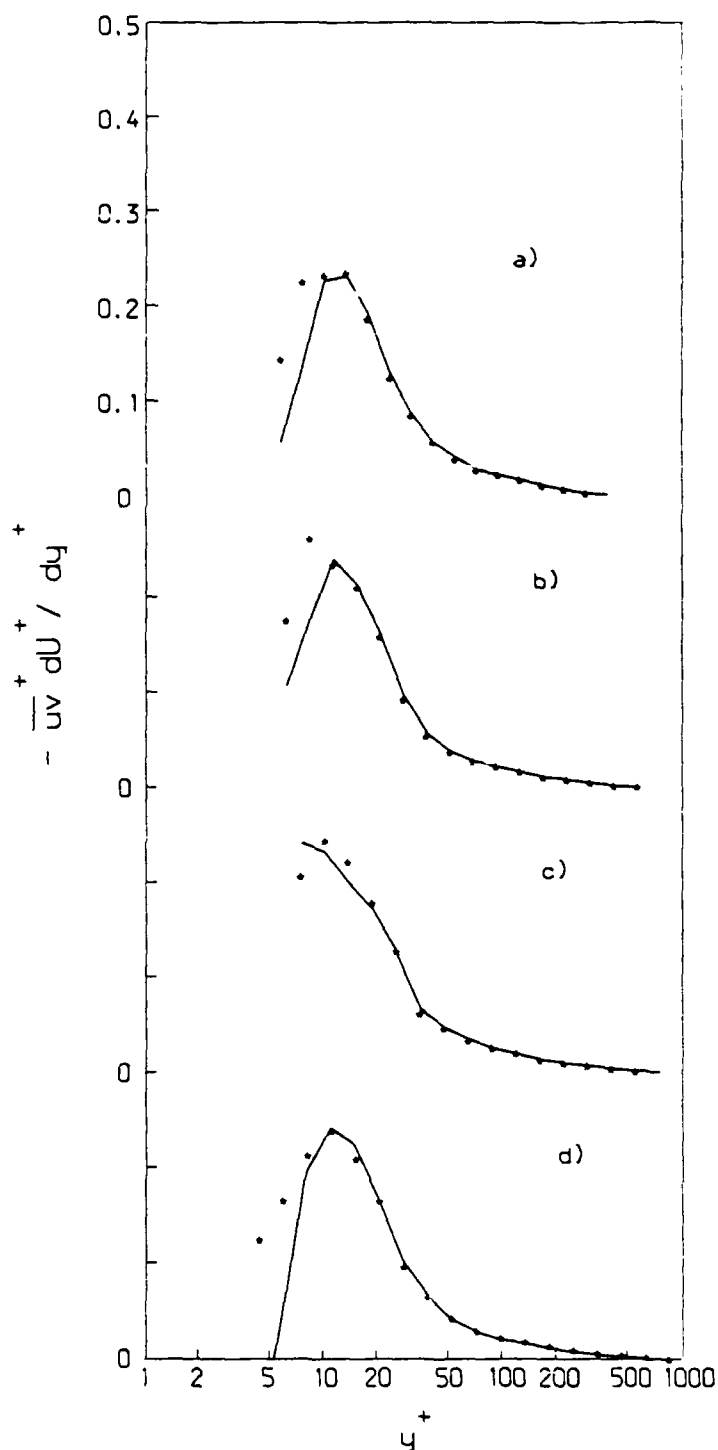


Figure 3.13. $\overline{u^2}$ production profiles for water flows: a) 2.5 cm channel, $Re_h = 14,430$; b) 2.5 cm channel, $Re_h = 20,260$; c) 2.5 cm channel, $Re_h = 30,420$; d) 2.5 cm channel, $Re_h = 34,640$; —, \overline{uv} from Equation 3.7.

2.3–2.4. The data are in good agreement with Spalart (1988). The scatter in data for $y^+ < 10$ is attributed to error in the normal velocity measurements.

Profiles for the production of \overline{uv} are shown in Figure 3.14. The results for the 2.5 cm channel wall strain rates of 1000 s^{-1} and 2500 s^{-1} agree well with those of Spalart (1988) with the peak value of about 0.15 occurring at $y^+ \approx 15$. Results from the 6.0 cm channel yielded a peak of about 0.2 and the high strain rate (4000 s^{-1}) flow in the 2.5 cm channel failed to yield conclusive results due to erroneous measurements of v for $y^+ < 30$.

3.4 Drag-Reduced Flow Results

In order to examine the effect of a dilute polymer solution on the turbulent structure, two-component velocity measurements were made at each of the flow conditions in the factorial experimental design. Most of the drag-reducing flows of polymer solutions differ from the water flows in the same general way. However, as mentioned in Section 3.2, for the drag-reduced flow at 4000 s^{-1} and 5 ppm the viscous and Reynolds stresses did not add up to the total shear in the region of $y^+ < 100$. The results presented here include those of a typical drag-reduced flow and those of the strongly non-Newtonian flow (4000 s^{-1} , 5 ppm) so that the similarities and differences of this strongly non-Newtonian flow can be seen. The typical drag-reduced flow is at a wall strain rate of 1000 s^{-1} , a polymer concentration of 3 ppm and drag reduction of 27%. Other polymer data were used to establish trends for the profile deviations. The kinematic viscosity used for normalization of the drag-reduced flows was that of water at 22° C , which is $0.96 \times 10^{-6} \text{ m}^2/\text{s}$.

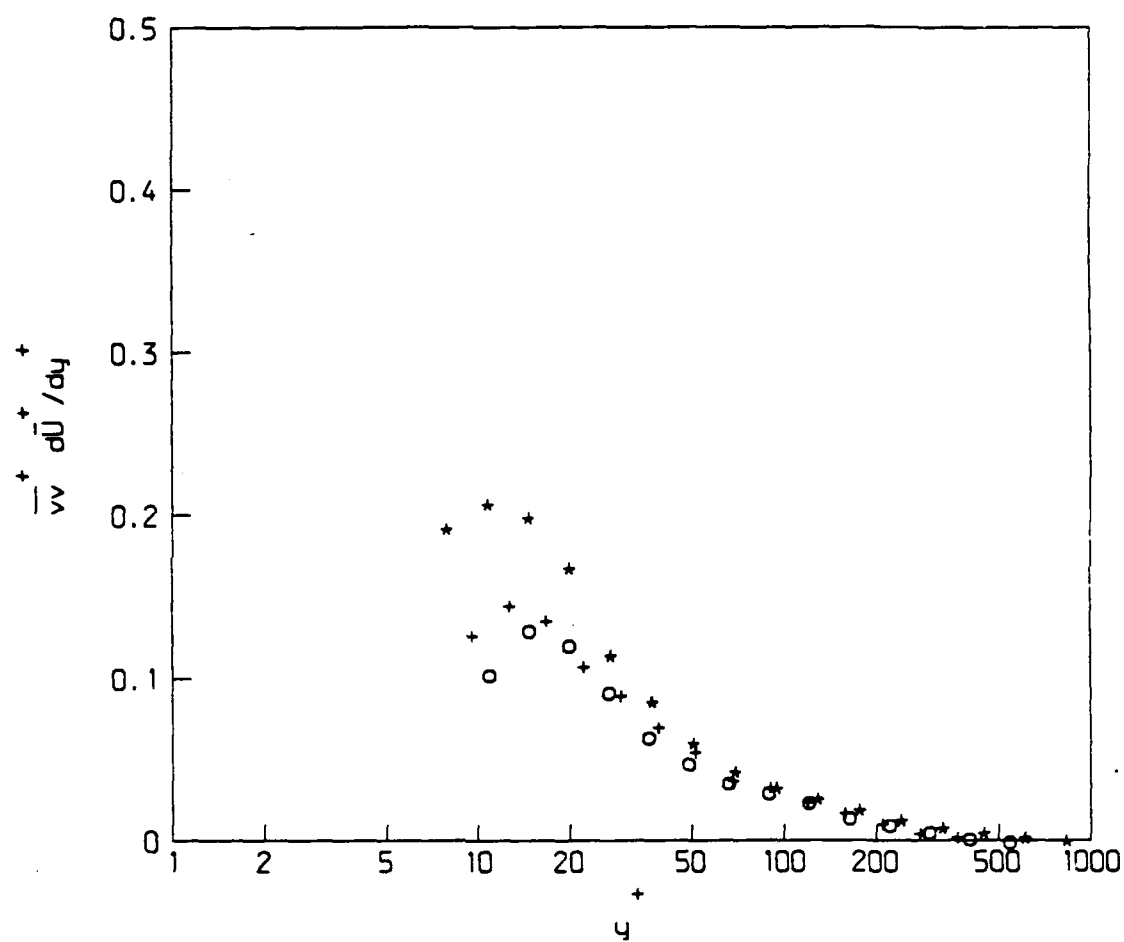


Figure 3.14. $\overline{v'w'}$ production profiles for water flow: +, 2.5 cm channel, $Re_h = 14,430$; o, 2.5 cm channel, $Re_h = 20,260$; *, 6.0 cm channel, $Re_h = 34,640$.

3.4.1 Mean velocity

Figure 3.15 shows the effect of polymer addition upon the mean velocity profile. As shown by Reischman and Tiederman (1975), the buffer zone thickens and offsets the logarithmic zone correspondingly. As can be seen, the results from the typical flow and the strongly non-Newtonian flow agree in trend, although the slopes and offsets of the two vary. This is expected since there are different amounts of drag reduction. In order to be as objective as possible, the method of Sreenivasan (1988) was used as a guide to establish where, if at all, the logarithmic zone exists. This method was not conclusive for the drag-reduced flows. Instead, if a straight line could be drawn through at least four data points for $50 < y^+ < 300$ plotted in semi-log u^+, y^+ coordinates, a logarithmic region was assumed to exist. A regression analysis performed with these data yielded the slope, $\frac{1}{\kappa}$, and the intercept, B , of the log-law, $U^+ = \frac{1}{\kappa} \ln y^+ + B$. This form of the log-law was assumed to hold for all drag-reduced flows. Coles (1968) suggests that this method is as good as any in determining the log-law constants. As can be seen on Figure 3.15, the fitted line (dashed) agrees with the data in the outer flow. Values of κ and B are shown in Table 3.1. Figure 3.16 shows that κ decreases in a linear fashion with drag reduction.

Since definition of the log zone is somewhat subjective, other experimenters have assumed that the slope is the same for water flows and drag-reduced flows. This assumption creates the idea of a parallel shift upward of the log zone in drag-reduced flows. For the data in the present study, however, if the constant slope assumption is used, the fitted line will not pass through more than two data points.

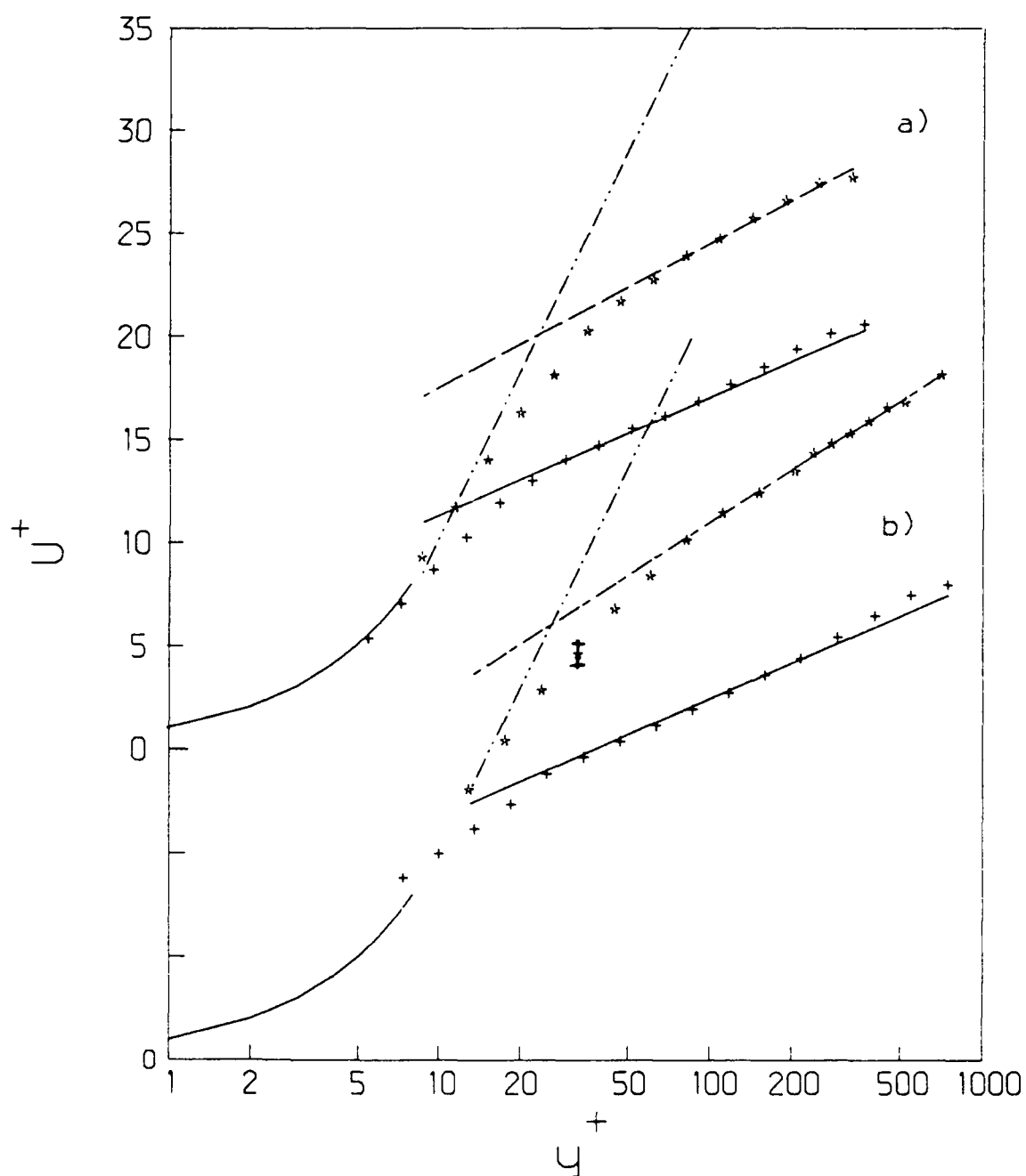


Figure 3.15. Mean velocity profiles: a) typical drag-reduced flow; b) strongly non-Newtonian drag-reduced flow; *, drag-reduced data; +, water flow data at equal wall shear; —, standard law of the wall; ---, fitted law of the wall; - · - ·, Virk ultimate asymptote.

Table 3.1. Parameters for the log law, $U^+ = \frac{1}{\kappa} \ln y^+ + B$.

channel (cm)	$\frac{d\bar{U}}{dy} \Big _w$ (s^{-1})	\bar{C} (ppm)	κ	B	%D κ	Re _h
2.5	1000	3	0.33	10.5	27	16,750
2.5	1000	5	0.34	11.1	34	17,460
2.5	2500	4	0.28	8.5	39	31,200
2.5	4000	3	0.30	8.0	35	39,310
2.5	4000	5	0.27	8.9	40	41,610
6.0	1000	3	0.38	5.7	11	37,070
6.0	1000	5	0.38	6.2	15	37,630

3.4.2 Second Moments

Figure 3.17 shows a comparison of the streamwise and wall-normal, RMS, velocities of the 3 ppm polymer flow with a water flow, both at a wall strain rate of 1000 s^{-1} . The peak in u'^+ broadens and moves outward from $y^+ = 15$ to $y^+ = 30$. These results agree in trend with those of Luchik (1988) and Reischman and Tiederman (1975). However, the peak in u'^+ is about 12% higher than both Luchik and Reischman and Tiederman's value but it agrees with the measurements of McComb and Rabie (1982). For $y^+ < 100$, the drag-reduced flow shows a damping of v'^+ . These results are consistent with those seen by Luchik (1988). As in the water flow cases, the v' results for $y^+ \leq 10$ appear to be high and are therefore questionable. As in the case of the mean velocity profiles, the typical and strongly non-Newtonian flows also showed similar trends in the RMS velocities. All other 2.5 cm channel drag-reduced results in this study exhibited the same trends, although some results showed more scatter in v' . The 6.0 cm channel results were similar in trend to those of the 2.5 cm channel, but since the drag

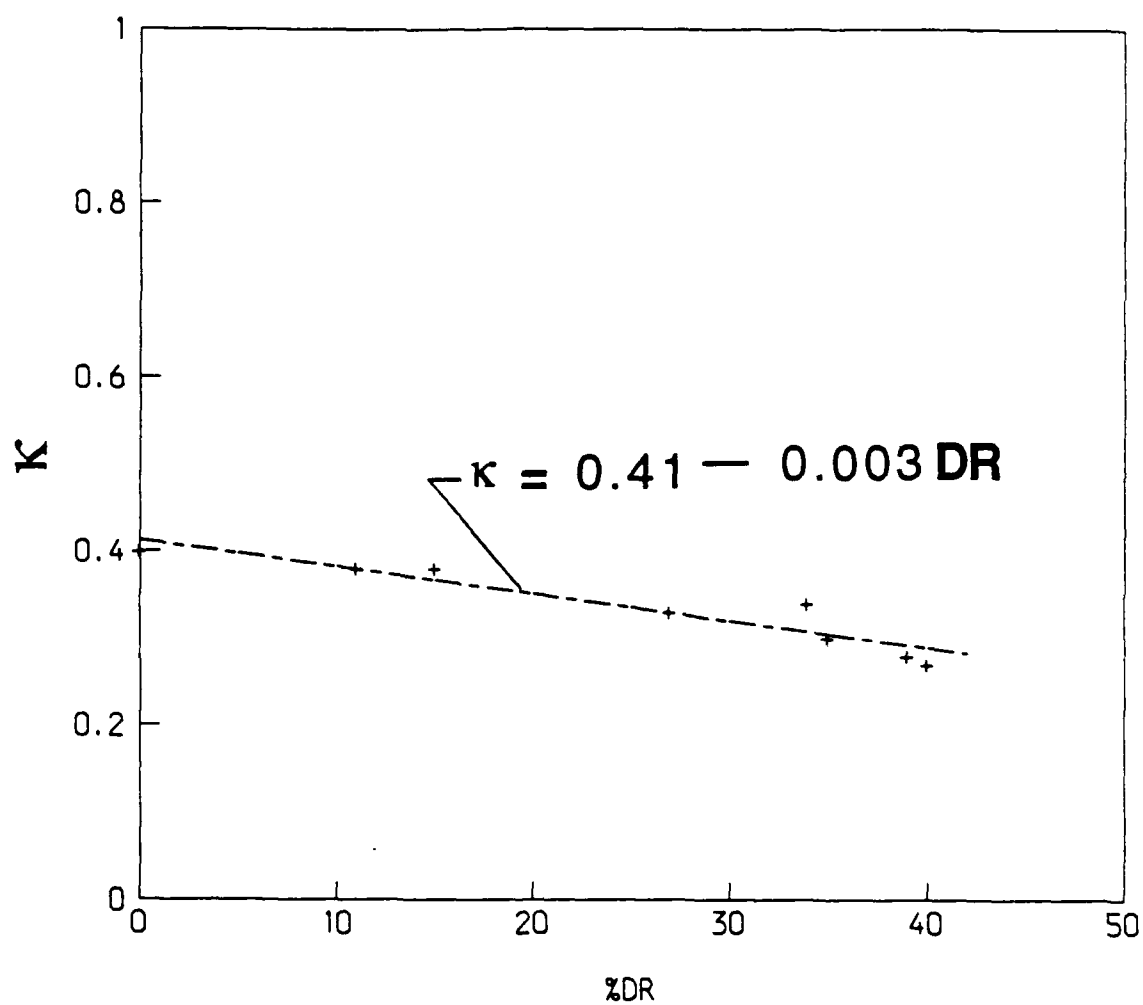


Figure 3.16. Dependence of the reciprocal of the log-law slope on drag reduction.

reduction was low, the change in the statistics was not as pronounced.

Since it has been shown that drag reduction depends upon wall strain rate and average polymer concentration, it is desirable to see if the turbulent quantities that change in a drag-reduced flow depend explicitly upon the same variables. Figure 3.18 shows the y^+ location for the peak in u'^+ for the 2.5 cm channel data on the familiar factorial design plot. A linear model fit to the data yields:

$$y^+_{u'p} = 27.2 + 2.5X_1 + 0.5X_2 \quad (3.12)$$

where $y^+_{u'p}$ is the y -location of the peak in u' . However, the F-test reveals that the influence of the coefficients in this model is no greater than the effect of error in measurement. This signifies that the peak location in u'^+ is not strongly, if at all, dependent upon wall strain rate or average polymer concentration. Due to difficulty in determining the peak v'^+ location, no similar modeling was attempted. When the peak location of u'^+ is plotted as a function of drag reduction, as in Figure 3.19, it is clearly evident that the peak in u'^+ moves away from the wall with increasing drag reduction. The evidence suggests that the location for the peak in u'^+ depends upon drag reduction rather than the variables upon which drag reduction depends.

The turbulent shear stress distribution for the drag-reduced flow is shown in Figure 3.20 with the corresponding water flow at equal τ_w . This plot shows that the turbulent stress in drag-reduced flows follows the same trends as in the water flow. This helps confirm the assumption that many drag-reduced flows are still basically Newtonian flows.

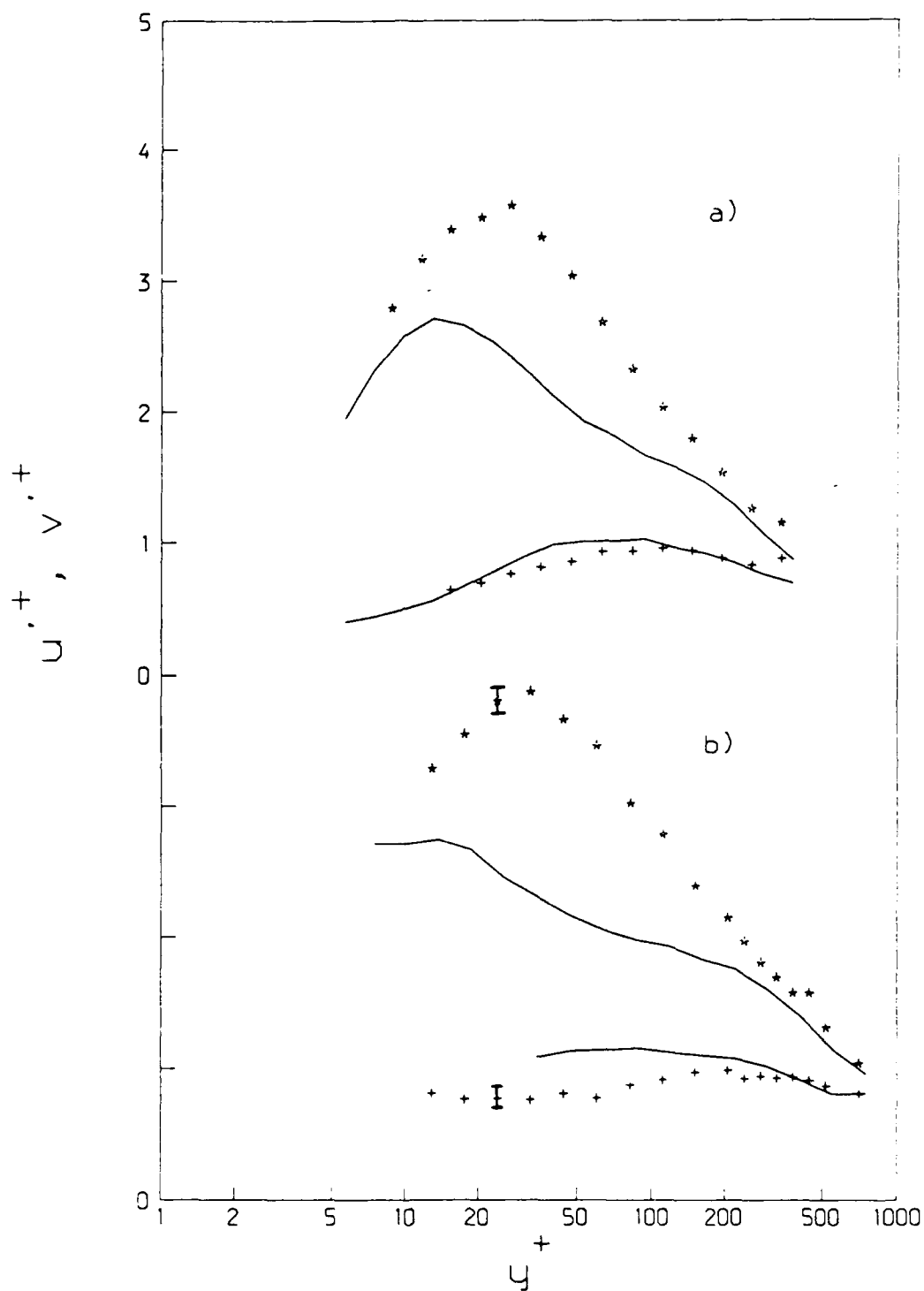


Figure 3.17. Root-mean-square velocities: a) typical drag-reduced case; b) strongly non-Newtonian drag-reduced case; *, u'^+ ; +, v'^+ ; —, water flow at equal τ_w .

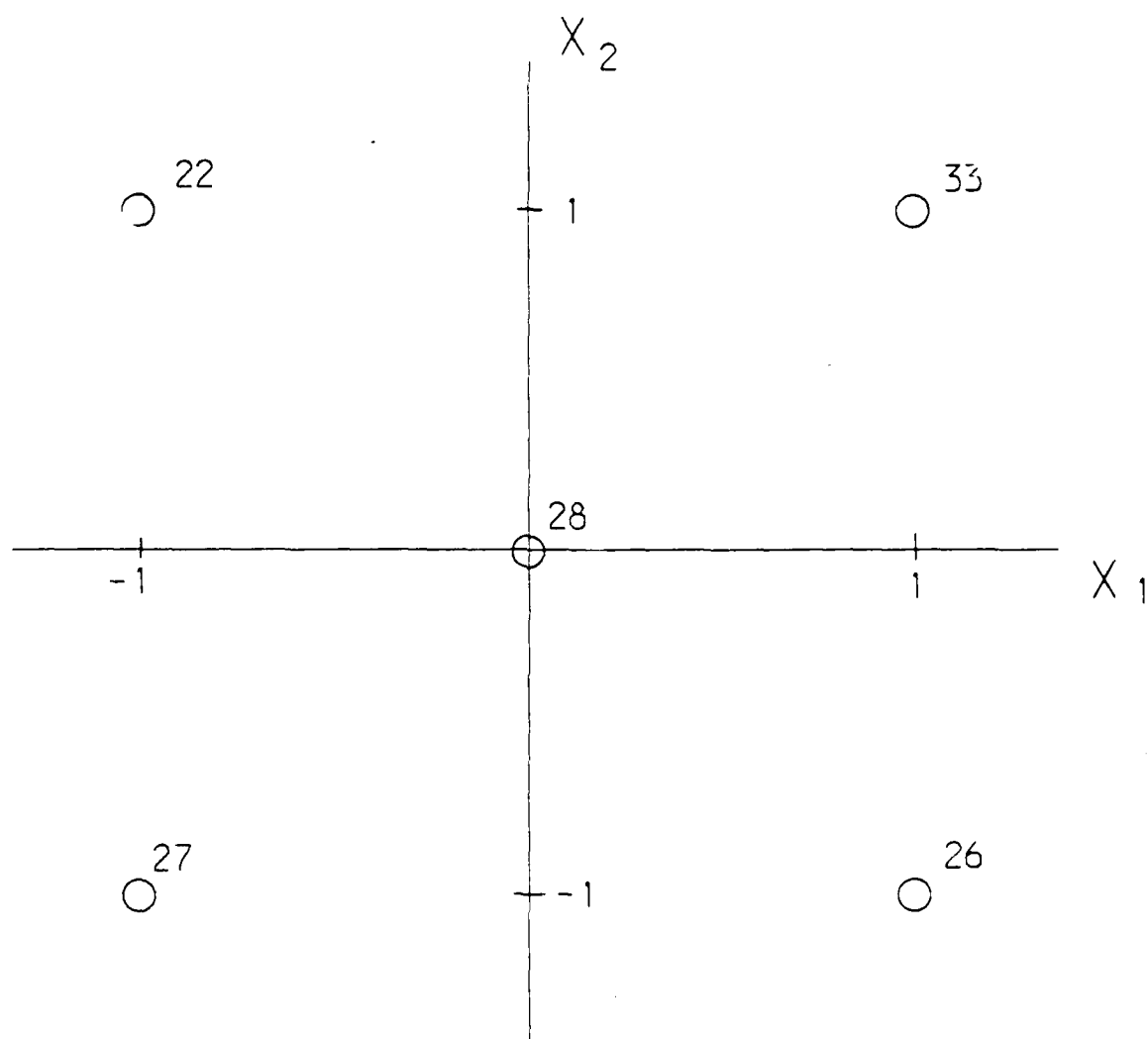


Figure 3.18. y^+ for peak in u' , 2.5 cm channel results only.

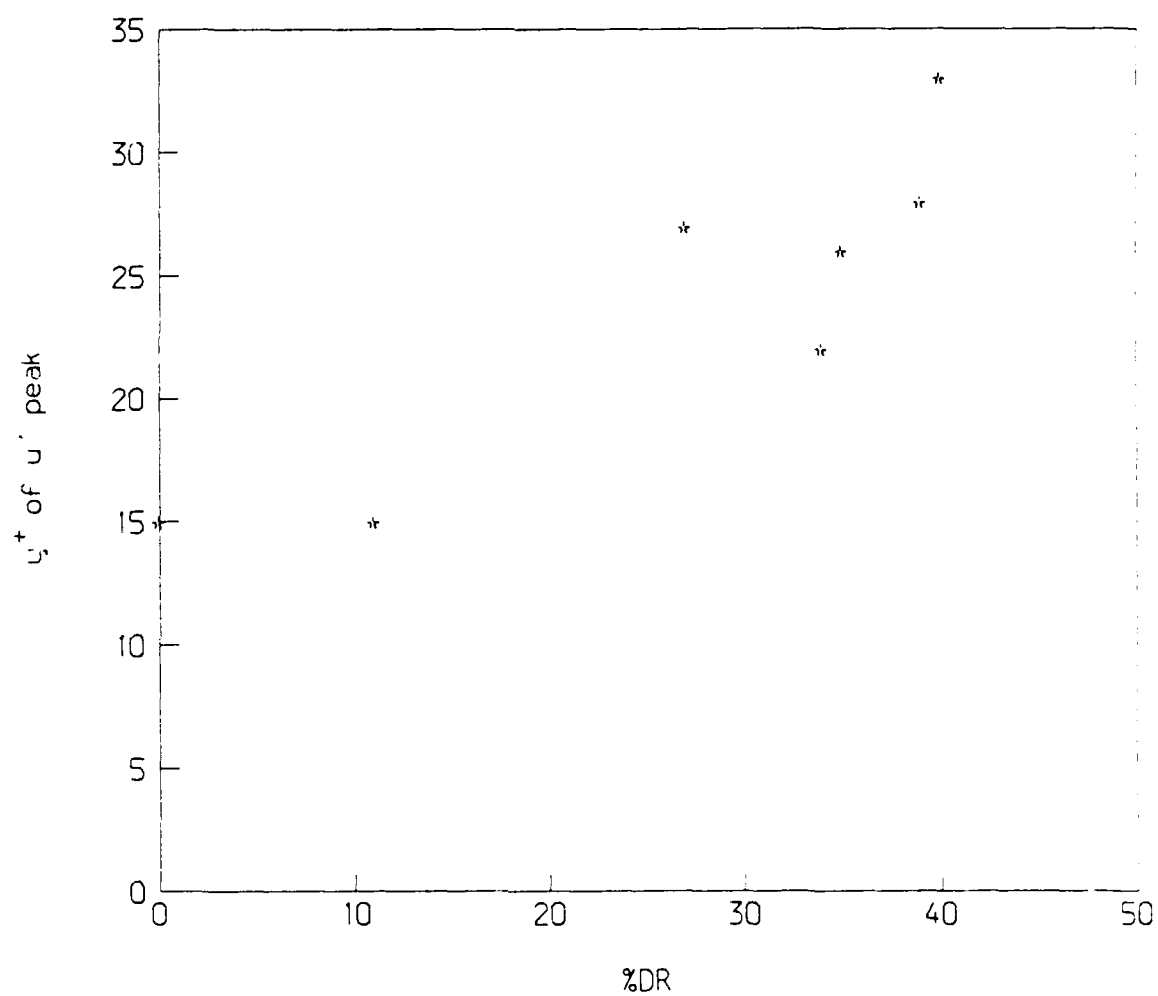


Figure 3.19. Variation of peak location for u'' as a function of drag reduction.

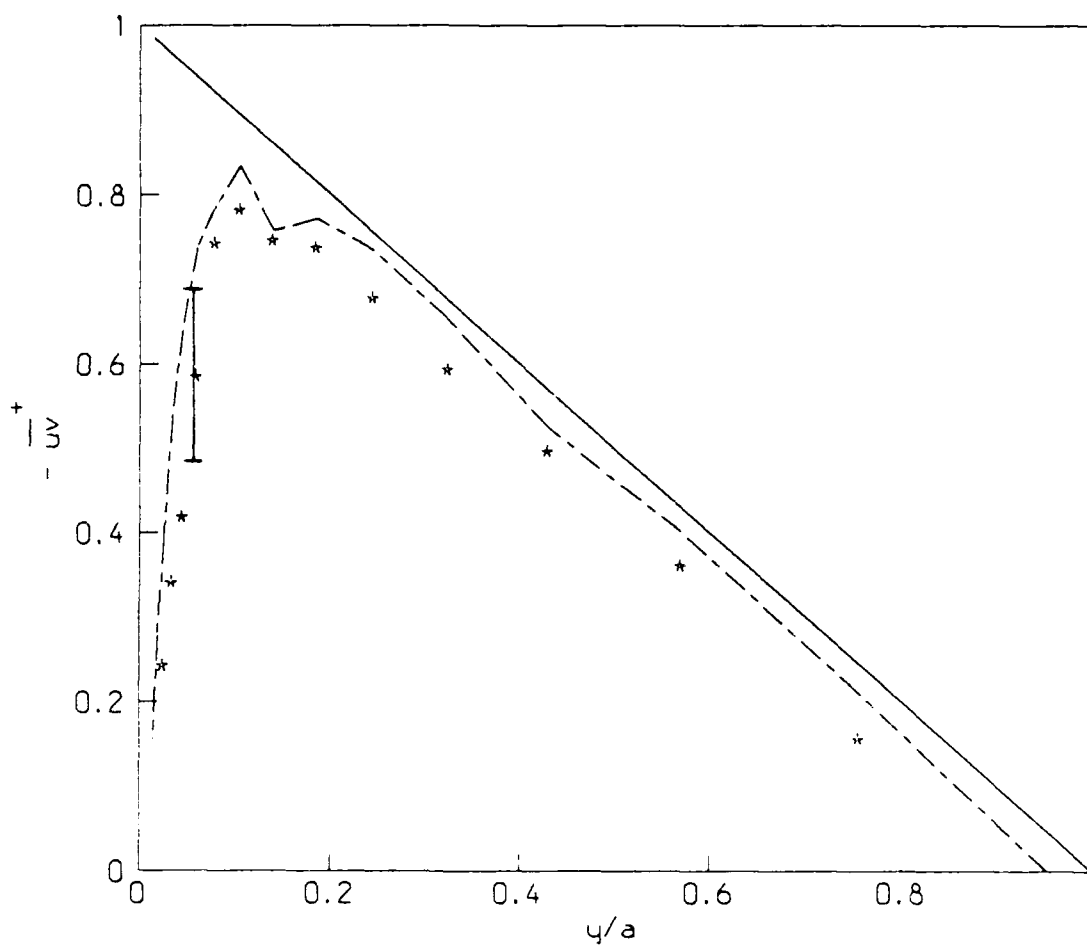


Figure 3.20. Reynolds shear stress distribution: *, typical drag-reduced flow; ---, water flow at equal wall shear stress; —, $\tau_w^+ (1 - y/a)$.

The 2.5 cm channel flow at a wall strain rate of 4000 s^{-1} and average polymer concentration of 5 ppm failed to yield an accurate measurement of τ_w^* as calculated by Equation 2.9. This strongly non-Newtonian flow exhibited the same phenomenon as reported by Willmarth et al. (1987). These features are namely that \overline{uv} behaves as the other drag-reduced flows in the outer portion of the flow. However, as the wall is approached ($y^+ < 100$), \overline{uv} rapidly decreases and the sum of $-\rho\overline{uv}$ and $\mu \frac{d\overline{U}}{dy}$ does not equal τ . Figure 3.21 shows the difference between the sum of the viscous and Reynolds stress and the local shear stress estimated from Figure 3.3 and the streamwise pressure gradient. All of the other velocity statistics, except those that depend upon \overline{uv} (namely production terms) behaved as would be expected from the trends displayed by the typical drag-reduced flows.

The profile of the correlation coefficient, R_{uv} , for the typical drag-reduced flow is shown compared with the R_{uv} for water flow at equal wall shear stress in Figure 3.22. Throughout the whole flow regime, the correlation coefficient is about 25% lower than the water flow values. In plots of the correlation coefficient the difference in behavior of the Reynolds stresses is evident for the flow condition with a wall strain rate equal to 4000 s^{-1} and average polymer concentration of 5 ppm. The correlation coefficient behaves as the typical drag-reduced case in the outer flow, but within $y^+ = 100$ the correlation decreases rapidly as the wall is approached. All other drag-reduced flows behave as the typical case, although the degree of difference between the polymer and water flows may vary. The trend is in agreement with Walker (1988).

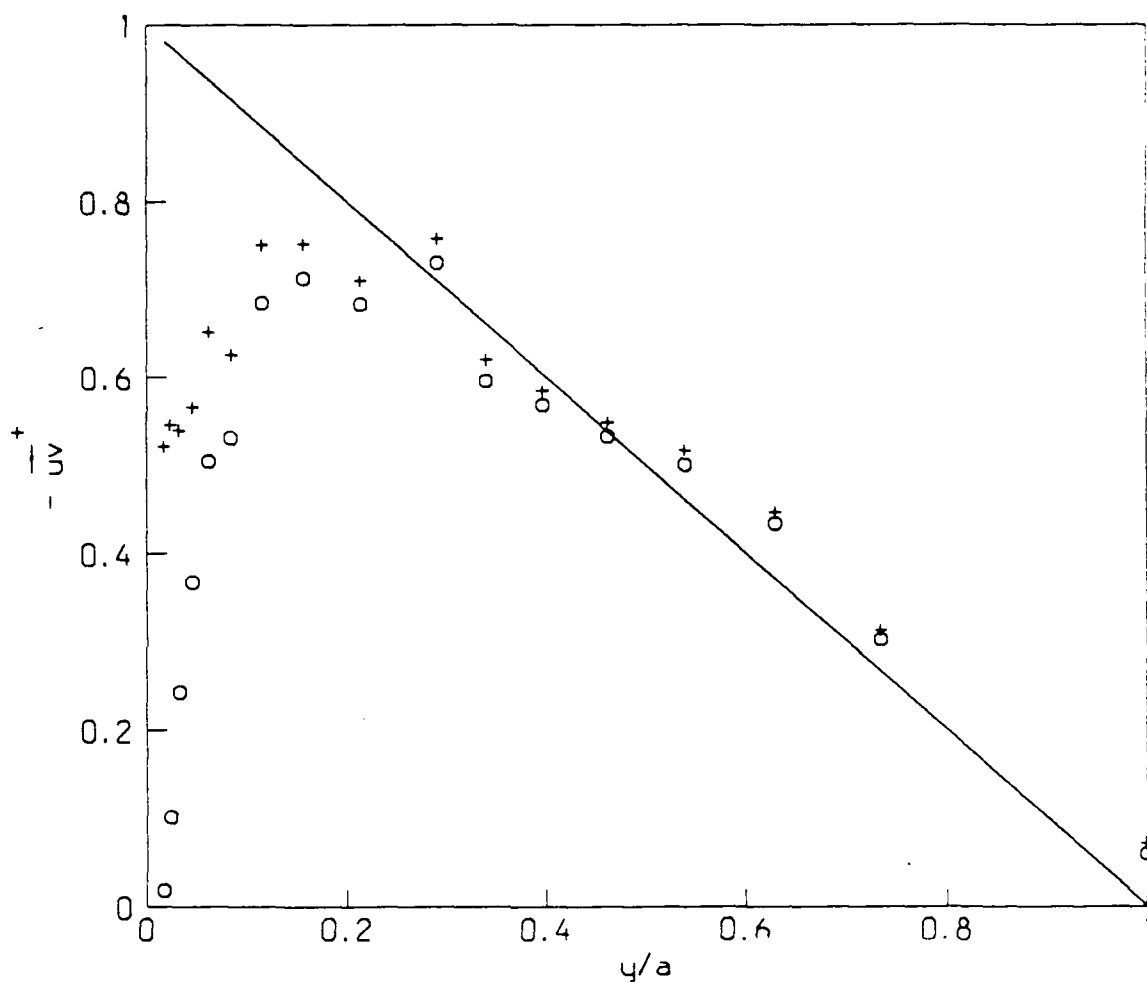


Figure 3.21. Difference in the shear stress as estimated by the sum of the viscous and Reynolds stresses and the streamwise pressure gradient for strongly non-Newtonian flow case: o, Reynolds shear stress; +, sum of Reynolds and viscous shear stresses; —, estimated $\tau_w^*(1-y/a)$.

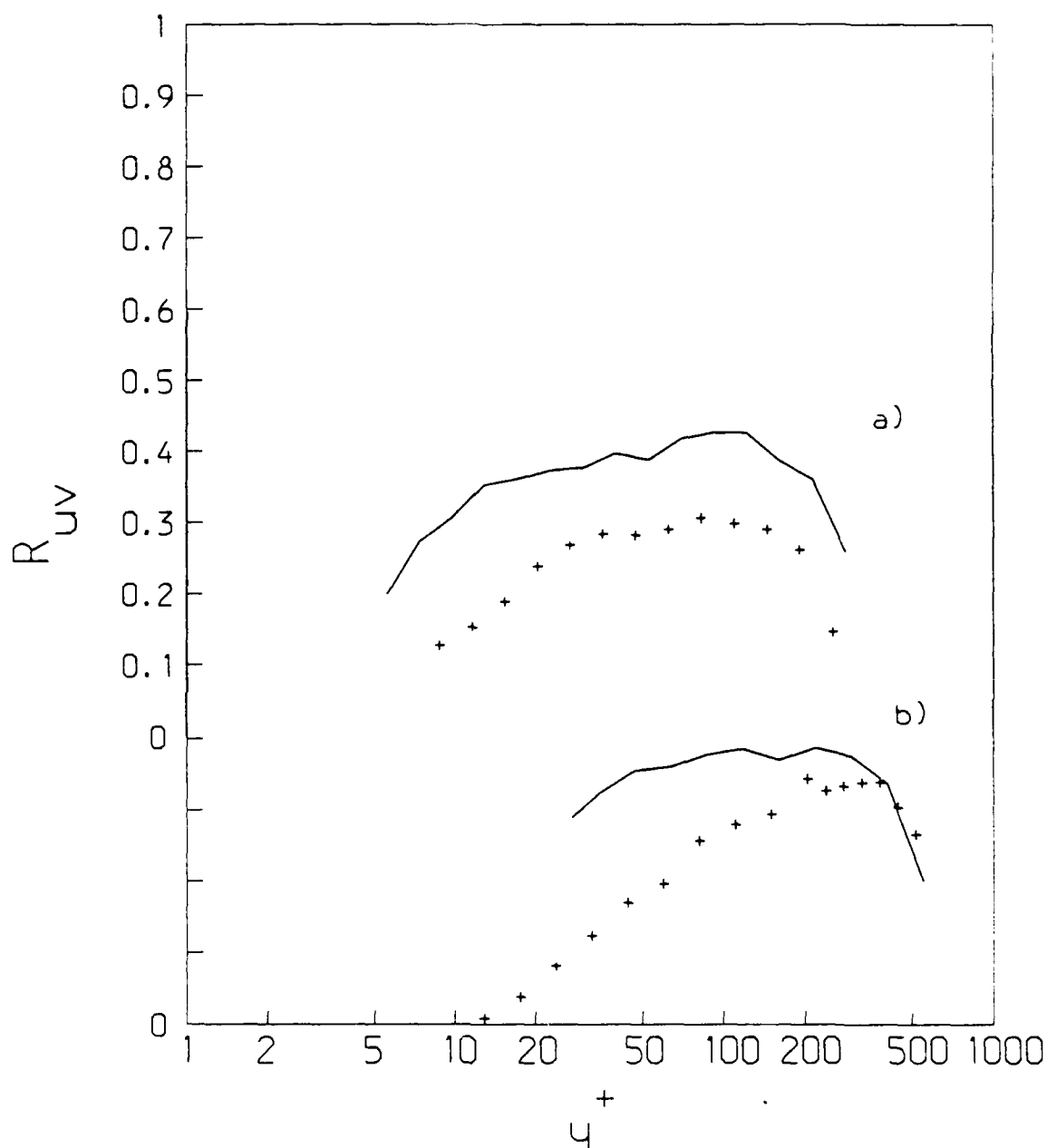


Figure 3.22. Correlation coefficient distribution: a) typical drag-reduced flow ; b) strongly non-Newtonian drag-reduced flow; +, drag-reduced; —, water flow at equal τ_w .

3.4.3 Reynolds Stress Production

Figure 3.23 shows the production of $\overline{u^2}$ for the drag-reduced flow as calculated using experimental results and as calculated using Equation 3.7. There is good agreement between the two results, except in the near-wall region ($y^+ < 10$), where the experimental results appear to be erroneously high. By using calculated values of \overline{uv} in calculating $\overline{u^2}$ production, it is possible to accurately define the peak of production. Figure 3.24 shows a comparison between the typical drag-reduced flow and the equal wall shear water flow. The production peak in the drag-reduced flow has shifted outward from the wall and appears to have broadened somewhat. The peak value, however, is only slightly less than that of the water flow.

As with the RMS results, it is of interest to see if the location of the peak in production of $\overline{u^2}$ depends upon wall strain rate and average polymer concentration. Figure 3.25 shows the peak location (in y^+ units) as it varies on the factorial design space. Fitting a model in the same manner as before yields:

$$y_{pp}^+ = 19.1 + 1.5X_1 + 2.75X_2 \quad (3.13)$$

where y_{pp}^+ is the y -location of the peak in $\overline{u^2}$ production. As with the u^{++} peak, analysis employing the F-test shows that the coefficients for the X_1 and X_2 terms are not statistically significant. If the peak location for $\overline{uv} \frac{d\overline{U}}{dy}$ is plotted against drag reduction, as in Figure 3.26, the resulting trend clearly shows the peak location to be moving away from the wall with increasing drag reduction. Thus, the peak location in $\overline{u^2}$ production is dependent primarily on drag reduction and weakly, if at all, upon those variables

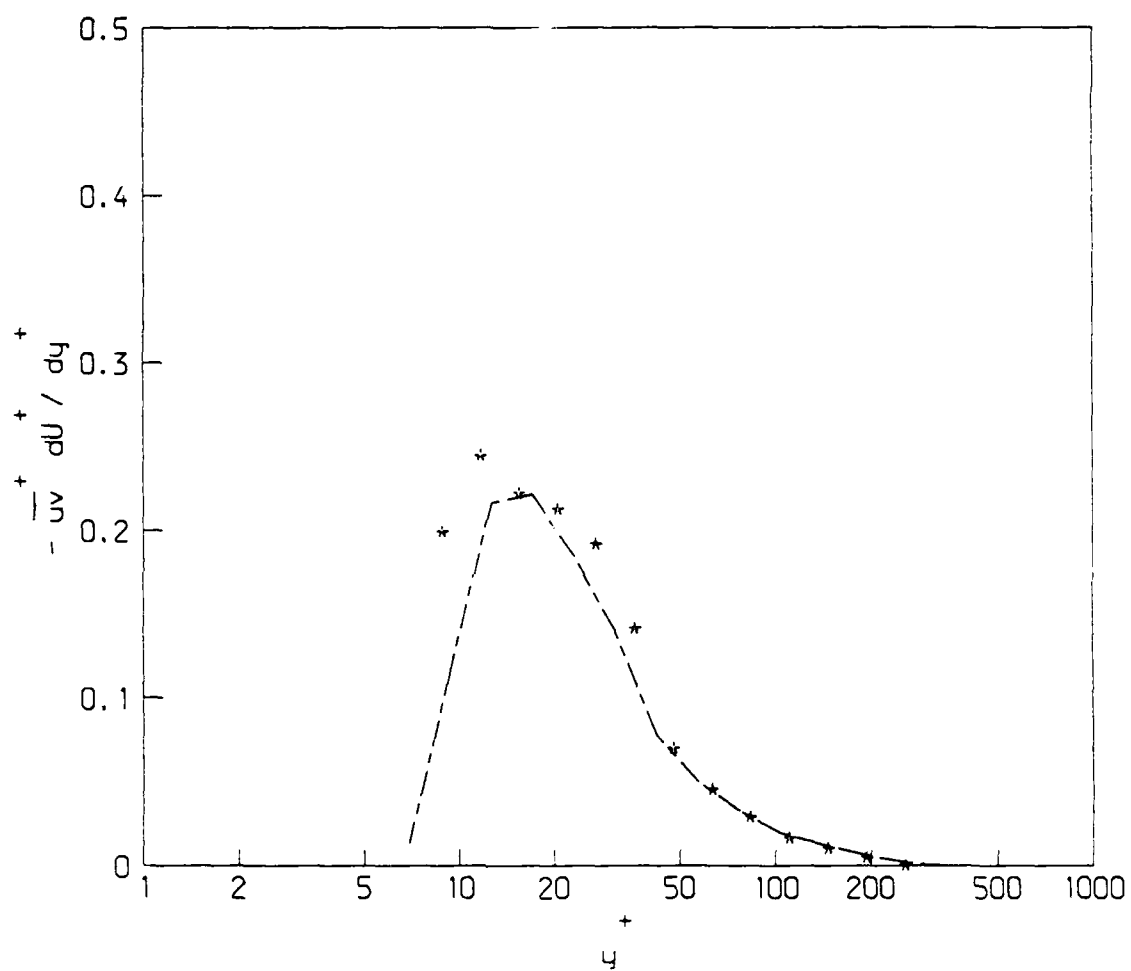


Figure 3.23. $\overline{u^2}$ production for typical drag-reduced flow: *, experimental results; ---, results obtained from calculating \overline{uv} from Equation 3.7

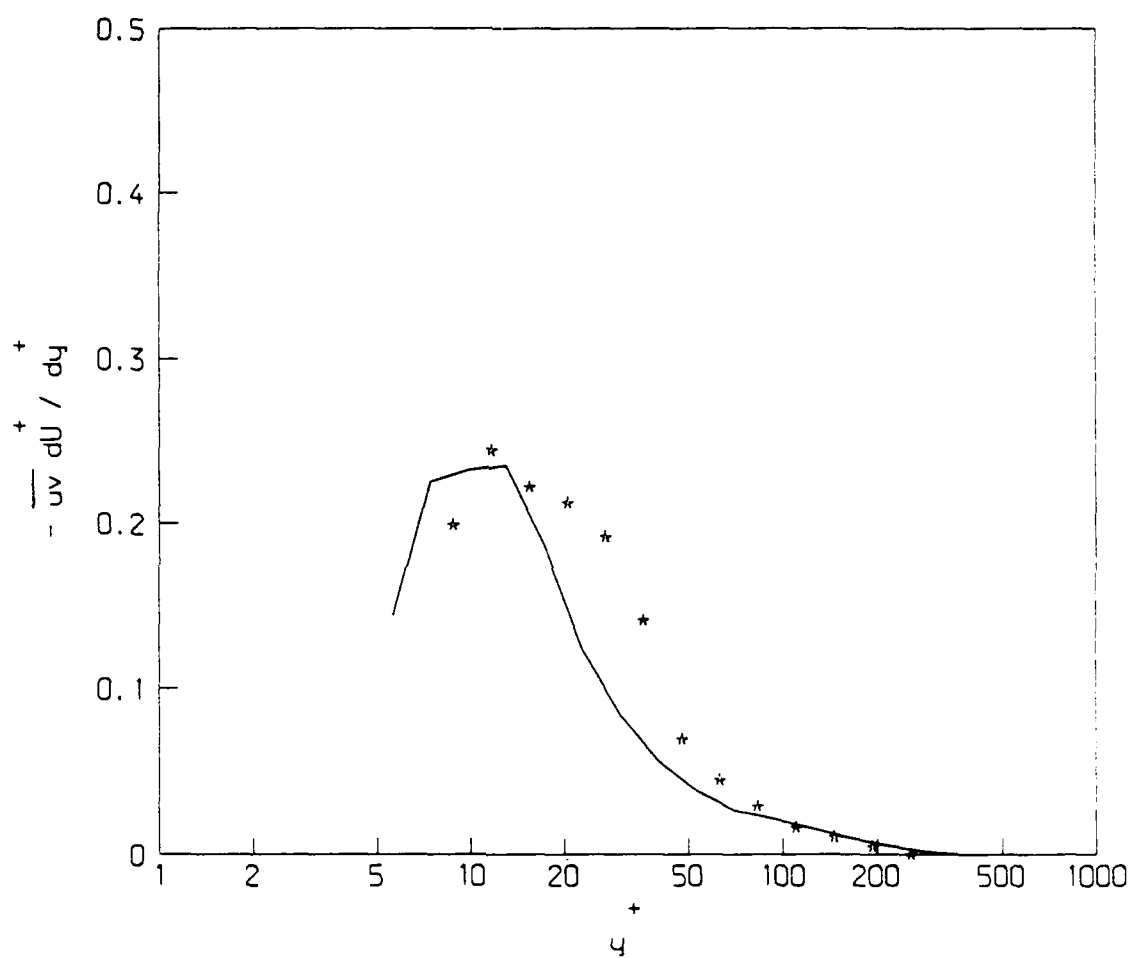


Figure 3.24. $\overline{u^2}$ production profiles for typical drag-reduced flow and water flow at equal τ_w : *, drag-reduced flow; —, water flow.

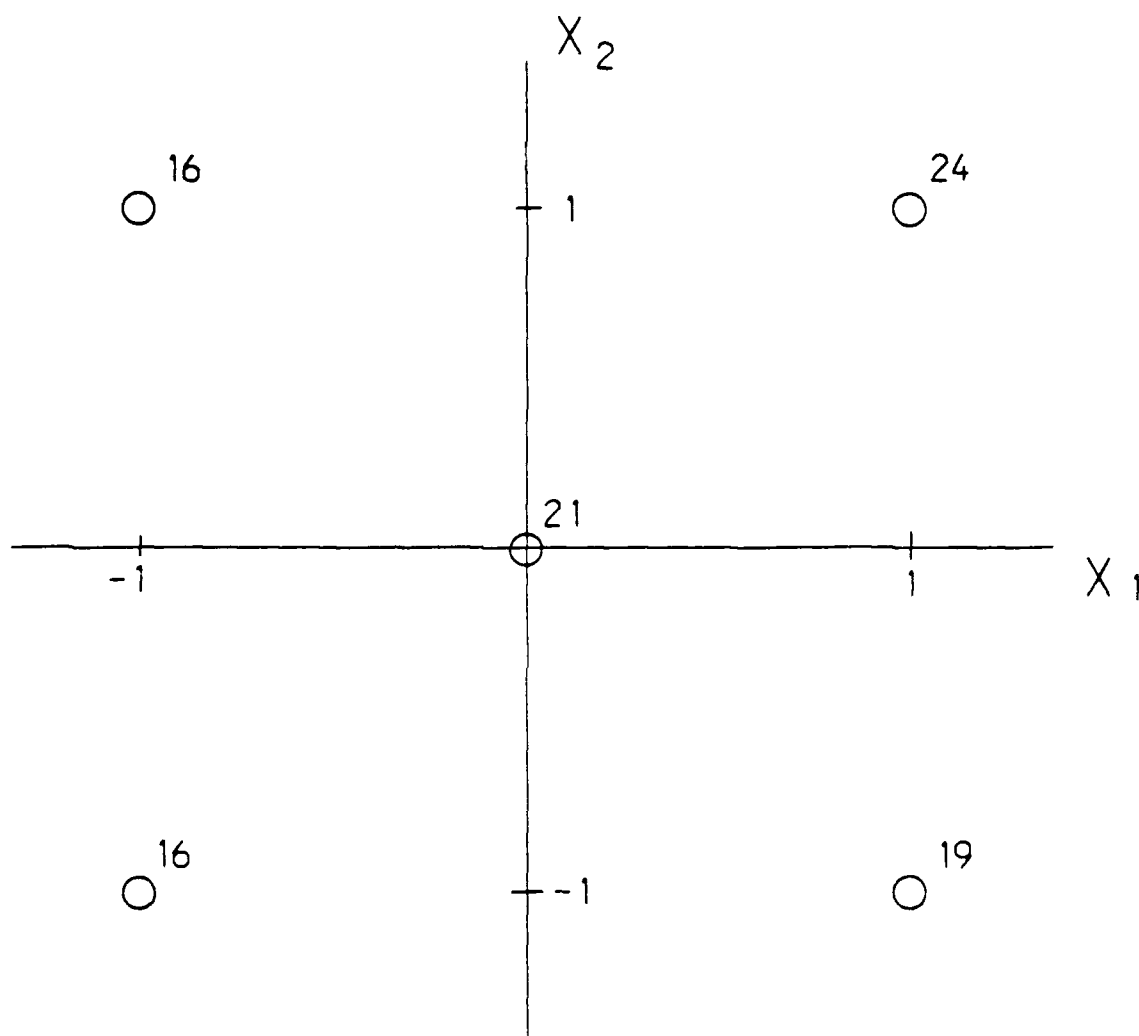


Figure 3.25. y^+ location for peak in $\overline{uv} \frac{d\overline{U}}{dy}$, 2.5 cm channel results only.

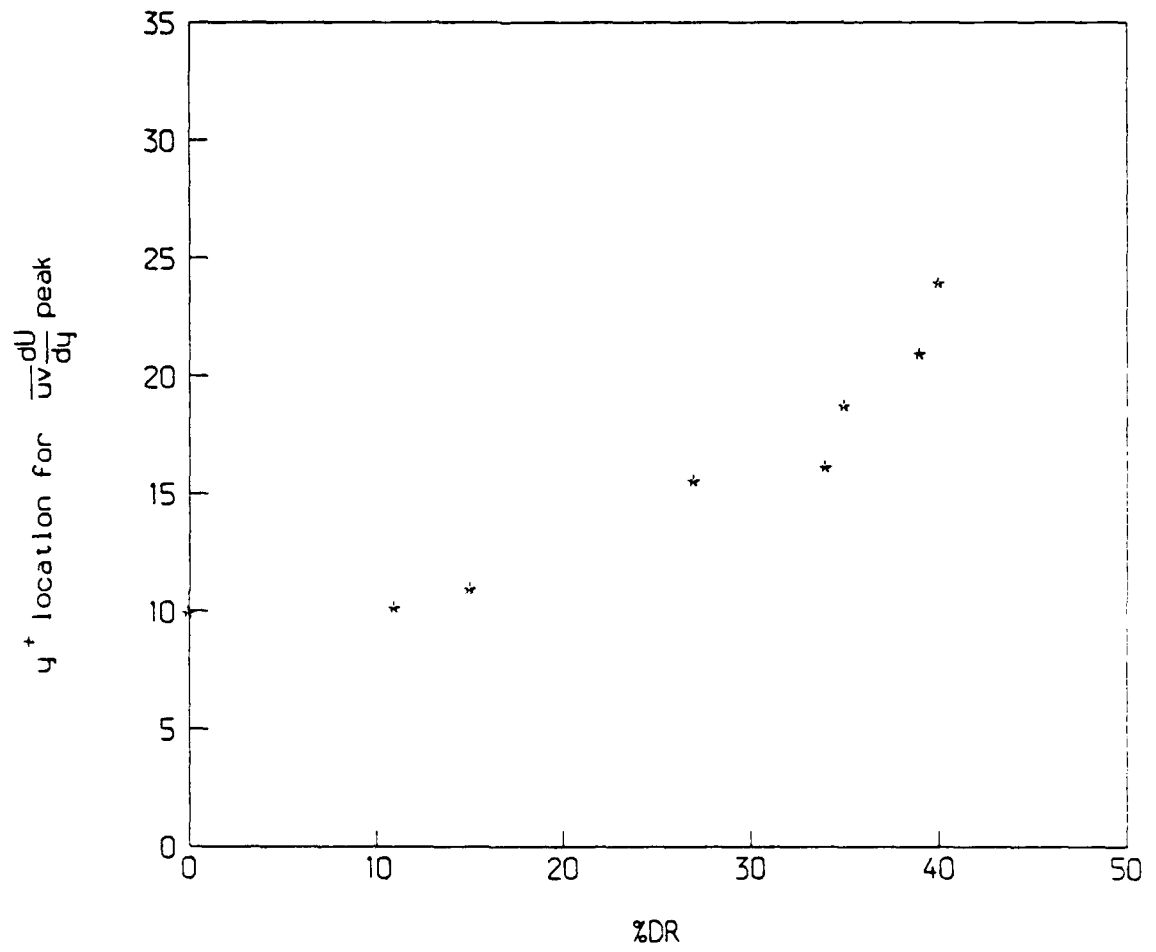


Figure 3.26. y^+ location of the peak value of $\overline{uv} \frac{d\bar{U}}{dy}$ as a function of drag reduction.

upon which drag reduction depends.

Figure 3.27 displays the integrated production profiles normalized by the mass average velocity for all flows. The water flow data fluctuates about a constant value, ≈ 1.3 , for the Reynolds number range shown. This confirms that the mass average velocity is the proper scaling argument. The polymer data, however, scatters widely with Reynolds number, implying that there is another variable upon which the drag-reduced results depend. Also, it is seen in Figure 3.27 that the drag-reduced flows yield significantly lower integrated profiles than the water flows. Plotting the same drag-reduced data as in Figure 3.28 shows that the integrated production profiles have a definite dependence upon drag reduction.

From the integrated $\overline{u^2}$ production profile results, it is clear that turbulence production is lower in drag-reduced flows than in water flows. However, for the same flows, the levels of u'^+ are much higher across the channel while v'^+ is reduced (see Figure 3.17). We now return to the transport equations for the normal stresses, Equations 3.9 and 3.10, to explain this phenomenon. If viscous destruction is increased for the $\overline{v^2}$ (term VI) in Equation 3.10, then there will also be an increase in destruction for the $\overline{u^2}$ (term VI) in Equation 3.9, since the dissipation scales are nearly isotropic. Therefore, to account for this increase in $\overline{u^2}$ and decrease in $\overline{v^2}$, the transfer of energy from $\overline{u^2}$ to $\overline{v^2}$ through the pressure-strain correlation must be inhibited. This behavior agrees with the results of Walker (1988), who points out that this is a valid explanation as long as the polymer does not affect the transport equations or their interpretation.

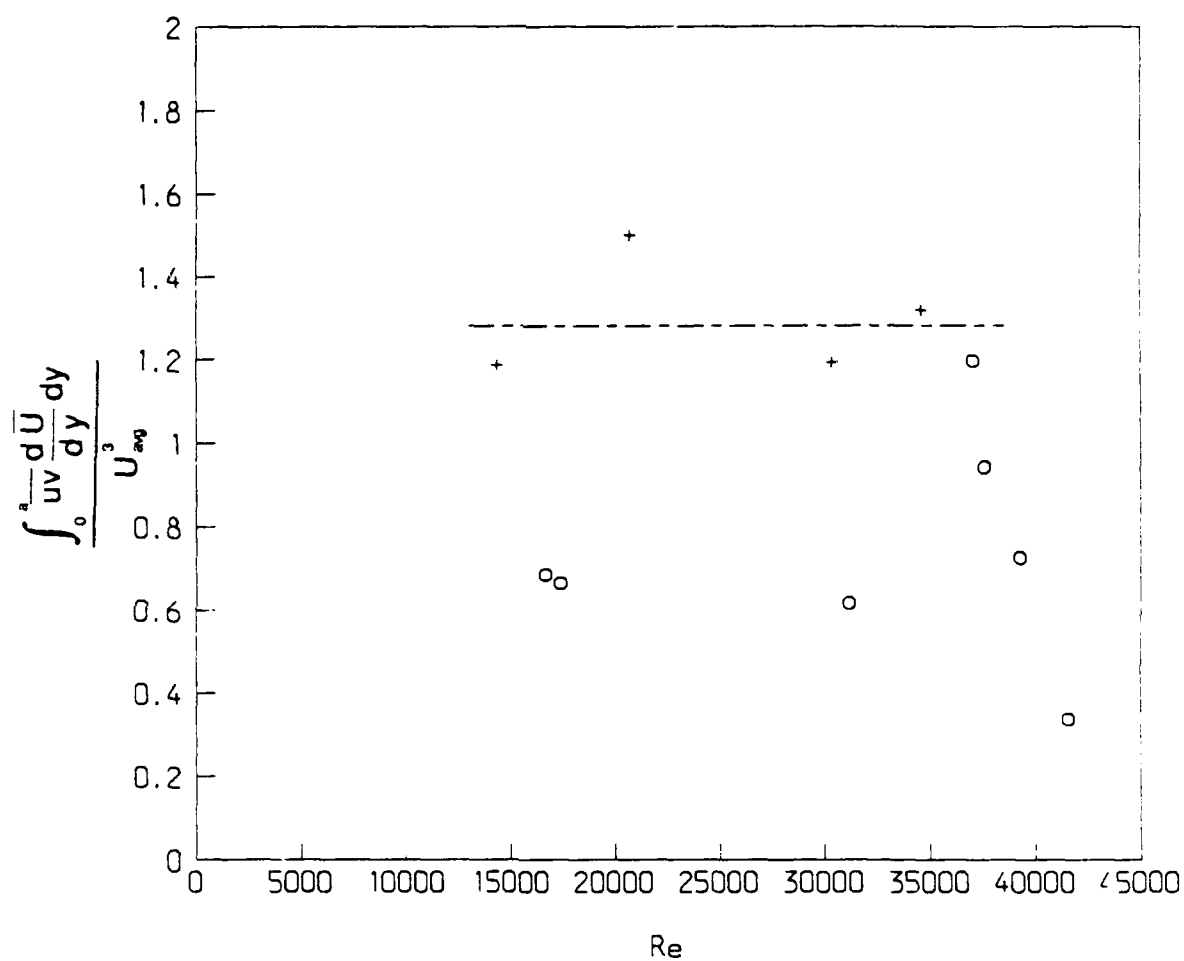


Figure 3.27. Variation of integrated production profiles with Reynolds number: +, water flow; o, drag-reduced flow; ---, $1.3 \pm 15\%$ at 95% confidence.

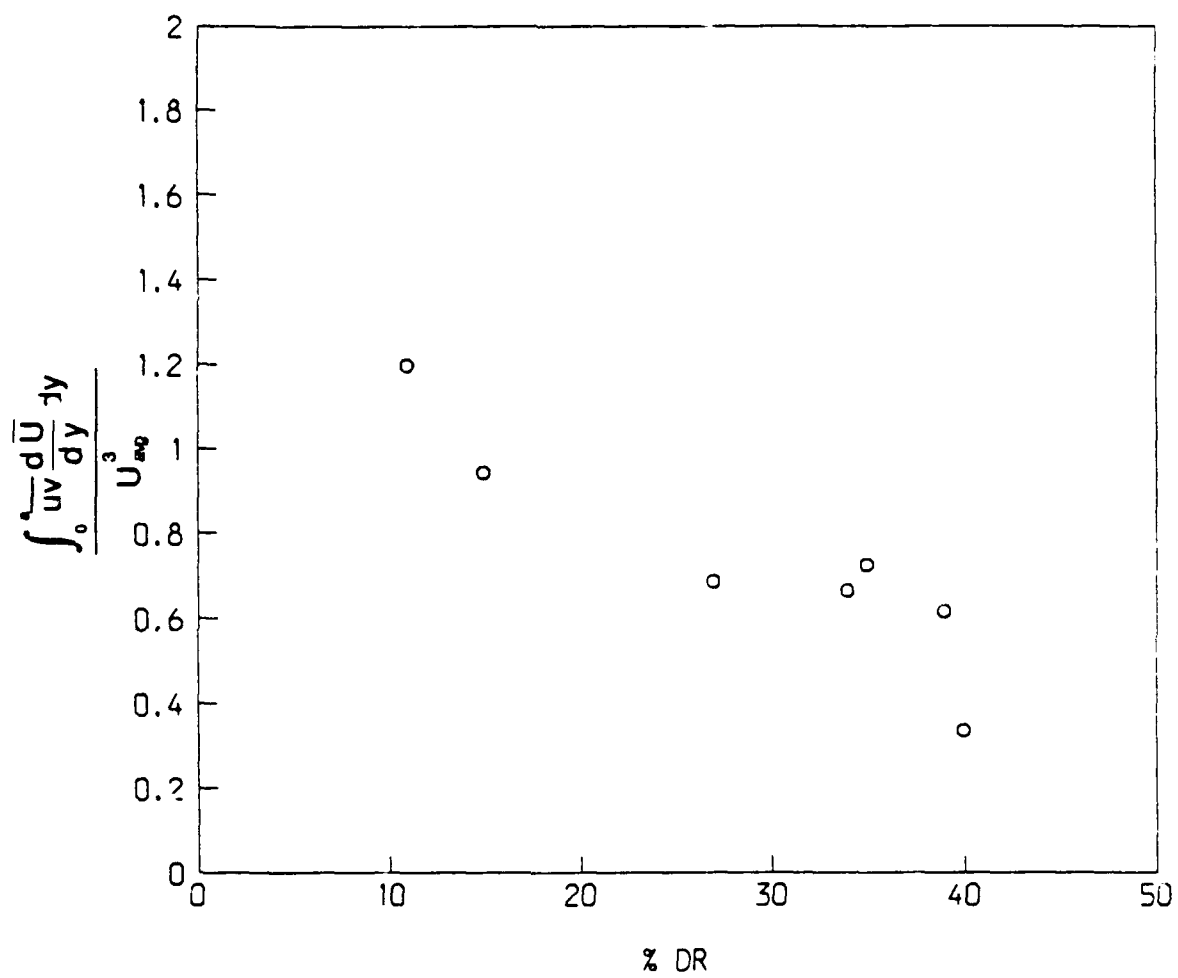


Figure 3.28. Variation of integrated production profiles with drag reduction.

The Reynolds shear stress production profiles are shown in Figure 3.29. Not all of the data are presented here since error in the normal velocity measurement obscured the behavior of the production profiles in some cases. So the flows in which the normal velocity is known to be in error are omitted. From Figure 3.29, it is seen that the drag-reduced flows tend to have a lower Reynolds stress production profile when normalized with a mean velocity. The flow at a wall strain rate of 1000 s^{-1} and an average polymer concentration of 5 ppm deviates from this trend as the wall is approached, but it is possible that the normal velocity may be high. Walker (1988) shows for a inhomogeneous flow that the production of the Reynolds stress increases immediately downstream of the polymer injection. From these results, he concluded that the pressure-strain correlation causes increased destruction of the Reynolds stress. The present results suggest that in a homogeneous flow, since production of the Reynolds shear stress is decreased, the destruction may not be any higher than in a water flow at equal Reynolds number.

3.4.4 Scale-up

One of the objectives of this study was to be able to predict drag reduction in one channel based upon information from a different channel. Granville (1985) proposes a scale-up procedure for pipe flow. This method was to be tested in this study. The details of the derivation of this method can be found in Granville (1985). In order to implement this method, mean velocity profiles were needed (1) to obtain an average velocity and (2) to find the change in the intercept of the log-law. Crucial to the success of this method is the assumption that the slope of the log-law will remain constant. As seen in

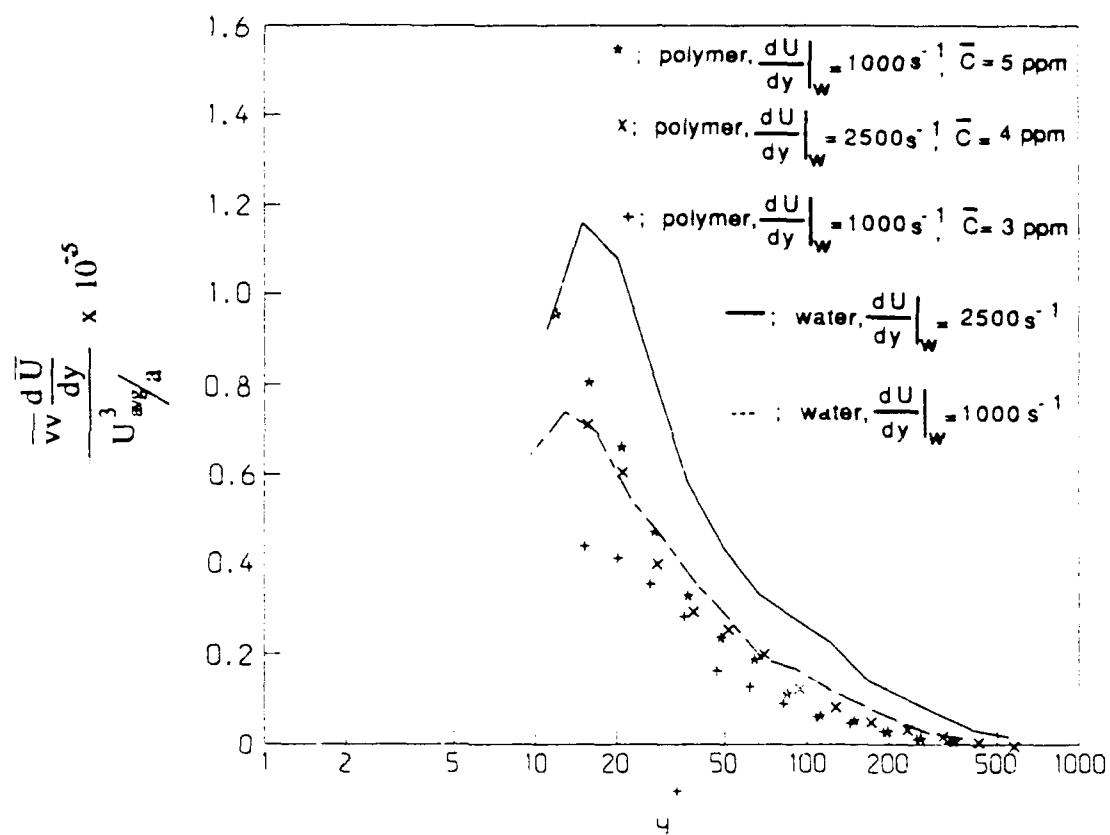
Figure 3.29. \overline{uv} production profiles.

Figure 3.16, the slope increased with increasing drag reduction. Without a constant slope, it was not possible to implement Granville's method. Although no functional form of dependence of drag reduction upon channel height was determined, it was seen that drag reduction differed in two different channels at the same wall strain rate and average polymer concentration, confirming the hypothesis that drag reduction depends on at least the three variables proposed.

3.5 Turbulent Burst Structure

It has been shown by Kim et al. (1971) and Corino and Brodkey (1969) that most of the turbulent kinetic energy and transport occur during the ejection phase of the burst cycle. These ejection events are characterized by a sudden outrush of slow-speed fluid near the wall out into the core of a channel flow. This section deals with the nature of the burst cycle for both water and drag-reduced flows.

In order to acquire data to deduce the mean period of the burst cycle, the time between data points was included in the data so that real-time velocity records could be constructed. Data records were long enough to include approximately 1000 burst periods. These long velocity records were made at each of the factorial design conditions and water records were made at equal wall shear stress to verify the previous Newtonian results obtained by Luchik and Tiederman (1987, 1988). For most velocity records, two components of velocity were measured (U and V) so that the uv quadrant two, $uv|_2$, method of detection could be used. However, due to insufficient, two-component data rates at the highest wall strain rate in the 2.5 cm channel

($\left. \frac{d\bar{U}}{dy} \right|_w = 4000 \text{ s}^{-1}$), only one velocity component, U , was measured. For these records,

the modified u-level detection technique (Luchik and Tiederman, 1987) was implemented.

3.5.1 Description of the detection techniques

The $uv|_2$ technique detects an ejection when the instantaneous uv product is greater than the product of the RMS streamwise and wall-normal velocities and some threshold, H or:

$$|uv|_2 \geq Hu'v'$$

The advantage of this technique is that it detects the physical characteristics of the ejection. A disadvantage is that in the near-wall region where these measurements are made it becomes difficult to attain the data rate required to reconstruct the temporal velocity records.

The modified u-level technique is much simpler than the $uv|_2$ technique, detecting ejections when;

$$u < -Lu'$$

and turning off the detector when,

$$u \geq -.25Lu'$$

where u is the fluctuating streamwise velocity, L is the threshold and u' is the streamwise RMS velocity.

3.5.2 Burst period results

Figure 3.30 show a typical time for the burst period, \bar{T}_B , as a function of the threshold. On this plot, it can be seen that a slight minimum in \bar{T}_B occurs in a region of relative threshold independence, at a threshold of one. According to the criteria of Luchik and Tiederman (1987), this is the correct value of \bar{T}_B for this flow. If a \bar{T}_B versus threshold plot does not exhibit a threshold independent range or at least show a minimum (other than at low thresholds 0.0, 0.2, 0.4) then no value of \bar{T}_B was deduced from that plot. There were four flows that showed such behavior; no value of \bar{T}_B was calculated for these flows. The reason that these flows did not yield values of \bar{T}_B is that the signal to noise ratios for these flows were low (less than 25). One flow was in the 2.5 cm channel, wall strain rate equal to 1000 s^{-1} , and the others were the three 6.0 cm channel flows.

Figure 3.31 shows the effect of Reynolds number upon the burst period normalized with inner variables for water flows. When \bar{T}_B is normalized with u_τ as calculated from pressure drop, the data scatters about $\bar{T}_B^+ = 90$, which is the line prescribed by Luchik and Tiederman (1987). However, when \bar{T}_B is normalized with u_τ calculated from the sum of the viscous and turbulent stresses (Equation 2.9), a new line, $\bar{T}_B^+ = 71$ fits the data. As can be seen, the current results are in agreement with those of Luchik and Tiederman (1987) and Walker (1988).

Figure 3.32 shows the variation in the ratio of the average burst period for polymer flows, \bar{T}_{BP} , to the average burst period of water flow, \bar{T}_{BW} , at equal wall shear stress with the amount of drag reduction in the polymer flow. Included are Luchik's

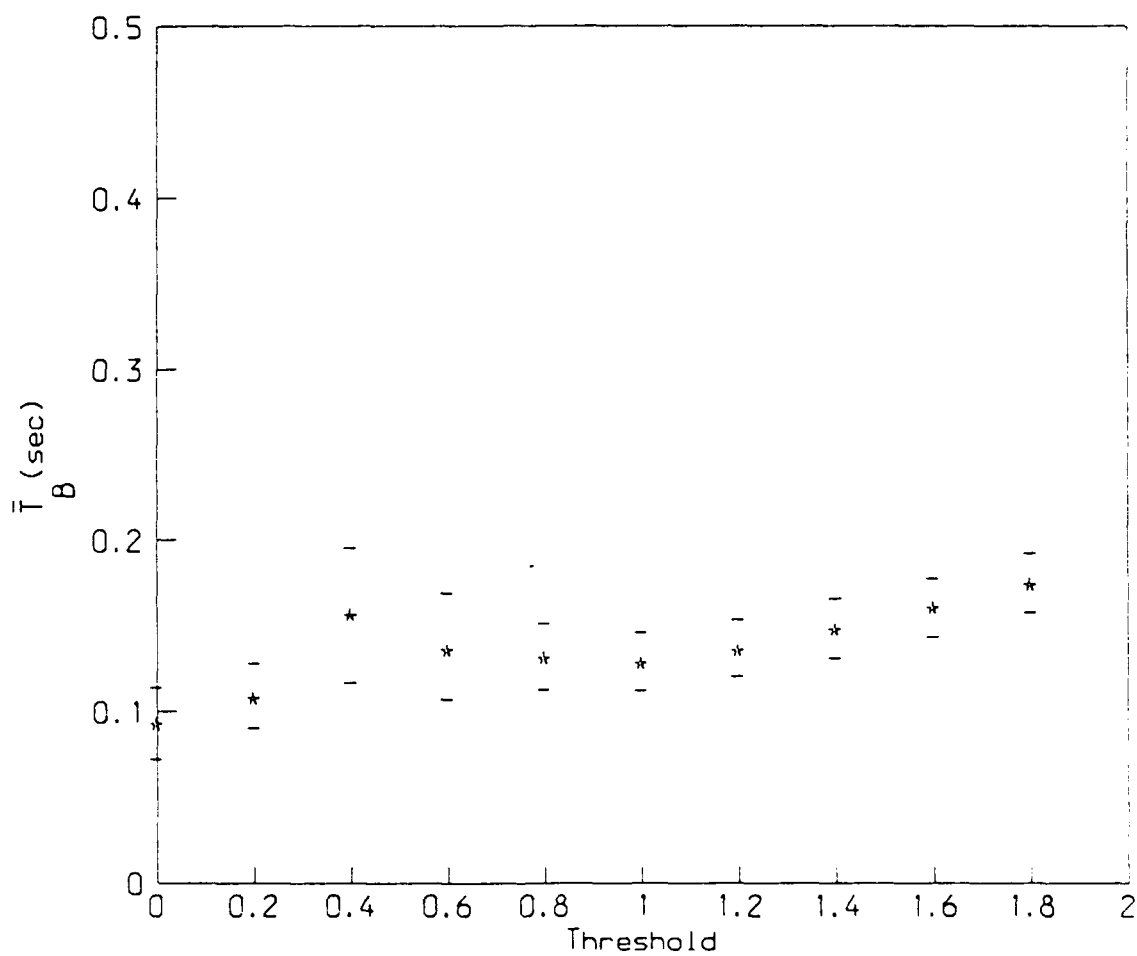


Figure 3.30. Typical mean burst period as a function of threshold; 2.5 cm channel.
 $\left. \frac{d\bar{U}}{dy} \right|_w = 1000 \text{ s}^{-1}$, $\bar{C} = 3 \text{ ppm}$.

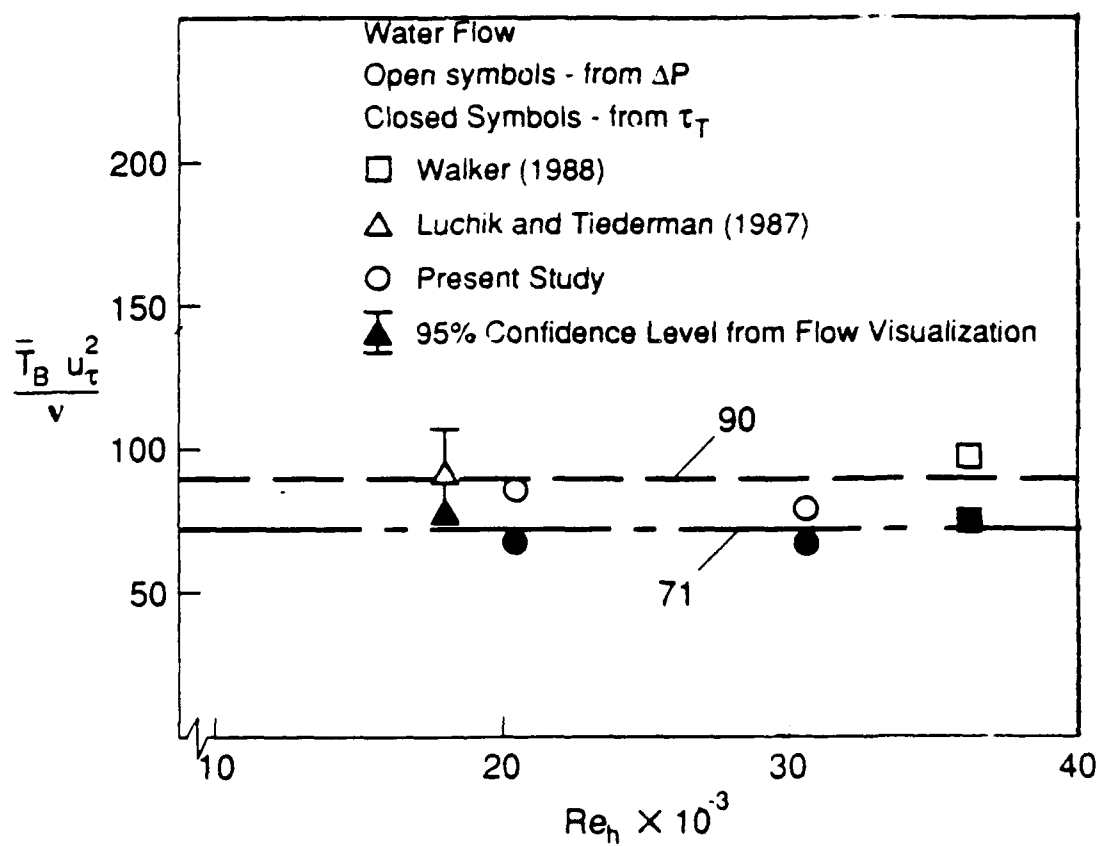


Figure 3.31. Burst period for water flow with inner scaling as a function of Reynolds number.

(1985) modified u-level and $uv|_2$ results with estimated error bounds. The data appear to follow the trend described by Luchik and Tiederman (1988) that an increase in the ratio of the polymer and water burst periods corresponds with the increase in streak spacing (see Oldaker and Tiederman 1977). Thus, the present results would support Luchik and Tiederman's conclusion that the bursting rate from a streak in a low concentration polymer flow is the same as that of a water flow.

Figure 3.33 displays the ratio of polymer to water burst periods (at equal wall shear stress) on the factorial design plot. Regression of the data provides the model:

$$\frac{T_{BP}}{T_{BW}} = 1.72 + 0.22X_1 - .01X_2.$$

However, F-test analysis of the model shows that the model's prediction are no better than the random error. From these results, it is seen that changes in the burst cycle are affected mainly by drag reduction. Stated in another way, a certain drag reduction will yield a certain burst period ratio, regardless of how that level of drag reduction was obtained.

It can be seen from Figures 3.34 and 3.35 that in a drag-reduced flow, the rate of occurrence of quadrant 2 and quadrant 4 events is much lower at low thresholds than water flows at equal wall shear stress. However, at higher thresholds, the rate of occurrence of these events is about the same in drag-reduced and water flows. These results confirm Luchik and Tiederman's hypothesis that the small amplitude events are damped in drag-reduced flows while the large amplitude events are unaffected. Luchik and Tiederman (1988) noted an increase in the probability density rate of occurrence of

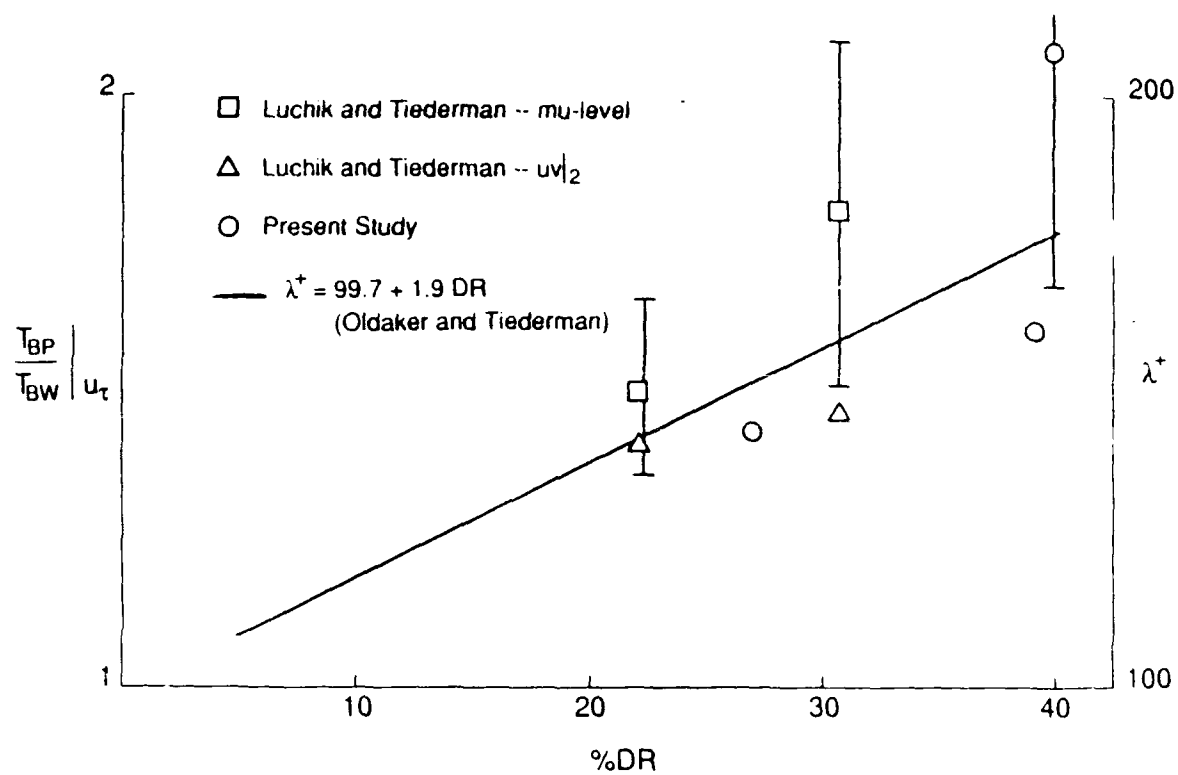


Figure 3.32. Variation in the ratio of the average burst period in a drag-reduced flow to the average burst period in a water flow at equal τ_w .

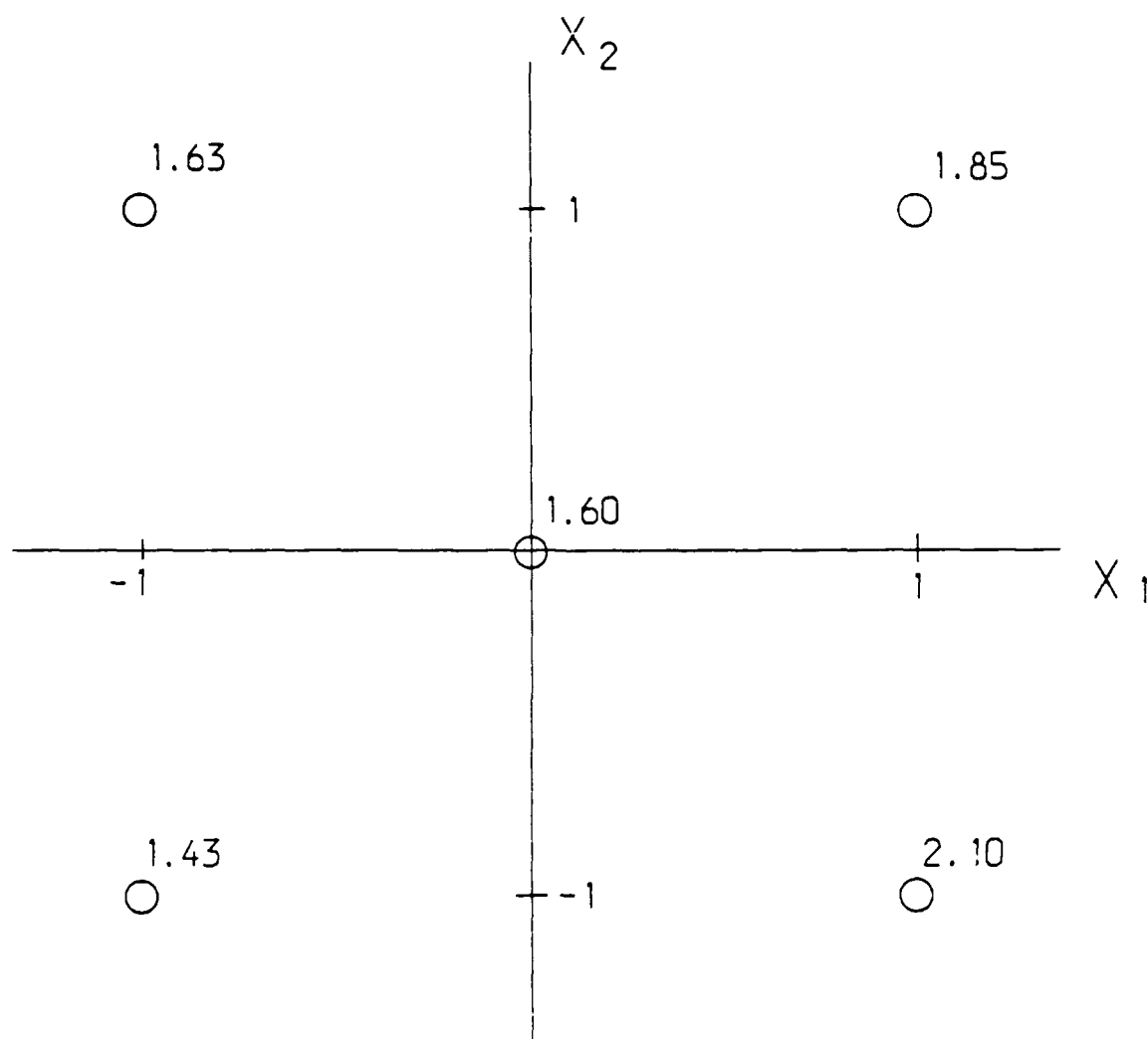


Figure 3.33. Variation in the ratio of the average burst period in a drag-reduced flow to the average burst period in a water flow at equal wall shear stress as a function of the design variables.

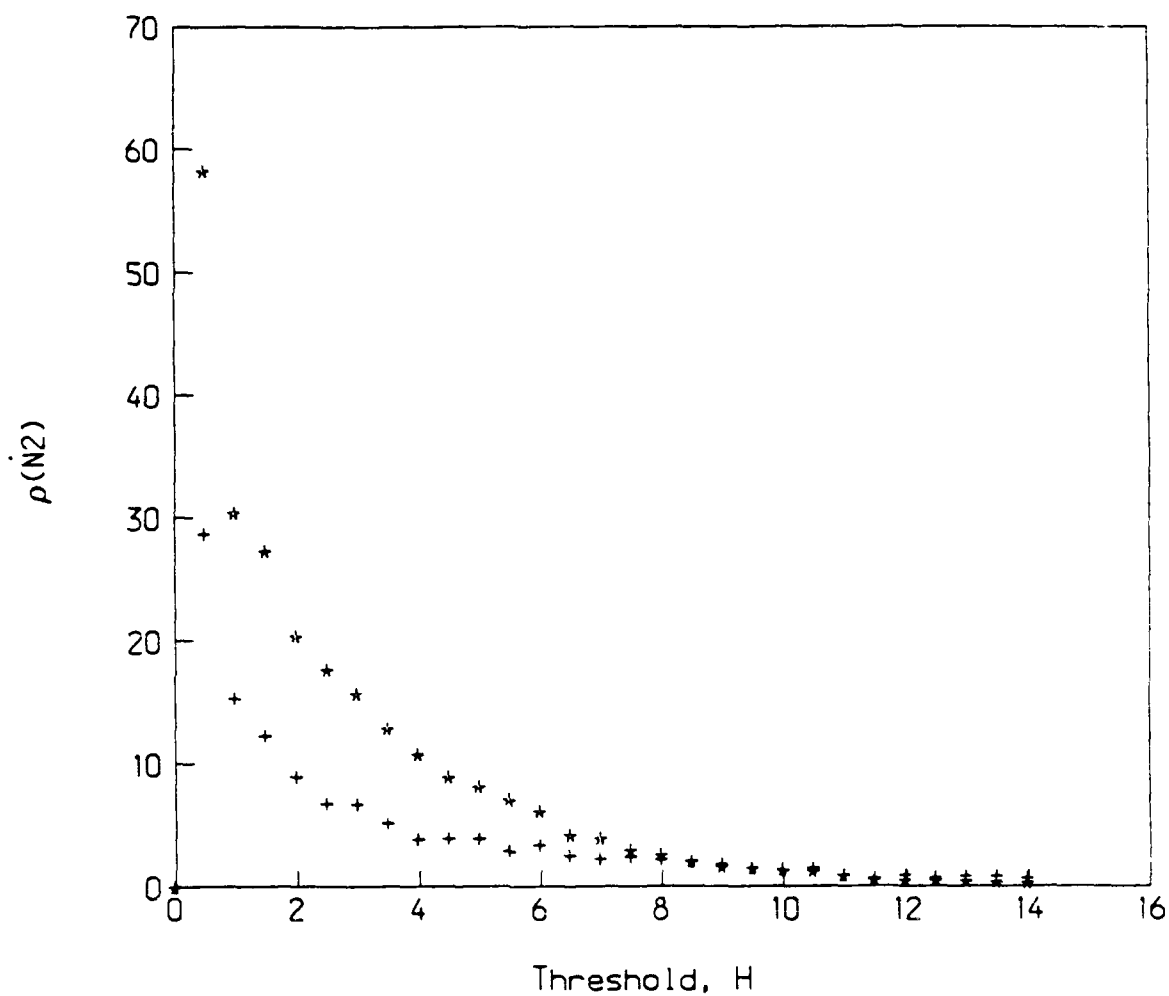


Figure 3.34. Probability density for the rate of occurrence of quadrant 2 events as a function of threshold: *, water flow, $\left. \frac{d\bar{U}}{dy} \right|_w = 2500 \text{ s}^{-1}$; +, 4 ppm drag-reduced flow at equal wall shear stress; $y^+ = 40$ for both flows.

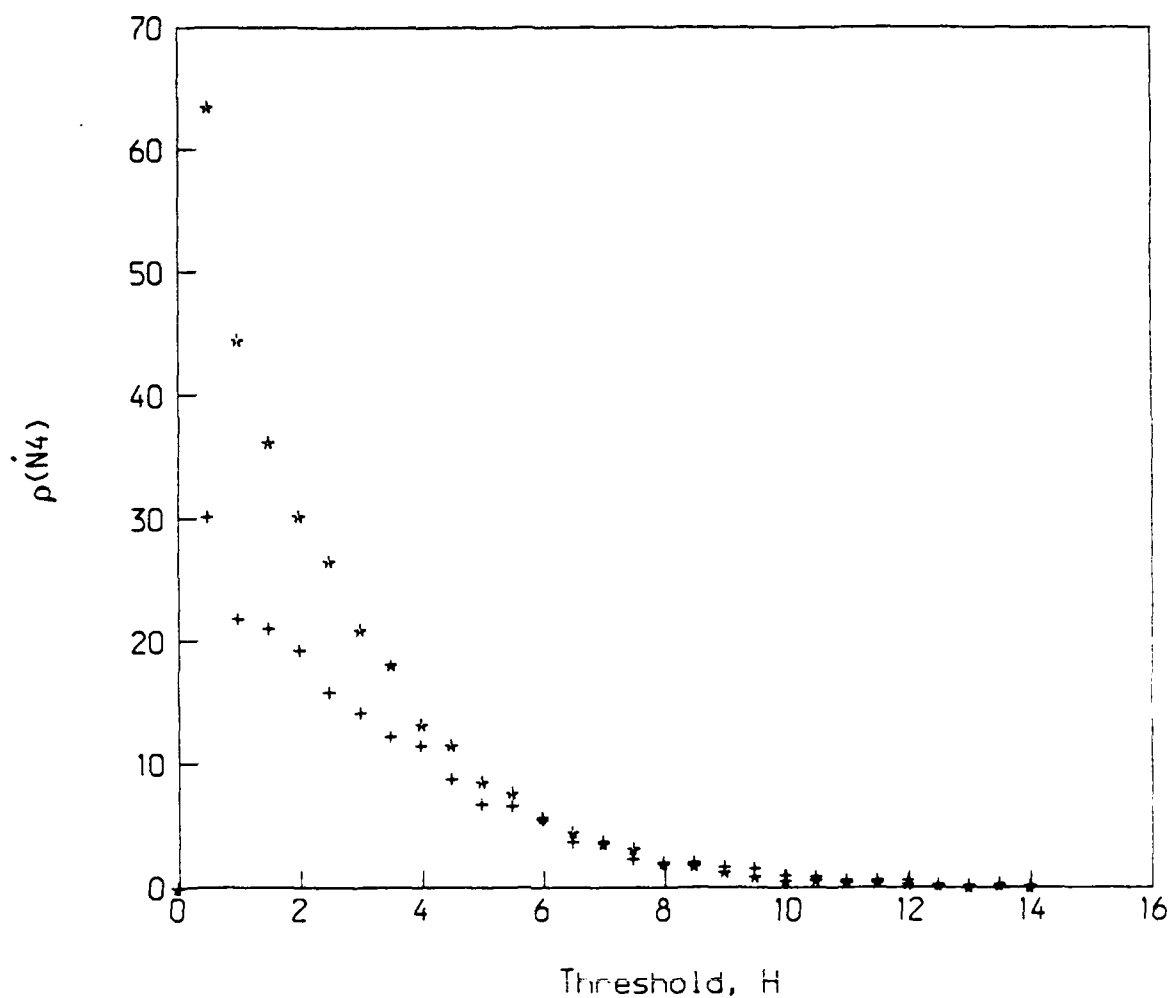


Figure 3.35. Probability density for the rate of occurrence of quadrant 4 events as a function of threshold: *, water flow, $\frac{d\bar{U}}{dy}|_w = 2500 \text{ s}^{-1}$; +, 4 ppm drag-reduced flow at equal wall shear stress; $y^+ = 40$ for both flows.

and Tiederman (1988) noted an increase in the probability density rate of occurrence of quadrant 4 events for drag-reduced flows at higher thresholds ($H > 4$). Examination of Figure 3.35 shows that no such trend was present in this flow. It should be noted that the data at wall strain rate of 2500 s^{-1} is used instead of the "typical" data at a wall strain rate of 1000 s^{-1} because no water flow data was available at that condition.

CHAPTER 4 - RECAPITULATION AND CONCLUSIONS

The dependence of drag reduction and turbulent structure upon three variables: wall strain rate ($\left. \frac{d\bar{U}}{dy} \right|_w$), average polymer concentration in the channel (\bar{C}), and channel height (h) has been investigated. A functional form of dependence of drag reduction upon the wall strain rate and the average polymer concentration based upon the 2.5 cm channel results was found. No form of dependence of drag reduction upon channel height was determined, even though it is readily apparent from the data that channel height is a factor in drag reduction.

The method to be used for scale-up (Granville 1985) required a constant slope of the logarithmic region of the velocity profile. The results of this experiment readily showed that the slope of the logarithmic region of the profile changes with the amount of drag reduction present; therefore, the scale-up technique of Granville (1985) could not be used.

Two methods were used to determine the wall shear stress. By assuming a fully developed and two-dimensional flow, a force balance shows that the wall shear stress is directly proportional to the pressure drop in the channel. This method yields an average shear stress over the entire channel perimeter. By making an additional assumption that the flow is Newtonian, it is possible to obtain the local wall shear stress in the center of

the midspan where the flow is unaffected by the corners. This was done by adding the experimentally determined viscous and Reynolds stresses. It was shown that this second method yielded a very accurate estimate of the shear stress. The average and local shear stress were significantly different for all flows. The average shear stress was consistently 10-25% higher than the local shear stress. The effect of the Reynolds number upon the ratio of these stresses was determined for a Reynolds number range of $14\,000 < Re_h < 40\,000$. It appears that the difference between the average shear stress and the local shear stress increases with Reynolds number.

For all of the polymer flows except one, the sum of the viscous and Reynolds stresses yielded the shear stress. The one flow that did not behave as a Newtonian flow (flow conditions: $\frac{d\bar{U}}{dy}|_w = 4000\text{ s}^{-1}$, $\bar{C} = 5\text{ ppm}$, and channel height = 2.5 cm) yielded results similar to those of Willmarth et al. (1987). In the outer flow the viscous and Reynolds stresses added to the total stress, $\tau_w^*(1-y/a)$. It is in the inner region, $y^+ < 100$, that the sum of the viscous and Reynolds stresses do not add up to the total stress, $\tau_w^*(1-y/a)$.

The water flow results presented here agree well with those presented in the literature. In addition, the water flow results cover a broad enough Reynolds number range so that the data may be used in the future for establishing or helping to confirm trends that are yet unknown to the author.

Due to limited pumping capacity, it was not possible to obtain all of the flow conditions necessary to complete the factorial design in the 6.0 cm channel. For this reason, the results obtained from the 6.0 cm channel could not be used for modeling

purposes.

In a drag-reduced flow, the streamwise RMS velocity increased at all locations in the channel, with the most pronounced effect around the peak, which was $\approx 20\%$ higher than that of a water flow at equal wall shear stress. The peak also moved away from the wall in a drag-reduced flow. Attempts to model the behavior of the peak as a function of the design variables yielded inconclusive results. It was then shown that the position of the peak depends solely upon drag reduction. The wall-normal RMS velocity decreased in the drag-reduced flows, which is consistent with results presented in the literature. Due to the fact that the wall-normal RMS exhibited no distinct peak, no modeling similar to that done for the streamwise RMS velocity was attempted.

Turbulent shear stress levels in the polymer flow were not significantly different in drag-reduced flows (except for the special case mentioned previously) than in water flows at equal wall shear stress. The correlation coefficient in the drag-reduced flows was significantly lower across the channel than that of the equal wall shear stress water flow.

The integrated production profiles of $\overline{u^2}$ are lower in drag-reduced flows than in water flows when normalized with mass average velocity. The water flow data showed that the normalized integrated production profile had a value of ≈ 1.3 for the Reynolds number range of this study. This constant value confirms that the mass average velocity is the correct scaling for the production integral. The drag-reduced flow data does not correlate with the Reynolds number. Instead, the value of this integral decreased with increasing drag reduction. The peak in $\overline{u^2}$ production moves away from the wall and

broadens with drag reduction. As with the streamwise RMS velocity, a dependence of the behavior of the $\overline{u^2}$ production peak upon the design variables was sought. This modeling attempt also failed to yield conclusive results. The peak behavior was shown to depend solely upon drag reduction.

As previously stated, the production of $\overline{u^2}$ is lower, the streamwise normal stress is increased and the wall-normal normal stress is decreased in a drag-reduced flow. Since an increase in destruction of the wall-normal normal stress would also result in an increase in destruction of the streamwise normal stress, one must conclude that the wall-normal normal stress production decreased. As previously seen, there is no production term from which the wall-normal normal stress extracts energy from the mean flow. The wall-normal normal stress is produced by taking energy from the streamwise normal stress by virtue of the "pressure-strain" or *redistribution term*. Therefore, the polymer must be inhibiting transfer of energy from the streamwise normal stress by some interaction with the pressure-strain correlation. These conclusions are in agreement with those presented by Walker (1988). The Reynolds shear stress was shown to have a lower production for homogeneous, well-mixed drag-reduced flows than for water flows. This finding does not agree with Walker (1988) who saw an increase in Reynolds stress production near the injector in inhomogeneous flows. Walker concluded that the pressure-strain correlation caused increased destruction in drag-reduced flows. From the present results, no such conclusion can be drawn and further experimentation is needed to verify the nature of this phenomenon.

Measurements of the turbulent burst period for water flows showed that normalization with the local shear velocity instead of the average shear velocity changed the non-dimensional burst period of water flows. Luchik and Tiederman (1987) showed that this non-dimensional burst period for water flows was $\bar{T}_B^+ = 90$ while normalization of the burst period with local shear velocity yields $\bar{T}_B^+ = 71$. When Luchik and Tiederman's (1987) results are normalized in a similar manner, the present results agree with theirs.

As with other turbulent structure quantities, a regression model for the burst period as a function of the design variables was sought. The dependent variable was the ratio of the average burst period for a drag-reduced flow to the average burst period of a water flow at equal wall shear stress. The regression analysis was inconclusive, as it was with the other turbulent structure variables. The ratio depends only on drag-reduction. The results here also support Luchik and Tiederman (1988) who showed that this variable increases with drag reduction in the same manner as the streak spacing. Results here also confirm Luchik and Tiederman's (1988) hypothesis that in a well mixed, low concentration flow, only the small amplitude eddies are damped.

Finally, it can be said that while drag reduction was shown to depend on at least the design variables proposed, all turbulent structure quantities depend on the amount of drag reduction rather than the design variables.

REFERENCES

- Bewersdorff, H.W. 1984 Effect of a centrally injected polymer thread on turbulent properties in pipe flows. In: *Drag Reduction*, R.J.H. Sellin and R.T. Moses, eds., Univ. of Bristol, B4.
- Bradshaw, P. 1978 *Topics in Applied Physics Volume 12: Turbulence..* Springer-Verlag, 25.
- Corino, E.R. and R.S. Brodkey 1969 A visual investigation of the wall region in turbulent flow. *J. Fluid Mech.* 37, 1.
- Dean, R.B. 1978 Reynolds number dependence of skin friction and other bulk flow variables in two-dimensional rectangular duct flow. *J. Fluids Engng.* 100, 215.
- Finnicum, D.S. and T.J. Hanratty 1985 Turbulent normal-velocity fluctuations close to a wall. *Phys. Fluids* 28, 1654.
- George, W.K. and J.L. Lumley 1973 The laser-Doppler velocimeter and its application to the measurement of turbulence. *J. Fluid Mech.* 10, 321.
- Granville, P.S. 1985 A method for predicting additive drag reduction from small-diameter pipe flows. *U.S. Navy report DTNSRDC/SPD-1142-01.*
- Hershey H.C., J.T. Kuo and M.L. Mcmillian 1975 Drag Reduction of straight and branched aluminum disoaps. *Ind. Eng. Chem. Product Research and Development* 14, 192.
- Hunter, J.S. 1960 Some applications of statistics to experimentation. *AIChE J.* 56, 10.
- Hussain, A.K.M.F. and W.C. Reynolds 1975 Measurements in fully developed turbulent channel flow. *J. Fluids Engng.* 97, 568.
- Instruction Manual for System 9100-6, Single Channel High Power LDV, Thermo-Systems Incorporated, St. Paul, Minnesota.
- Instruction Manual for System 9100-8 Laser Doppler Velocimeter, Thermo-Systems

Incorporated, St. Paul Minnesota.

Kim H.T., S.J. Kline and W.C. Reynolds 1971 The production of turbulence near a smooth wall in a turbulent boundary layer. *J. Fluid Mech.* **50**, 133.

Kim J., P. Moin and R. Moser 1987 Turbulence statistics in fully developed channel flow at low Reynolds number. *J. Fluid Mech.* **177**, 133.

Kreplin, H. and H. Eckelmann 1979 Behavior of the three fluctuating velocity components in the wall region of a turbulent channel flow. *Phys. Fluids* **22**, 1233.

Luchik, T.S. 1985 *The effect of drag reducing additives on turbulent structure in channel flow*. Ph.D. Thesis, Purdue University.

Luchik, T.S. and W.G. Tiederman 1987 Timescale and structure of ejections and bursts in turbulent channel flows. *J. Fluid Mech.* **174**, 529.

Luchik, T.S. and W.G. Tiederman 1988 Turbulent structure in low concentration drag-reducing channel flows. *J. Fluid Mech.* **190**, 241.

McComb, W.D. and L.H. Rabie 1982 Local drag reduction due to injection of polymer solutions into turbulent flow in a pipe. Part I: Dependence on local polymer concentration; Part II: Laser-Doppler measurements of turbulent structure. *AIChE J.* **28**, 547.

Oldaker, D.K. and W.G. Tiederman 1977 Spatial structure of the viscous sublayer in drag-reducing channel flows. *Phys. Fluids* **20**, No. 10, Part II, S133.

Reischman, M.M. and W.G. Tiederman 1975 Laser Doppler anemometer measurements in drag-reducing channel flows. *J. Fluid Mech.* **70**, 369.

Savill, A.M. and J.C. Mumford 1988 Manipulation of turbulent boundary layers by outer-layer devices: skin-friction and flow-visualization results. *J. Fluid Mech.* **194**, 389.

Spalart, P. 1988 Direct simulation of a turbulent boundary layer up to $Re_\theta = 1410$. *J. Fluid Mech.* **187**, 61.

Sreenivasan, K.R. 1988 The turbulent boundary layer. *private communication*.

Tiederman, W.G., T.S. Luchik and D.G. Bogard 1985 Wall layer structure and drag reduction. *J. Fluid Mech.* **156**, 419.

Tiederman, W.G. 1989 Eulerian detection of turbulent bursts. In: *Near Wall Turbulence*, S.J. Kline and N.H. Afgan, eds., Hemisphere New York, New York, in

press.

Virk, P.S. 1975 Drag reduction fundamentals. *AIChE J.* **21**, 625.

Walker, D.T., W.G. Tiederman and T.S. Luchik 1986 Optimization of the injection process for drag reducing additives. *Exp. in Fluids* **4**, 114.

Walker, D.T. 1988 *Turbulent structure and mass transport in a channel flow with polymer injection*. Ph.D Thesis, Purdue University.

Walsh, M.J. and L.M. Weinstein 1979 Drag and heat-transfer characteristics of small longitudinally ribbed surfaces. *AIAA Journal* **17**, 776.

Wei, T. 1987 *Reynolds number effects on the small scale structure of a turbulent channel flow*. Ph.D. Dissertation, University of Michigan.

Wells, C.S. and J. G. Spangler 1967 Injection of drag-reducing fluid into a turbulent pipe flow of a Newtonian fluid. *Phys. Fluids* **10**, 1890.

Willmarth, W.W., T. Wei, and C.O. Lee 1987 Laser anemometer measurements of Reynolds stress in a turbulent channel flow with drag reducing polymer additives. *Phys. Fluids* **30**, 935.

Wu, J. and M.P. Tulin 1972 Drag reduction by ejecting additive solutions into pure-water boundary layer. *J. Basic Engng.* **74**, 749.

APPENDIX

In this appendix, the mean and RMS streamwise and wall-normal velocities, the turbulent shear stress \overline{uv} and the location from the wall that these measurements were made are shown in tabular form. Also included in this appendix are mean velocity profiles, RMS velocity profiles, Reynolds shear stress profiles, $\overline{u^2}$ production profiles, wall shear stress calculation profiles, and correlation coefficient profiles for all flows. Water flow profiles at equal wall shear stress are shown in the same plots as the drag-reduced profiles so that differences in the flows are readily apparent.

Data for 6.0 cm channel, $\frac{d\bar{U}}{dy} \Big|_w = 1000 \text{ s}^{-1}$

\bar{V} (m/s)	\bar{U} (m/s)	v' (m/s)	u' (m/s)	\bar{uv} (m/s) ²	y (mm)
Water Flow					
3.63E-03	0.612	1.97E-02	2.45E-02	-9.79E-06	30.000
2.19E-03	0.606	2.16E-02	2.94E-02	-1.84E-04	21.981
1.34E-03	0.579	2.39E-02	3.68E-02	-3.19E-04	16.106
1.26E-03	0.555	2.62E-02	4.20E-02	-4.31E-04	11.801
1.14E-03	0.532	2.83E-02	4.66E-02	-5.41E-04	8.646
1.31E-03	0.508	2.94E-02	4.96E-02	-5.84E-04	6.335
1.62E-03	0.484	3.01E-02	5.18E-02	-6.35E-04	4.642
4.07E-05	0.462	3.09E-02	5.30E-02	-6.43E-04	3.401
3.93E-04	0.444	3.01E-02	5.55E-02	-6.39E-04	2.492
-5.39E-04	0.423	2.98E-02	5.97E-02	-6.49E-04	1.826
-1.41E-04	0.401	2.79E-02	6.43E-02	-6.23E-04	1.338
-3.40E-04	0.373	2.56E-02	6.93E-02	-5.86E-04	0.980
-7.13E-04	0.343	2.30E-02	7.49E-02	-5.54E-04	0.718
-2.51E-04	0.297	1.96E-02	7.58E-02	-4.30E-04	0.526
-2.05E-04	0.250	1.67E-02	7.38E-02	-3.44E-04	0.386
5.49E-04	0.200	1.49E-02	6.65E-02	-2.24E-04	0.283
1.33E-03	0.151	1.33E-02	5.54E-02	-1.32E-04	0.207
4.17E-03	0.105	1.31E-02	4.28E-02	-8.69E-05	0.152

3 ppm Polymer Flow

-6.33E-03	0.654	2.32E-02	2.86E-02	-3.85E-06	30.000
-8.55E-03	0.641	2.49E-02	3.19E-02	-5.03E-04	20.007
-4.75E-04	0.597	2.78E-02	4.25E-02	-4.89E-04	13.243
1.33E-04	0.560	3.11E-02	4.75E-02	-6.34E-04	8.898
-4.18E-04	0.542	3.16E-02	5.15E-02	-6.63E-04	5.934
1.02E-03	0.509	3.10E-02	5.44E-02	-6.62E-04	3.957
-1.63E-04	0.480	3.13E-02	5.76E-02	-6.52E-04	2.639
-5.11E-04	0.450	2.99E-02	6.26E-02	-6.07E-04	1.760
5.23E-04	0.421	2.56E-02	7.41E-02	-6.66E-04	1.174
-5.14E-04	0.377	2.30E-02	7.99E-02	-5.39E-04	0.783
1.59E-04	0.324	1.93E-02	8.16E-02	-4.34E-04	0.523
5.19E-04	0.253	1.66E-02	7.73E-02	-3.07E-04	0.348
1.79E-03	0.193	1.48E-02	6.70E-02	-2.11E-04	0.232
3.00E-03	0.139	1.30E-02	5.38E-02	-1.29E-04	0.155

\bar{V} (m/s)	\bar{U} (m/s)	v' (m/s)	u' (m/s)	\bar{uv} (m/s) ²	y (mm)
--------------------	--------------------	---------------	---------------	----------------------------------	-------------

5 ppm Polymer Flow

-4.23E-06	0.670	2.22E-02	2.68E-02	-8.76E-06	30.000
6.55E-04	0.622	2.56E-02	3.95E-02	-3.51E-04	13.243
2.91E-03	0.584	2.88E-02	4.59E-02	-5.42E-04	8.898
1.94E-03	0.548	3.01E-02	5.19E-02	-6.76E-04	5.934
1.66E-03	0.518	3.11E-02	5.46E-02	-6.87E-04	3.957
1.15E-03	0.496	3.02E-02	5.97E-02	-7.32E-04	2.659
7.48E-04	0.466	2.90E-02	6.53E-02	-7.19E-04	1.760
-8.17E-05	0.438	2.56E-02	7.51E-02	-7.23E-04	1.174
1.79E-05	0.386	2.12E-02	8.12E-02	-5.52E-04	0.783
3.15E-04	0.327	1.68E-02	8.40E-02	-4.40E-04	0.523

Data for 2.5 cm channel, $\left. \frac{d\bar{U}}{dy} \right|_w = 1000 \text{ s}^{-1}$

Water Flow

1.13E-02	0.598	2.03E-02	2.54E-02	4.19E-05	12.500
1.13E-03	0.585	2.21E-02	3.10E-02	-1.77E-04	9.441
1.08E-03	0.563	2.48E-02	3.77E-02	-3.36E-04	7.131
1.22E-03	0.538	2.68E-02	4.26E-02	-4.41E-04	5.386
-8.36E-04	0.514	2.80E-02	4.59E-02	-5.47E-04	4.068
-8.73E-04	0.490	2.98E-02	4.84E-02	-6.16E-04	3.072
-7.76E-04	0.469	2.94E-02	5.27E-02	-6.48E-04	2.321
-1.53E-03	0.451	2.93E-02	5.59E-02	-6.36E-04	1.753
-1.22E-03	0.427	2.87E-02	6.15E-02	-7.01E-04	1.324
-1.92E-03	0.407	2.58E-02	6.79E-02	-6.61E-04	0.999
-1.25E-03	0.377	2.25E-02	7.35E-02	-6.19E-04	0.755
-1.83E-03	0.345	1.92E-02	7.72E-02	-5.37E-04	0.570
-1.45E-03	0.298	1.62E-02	7.86E-02	-4.50E-04	0.431
-1.17E-03	0.253	1.44E-02	7.47E-02	-3.29E-04	0.325
-1.34E-03	0.205	1.27E-02	6.72E-02	-2.34E-04	0.246
-4.37E-04	0.156	1.16E-02	5.65E-02	-1.31E-04	0.186

\bar{V} (m/s)	\bar{U} (m/s)	v' (m/s)	u' (m/s)	\bar{uv} (m/s) ²	y (mm)
--------------------	--------------------	---------------	---------------	----------------------------------	-------------

3 ppm Polymer Flow

-1.10E-02	0.730	2.35E-02	3.08E-02	8.48E-05	12.500
-1.82E-03	0.723	2.21E-02	3.36E-02	-1.09E-04	9.441
-2.17E-03	0.701	2.34E-02	4.08E-02	-2.51E-04	7.131
-4.03E-03	0.678	2.49E-02	4.75E-02	-3.45E-04	5.386
-3.35E-03	0.652	2.54E-02	5.39E-02	-4.11E-04	4.068
-1.56E-03	0.630	2.48E-02	6.15E-02	-4.69E-04	3.072
-1.06E-03	0.599	2.47E-02	7.09E-02	-5.10E-04	2.321
-4.07E-03	0.571	2.27E-02	8.02E-02	-5.16E-04	1.753
-3.37E-03	0.534	2.16E-02	8.79E-02	-5.42E-04	1.324
-4.64E-03	0.478	2.02E-02	9.43E-02	-5.14E-04	0.999
-2.76E-03	0.429	1.84E-02	9.19E-02	-4.05E-04	0.755
-8.10E-04	0.369	1.70E-02	8.95E-02	-2.90E-04	0.570
9.06E-04	0.308	1.84E-02	8.35E-02	-2.37E-04	0.431
2.78E-03	0.246	1.78E-02	7.37E-02	-1.69E-04	0.325

5 ppm Polymer Flow

-4.50E-03	0.761	2.58E-02	3.15E-02	9.30E-05	12.500
-7.05E-03	0.750	2.53E-02	3.52E-02	-1.40E-04	9.441
-5.49E-03	0.730	2.54E-02	4.18E-02	-3.11E-04	7.131
-4.12E-03	0.703	2.73E-02	5.05E-02	-4.65E-04	5.386
-4.90E-03	0.676	2.76E-02	5.84E-02	-5.33E-04	4.068
-5.17E-03	0.654	2.68E-02	6.64E-02	-5.28E-04	3.072
-6.18E-02	0.612	2.92E-02	7.24E-02	-5.24E-04	2.321
3.09E-03	0.583	2.74E-02	8.22E-02	-5.23E-04	1.753
-2.02E-03	0.539	2.64E-02	9.11E-02	-5.04E-04	1.324
-3.99E-03	0.497	2.56E-02	9.75E-02	-4.50E-04	0.999
-5.23E-03	0.443	2.38E-02	9.88E-02	-3.54E-04	0.755
-3.69E-02	0.379	2.16E-02	9.30E-02	-2.93E-04	0.570
-2.40E-03	0.310	2.17E-02	8.42E-02	-1.69E-04	0.431
-1.39E-03	0.253	1.83E-02	7.24E-02	-2.25E-04	0.325
1.05E-03	0.198	2.10E-02	6.19E-02	-1.14E-04	0.246

Data for 2.5 cm channel, $\frac{d\bar{U}}{dy} \Big|_w = 2500 \text{ s}^{-1}$

\bar{V} (m/s)	\bar{U} (m/s)	v' (m/s)	u' (m/s)	\overline{uv} (m/s) ²	y (mm)
Water Flow					
-3.22E-03	0.887	3.06E-02	3.64E-02	-2.19E-05	12.500
-2.99E-03	0.866	3.36E-02	4.60E-02	-4.79E-04	9.270
7.37E-04	0.830	3.70E-02	5.69E-02	-8.24E-04	6.862
1.77E-03	0.791	3.95E-02	6.27E-02	-1.04E-03	5.079
3.33E-03	0.753	4.23E-02	6.68E-02	-1.19E-03	3.760
-2.69E-03	0.722	4.56E-02	7.11E-02	-1.40E-03	2.783
-1.64E-03	0.686	4.53E-02	7.63E-02	-1.51E-03	2.060
-5.26E-03	0.658	4.55E-02	8.08E-02	-1.54E-03	1.524
-5.21E-03	0.631	4.42E-02	8.60E-02	-1.56E-03	1.129
-5.29E-03	0.601	4.17E-02	9.28E-02	-1.50E-03	0.835
-4.43E-03	0.568	3.74E-02	0.103	-1.45E-03	0.618
-4.26E-03	0.522	3.13E-02	0.110	-1.34E-03	0.458
-4.29E-03	0.457	2.63E-02	0.114	-1.16E-03	0.339
-3.94E-03	0.393	2.18E-02	0.110	-8.51E-04	0.251
-2.93E-03	0.315	1.81E-02	0.101	-6.43E-04	0.186
-2.03E-03	0.234	1.50E-02	8.41E-02	-3.72E-04	0.137
4 ppm Polymer Flow					
-2.77E-03	1.345	3.93E-02	4.80E-02	2.68E-05	12.500
-2.04E-03	1.328	4.09E-02	5.82E-02	-4.45E-04	9.270
-2.93E-03	1.283	4.21E-02	7.12E-02	-9.21E-04	6.862
-1.42E-03	1.239	4.40E-02	8.17E-02	-1.21E-03	5.079
-3.77E-03	1.192	4.50E-02	9.27E-02	-1.26E-03	3.760
-1.65E-03	1.147	4.63E-02	0.106	-1.54E-03	2.783
1.18E-02	1.095	4.66E-02	0.121	-1.58E-03	2.060
0.0	1.043	4.53E-02	0.130	-1.51E-03	1.524
-1.12E-02	0.969	4.30E-02	0.143	-1.46E-03	1.129
-3.62E-03	0.908	3.78E-02	0.158	-1.39E-03	0.835
-3.26E-03	0.826	3.42E-02	0.167	-1.64E-03	0.618
-1.84E-03	0.731	3.10E-02	0.161	-1.15E-03	0.458
-1.74E-03	0.591	2.91E-02	0.149	-8.74E-04	0.339
-1.31E-03	0.539	2.92E-02	0.143	-7.46E-04	0.251
-2.29E-03	0.461	2.61E-02	0.131	-5.71E-04	0.186

Data for 2.5 cm channel, $\frac{d\bar{U}}{dy} \Big|_w = 4000 \text{ s}^{-1}$

\bar{V} (m/s)	\bar{U} (m/s)	v' (m/s)	u' (m/s)	\bar{uv} (m/s) ²	y (mm)
Water Flow					
2.18E-03	1.326	4.68E-02	5.52E-02	1.50E-04	12.500
-1.37E-03	1.298	4.64E-02	6.60E-02	-6.13E-04	9.190
-3.09E-03	1.241	5.25E-02	8.06E-02	-1.42E-03	6.757
-2.49E-03	1.182	5.84E-02	9.21E-02	-2.02E-03	4.968
1.08E-03	1.123	6.19E-02	0.101	-2.42E-03	3.653
1.66E-03	1.075	6.32E-02	0.105	-2.46E-03	2.685
2.86E-03	1.024	6.47E-02	0.111	-2.77E-03	1.974
1.74E-03	0.978	6.65E-02	0.114	-2.85E-03	1.452
4.14E-03	0.934	6.58E-02	0.118	-2.80E-03	1.067
3.75E-03	0.890	6.53E-02	0.124	-2.89E-03	0.785
2.14E-03	0.846	6.26E-02	0.133	-2.69E-03	0.577
6.65E-03	0.798		0.141		0.424
6.30E-03	0.713		0.153		0.312
1.06E-02	0.645		0.158		0.229
1.34E-02	0.576		0.156		0.169
1.38E-02	0.508		0.156		0.124

3 ppm Polymer Flow

8.88E-04	1.697	4.29E-02	5.48E-02	-1.17E-04	12.500
-3.87E-03	1.663	4.60E-02	6.75E-02	-9.28E-04	9.190
2.93E-04	1.598	5.10E-02	8.24E-02	-1.54E-03	6.757
-5.86E-04	1.540	5.43E-02	9.85E-02	-2.17E-03	4.968
-2.28E-03	1.497	5.36E-02	0.115	-2.33E-03	3.653
-2.25E-03	1.434	5.50E-02	0.129	-2.70E-03	2.685
-7.85E-03	1.367	5.63E-02	0.140	-2.79E-03	1.974
-9.15E-03	1.306	5.29E-02	0.153	-2.65E-03	1.452
-8.03E-03	1.224	5.08E-02	0.171	-2.65E-03	1.067
-1.08E-02	1.145	4.95E-02	0.188	-2.83E-03	0.785
-8.62E-03	1.059	4.35E-02	0.196	-2.42E-03	0.577
-8.07E-03	0.956	4.12E-02	0.200	-2.18E-03	0.424
-6.39E-03	0.799	3.69E-02	0.194	-1.63E-03	0.312
-5.34E-03	0.637	3.17E-02	0.173	-1.24E-03	0.229
-3.41E-03	0.462	2.57E-02	0.140	-5.69E-04	0.169
-2.08E-03	0.340	2.58E-02	0.116	-5.15E-04	0.124

\bar{V} (m/s)	\bar{U} (m/s)	v' (m/s)	u' (m/s)	\bar{uv} (m/s) ²	y (mm)
5 ppm Polymer Flow					
6.50E-03	1.818	4.46E-02	5.76E-02	-1.97E-04	12.500
6.35E-03	1.746	4.78E-02	7.24E-02	-9.26E-04	9.190
-1.29E-03	1.732	5.01E-02	8.67E-02	-1.32E-03	7.880
-9.34E-03	1.696	5.16E-02	8.68E-02	-1.52E-03	6.757
-3.86E-03	1.662	5.12E-02	9.32E-02	-1.62E-03	5.794
4.18E-04	1.636	5.19E-02	9.93E-02	-1.73E-03	4.968
1.56E-03	1.610	5.09E-02	0.108	-1.81E-03	4.260
4.68E-03	1.562	5.43E-02	0.118	-2.21E-03	3.653
6.90E-03	1.505	5.34E-02	0.131	-2.07E-03	2.685
9.12E-03	1.452	5.03E-02	0.153	-2.16E-03	1.974
9.15E-03	1.380	4.84E-02	0.166	-2.07E-03	1.452
1.21E-02	1.286	4.29E-02	0.190	-1.61E-03	1.067
1.78E-02	1.199	4.47E-02	0.201	-1.54E-03	0.785
1.55E-02	1.079	4.21E-02	0.212	-1.12E-03	0.577
1.79E-02	0.982	4.27E-02	0.209	-7.48E-04	0.424
2.03E-02	0.849	4.23E-02	0.195	-3.24E-04	0.312
2.42E-02	0.720	4.48E-02	0.180	-7.42E-05	0.229

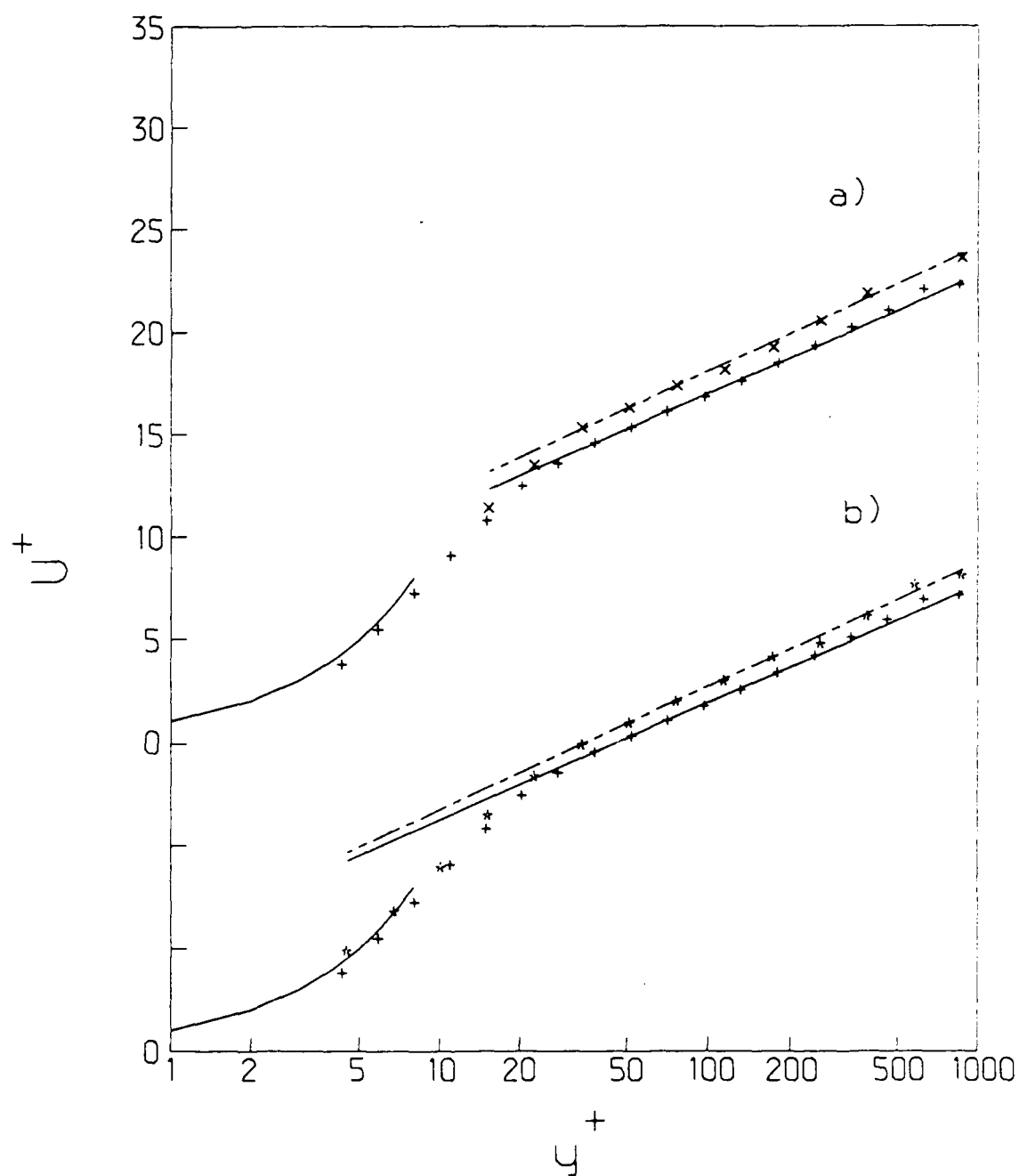


Figure A.1. Mean velocity profiles for 6.0 cm channel, $\frac{d\bar{U}}{dy} \Big|_w = 1000 \text{ s}^{-1}$: a) 5 ppm polymer flow; b) 3 ppm polymer flow; +, water flow at equal τ_w .

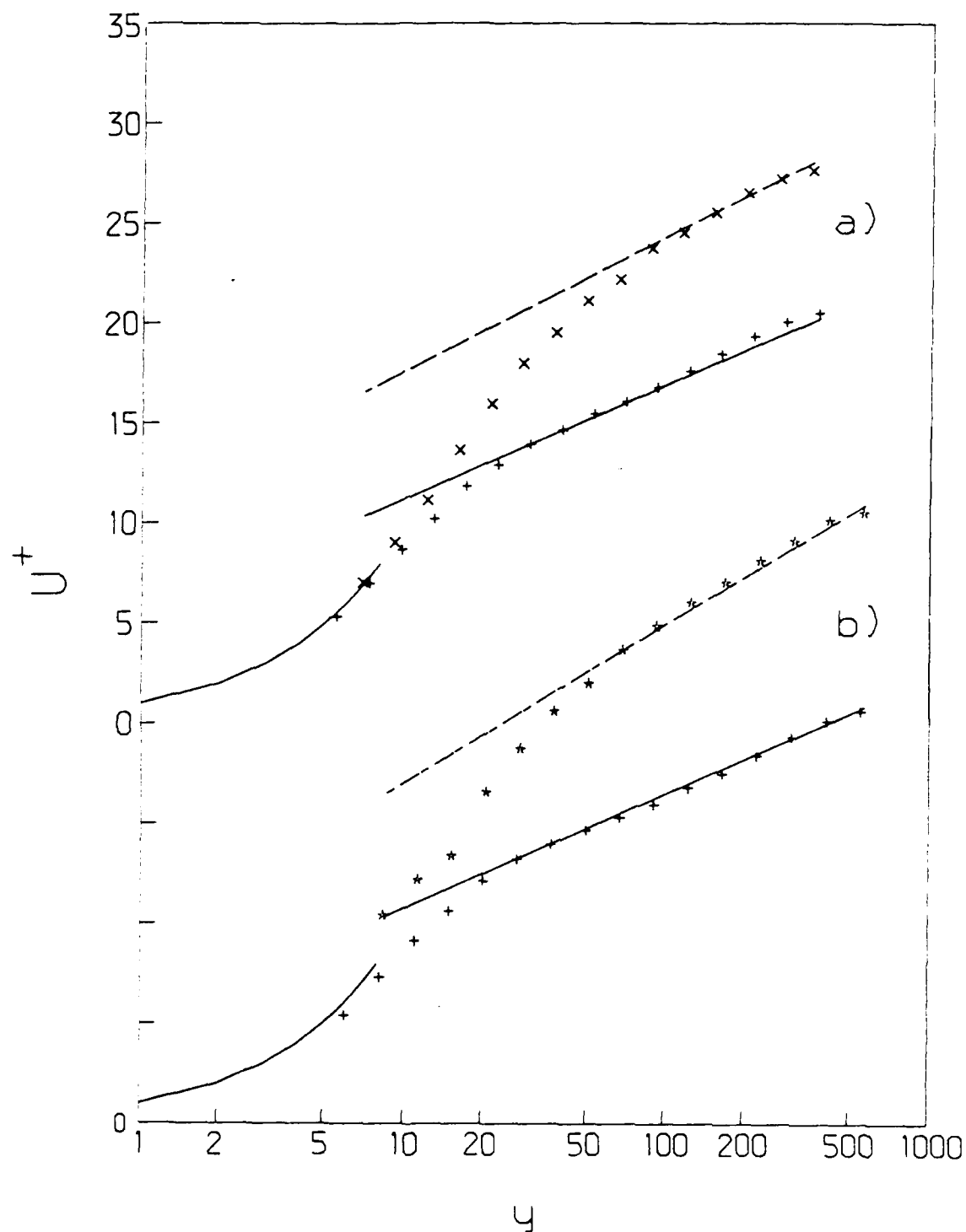


Figure A.2. Mean velocity profiles for 2.5 cm channel: a) $\frac{d\bar{U}}{dy} \Big|_w = 1000 \text{ s}^{-1}$, 5 ppm polymer flow; b) $\frac{d\bar{U}}{dy} \Big|_w = 2500 \text{ s}^{-1}$, 4 ppm polymer flow; +, water flow at equal τ_w .

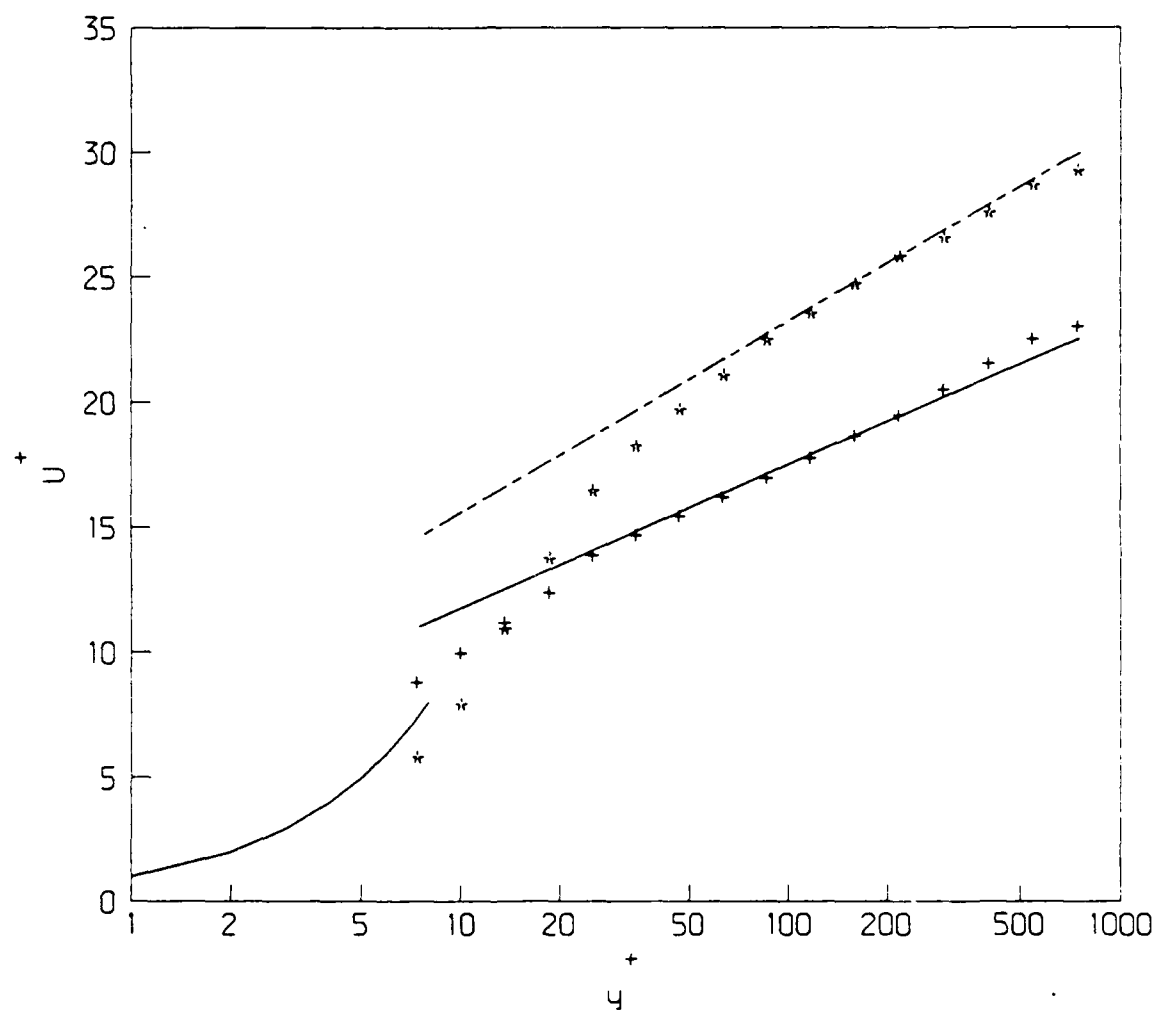


Figure A.3. Mean velocity profiles for 2.5 cm channel: $\frac{d\bar{U}}{dy} \Big|_w = 4000 \text{ s}^{-1}$, 3 ppm polymer flow; +, water flow at equal τ_w .

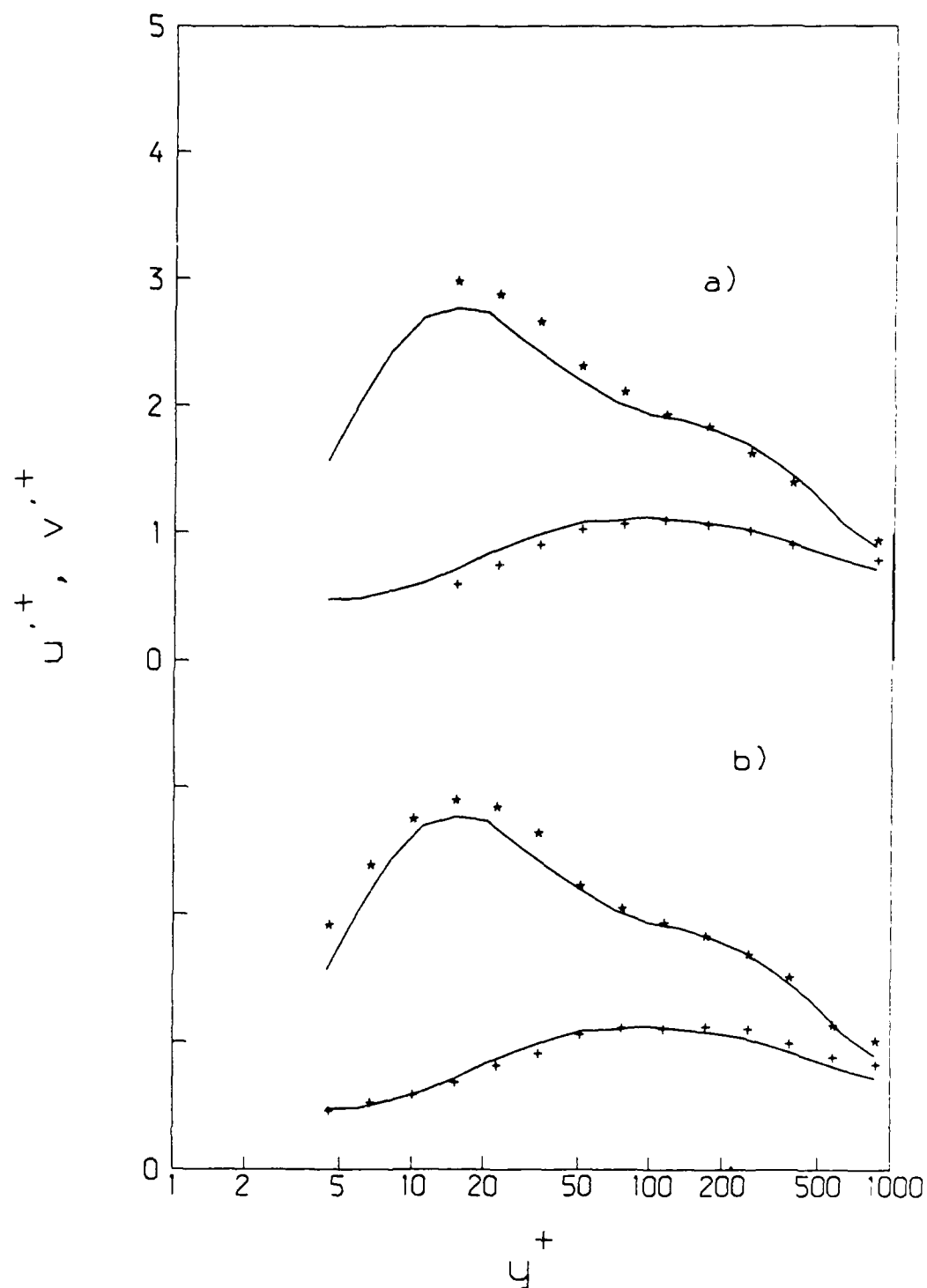


Figure A.4. RMS velocity profiles for 6.0 cm channel, $\left. \frac{d\bar{U}}{dy} \right|_w = 1000 \text{ s}^{-1}$: a) 5 ppm polymer flow; b) 3 ppm polymer flow; —, water flow at equal τ_w .

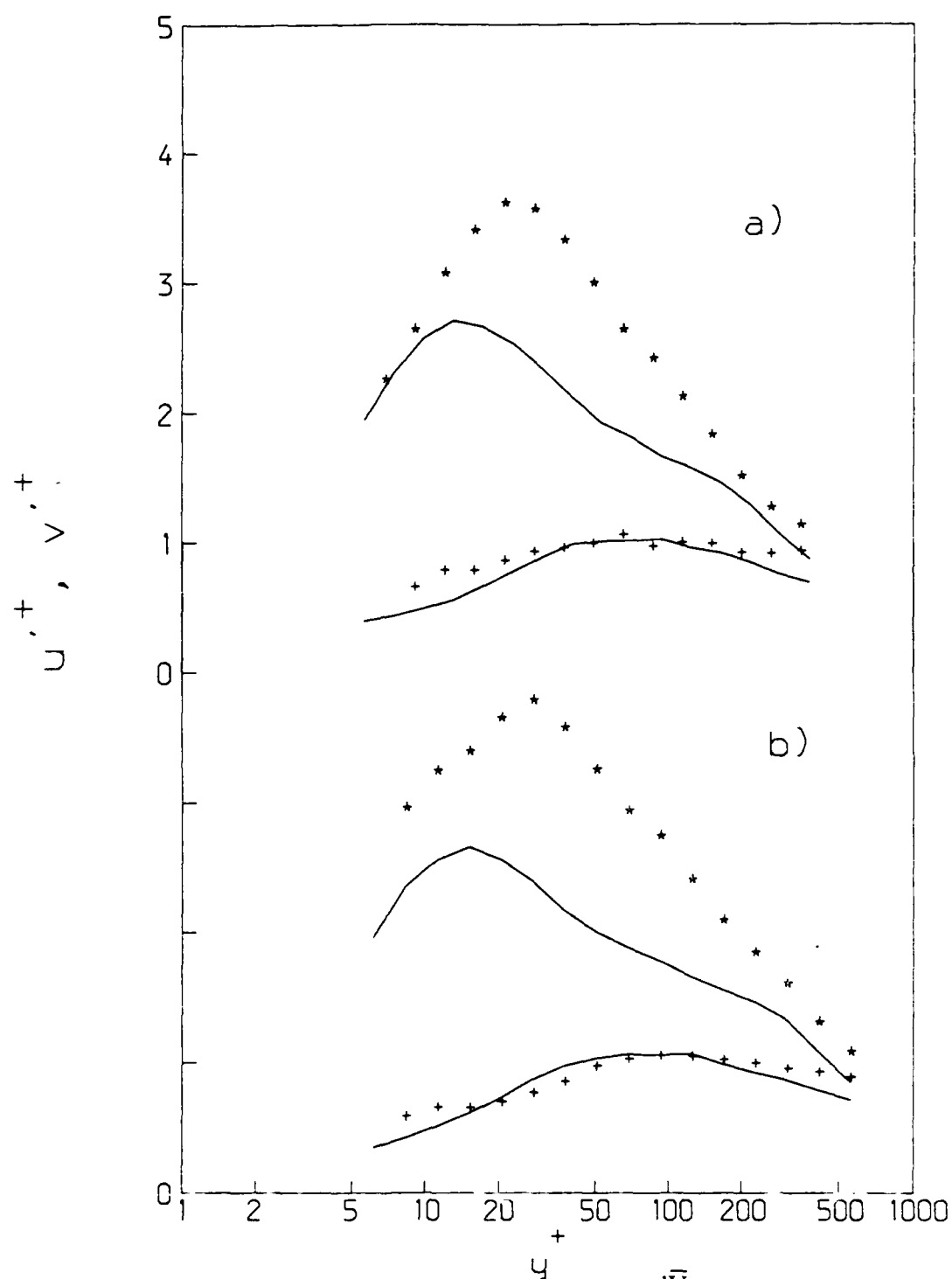


Figure A.5. RMS velocity profiles for 2.5 cm channel: a) $\frac{d\bar{U}}{dy} \Big|_w = 1000 \text{ s}^{-1}$, 5

ppm polymer flow; b) $\frac{d\bar{U}}{dy} \Big|_w = 2500 \text{ s}^{-1}$, 4 ppm polymer flow;

—, water flow at equal τ_w .

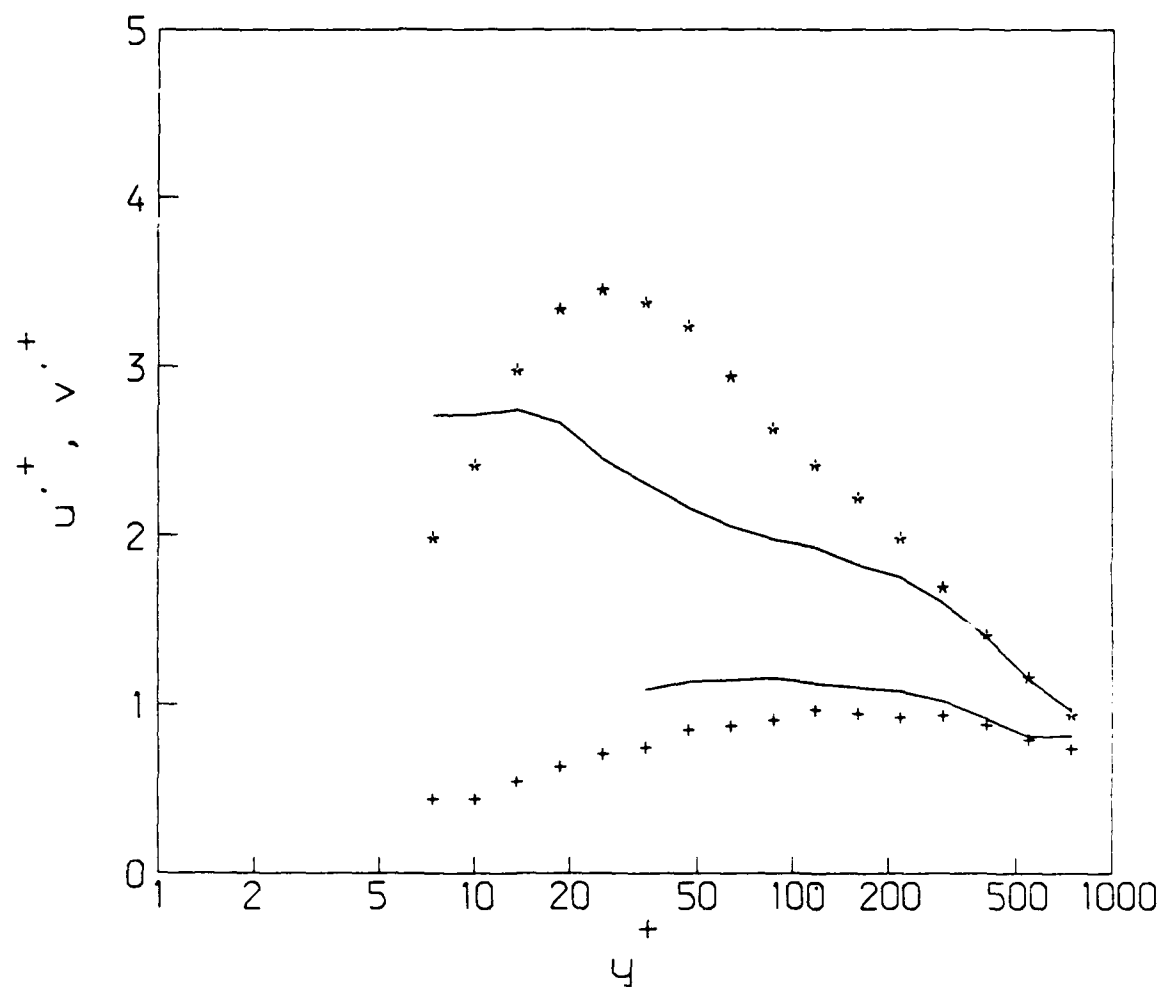


Figure A.6. RMS velocity profiles for 2.5 cm channel: $\frac{d\bar{U}}{dy} = 4000 \text{ s}^{-1}$, 3 ppm polymer flow; —, water flow at equal τ_w .

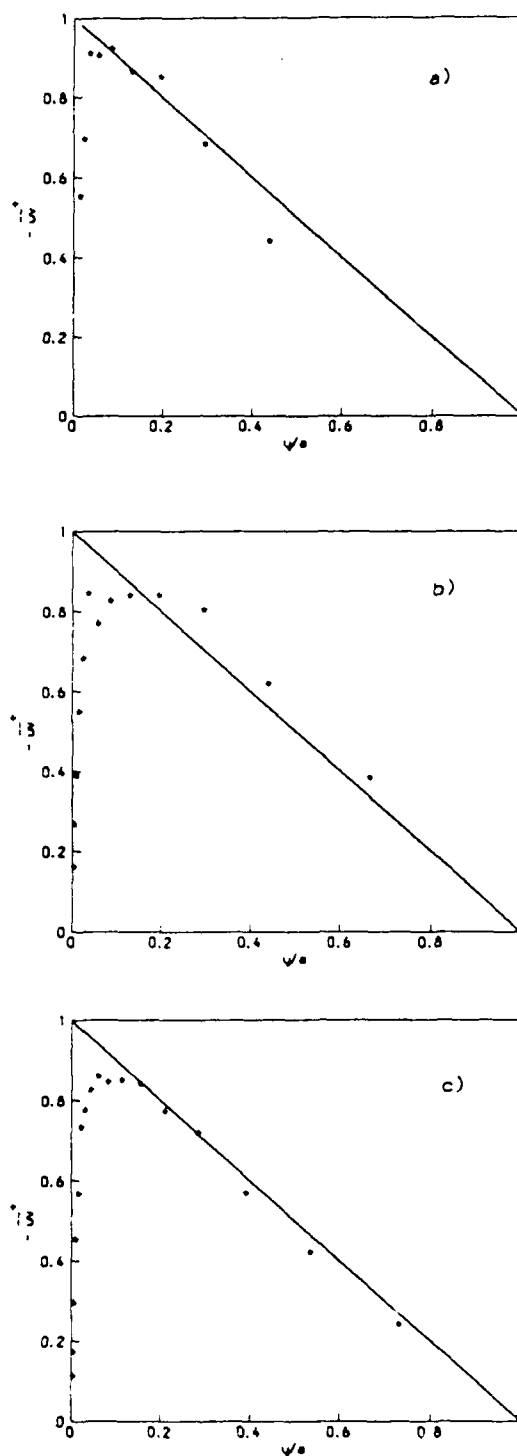


Figure A.7. Reynolds shear stress profiles for 6.0 cm channel, $\frac{d\bar{U}}{dy}|_w = 1000 \text{ s}^{-1}$:
 a) 5 ppm polymer flow; b) 3 ppm polymer flow; c) water flow.

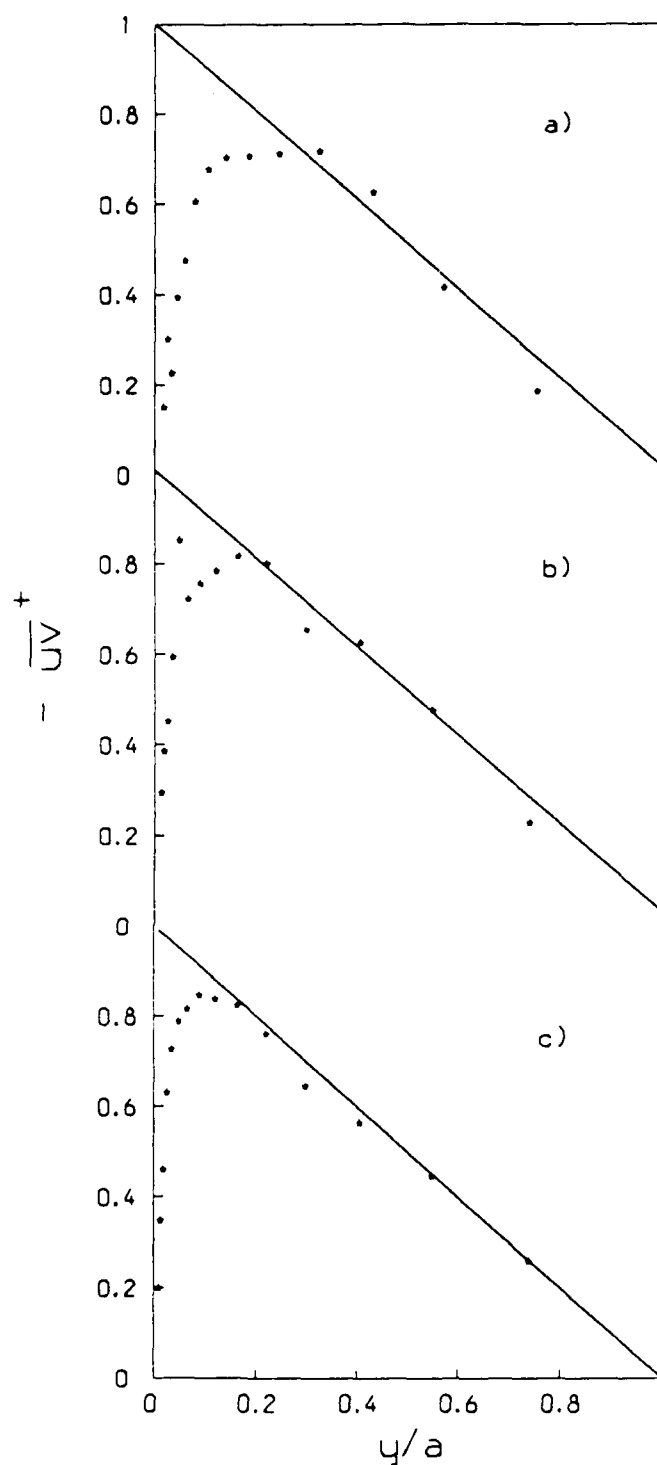


Figure A.8. Reynolds shear stress profiles for 2.5 cm channel: a) $\frac{d\bar{U}}{dy}|_w = 1000 \text{ s}^{-1}$, 5 ppm polymer flow; b,c) $\frac{d\bar{U}}{dy}|_w = 2500 \text{ s}^{-1}$; 4 ppm polymer flow, water flow, respectively.

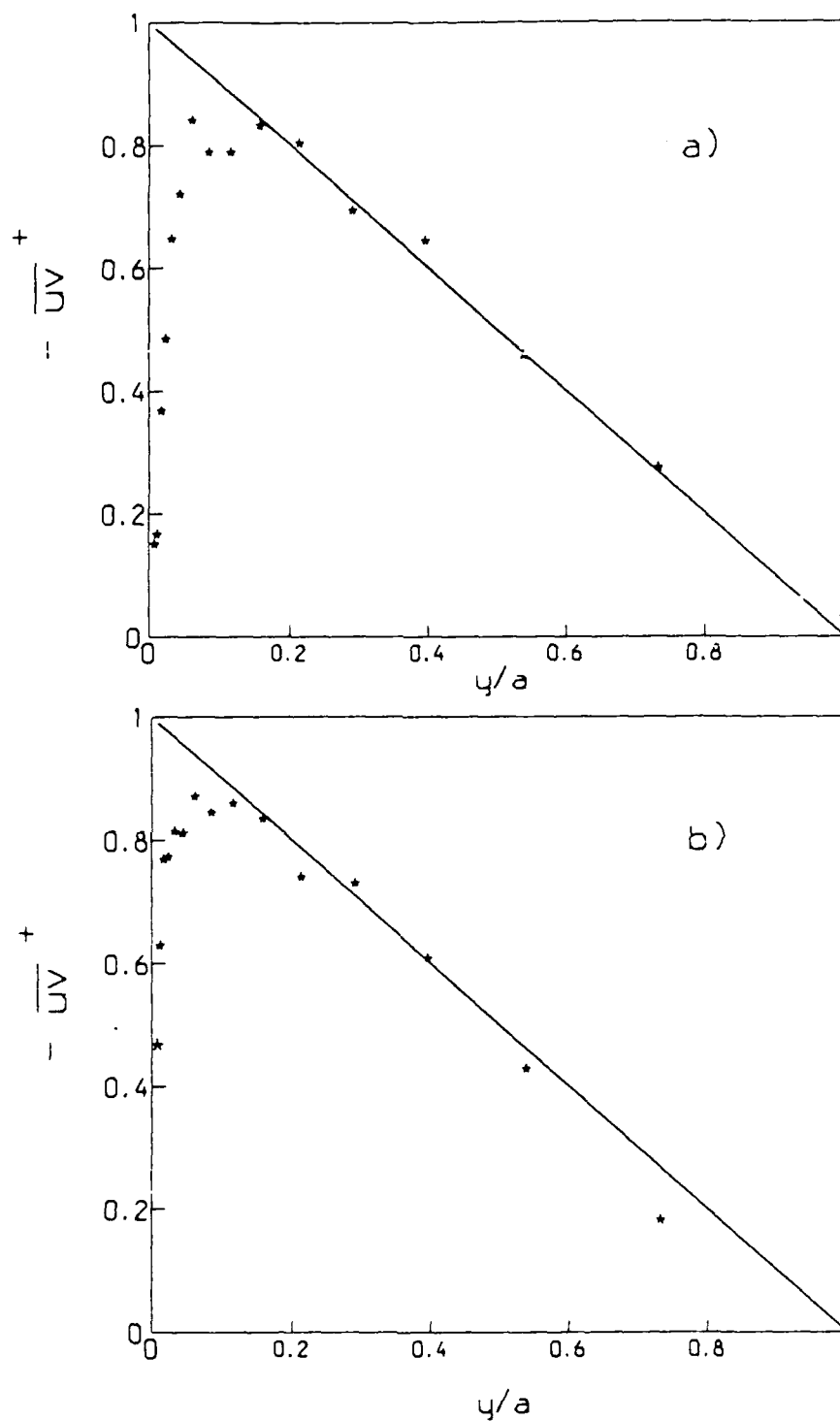


Figure A.9. Reynolds shear stress profiles for 2.5 cm channel, $\frac{d\bar{U}}{dy}\big|_w = 4000 \text{ s}^{-1}$:
 a) 3 ppm polymer flow; b) water flow.

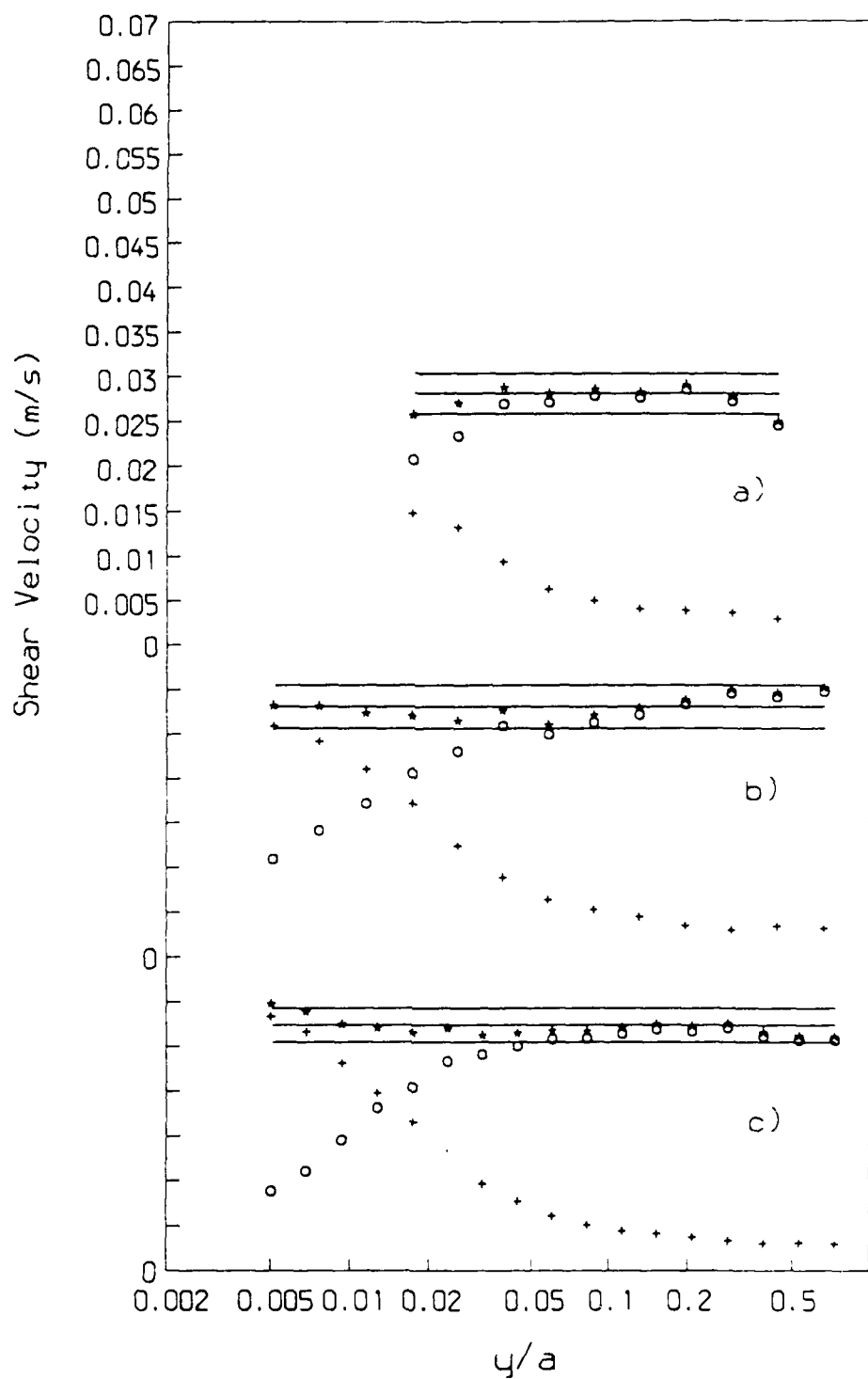


Figure A.10. Shear velocity profiles for 6.0 cm channel, $\left. \frac{d\bar{U}}{dy} \right|_w = 1000 \text{ s}^{-1}$: a) 5 ppm polymer flow; b) 3 ppm polymer flow; c) water flow.

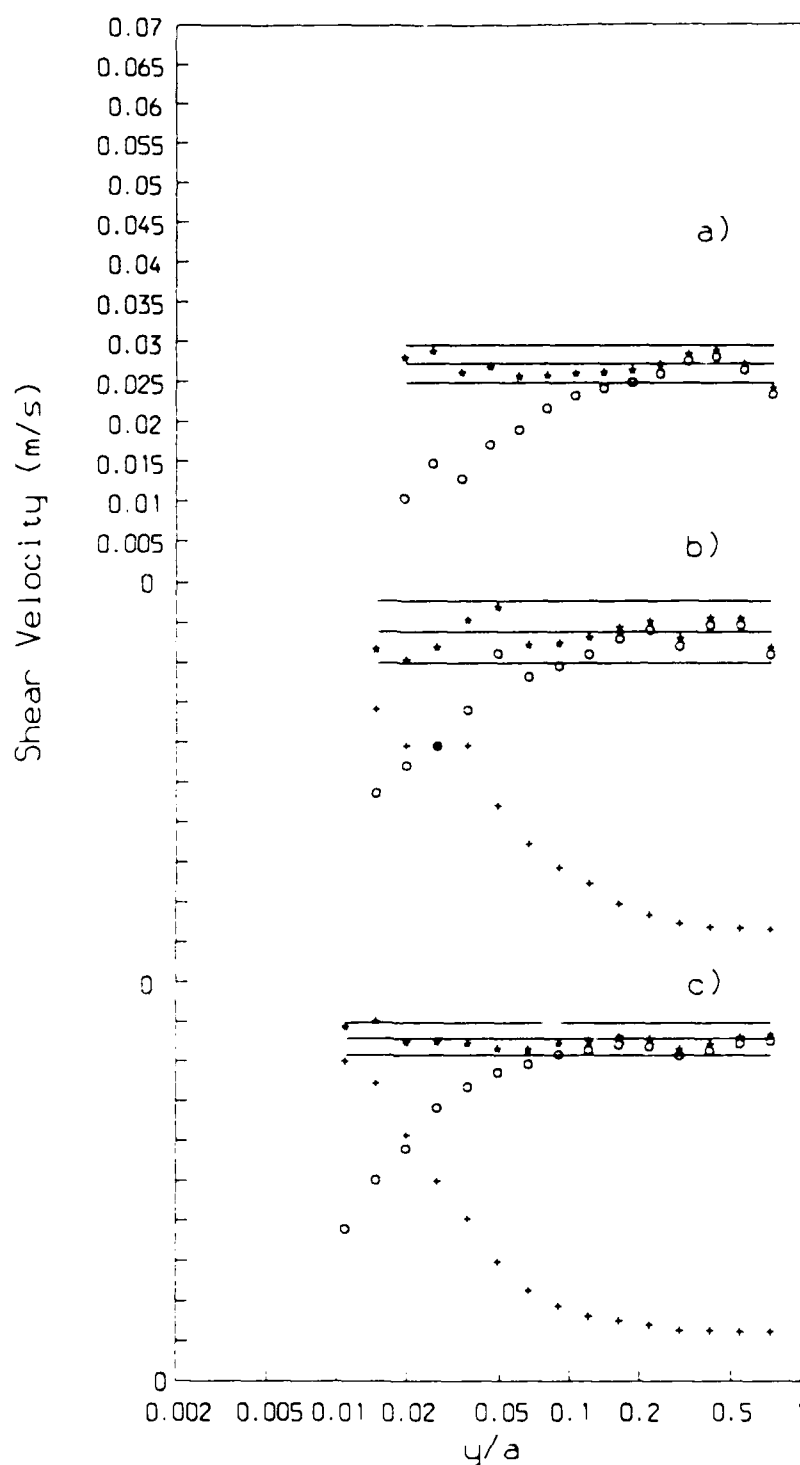


Figure A.11. Shear velocity profiles for 2.5 cm channel: a) $\frac{d\bar{U}}{dy} \Big|_w = 1000 \text{ s}^{-1}$, 5 ppm polymer flow; b,c) $\frac{d\bar{U}}{dy} \Big|_w = 2500 \text{ s}^{-1}$; 4 ppm polymer flow, water flow, respectively.

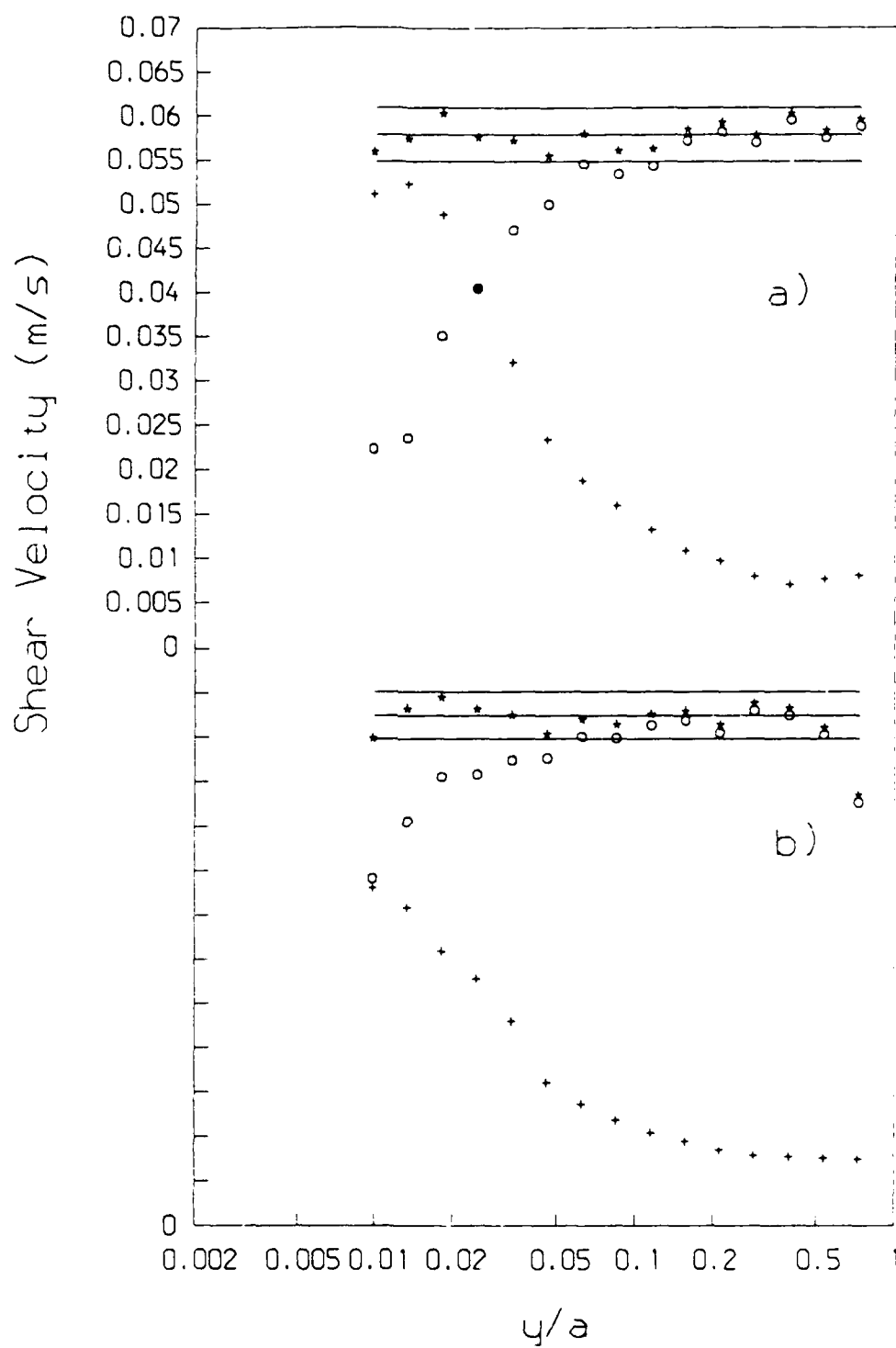


Figure A.12. Shear velocity profiles for 2.5 cm channel, $\left. \frac{d\bar{U}}{dy} \right|_w = 4000 \text{ s}^{-1}$: a) 3 ppm polymer flow; b) water flow.

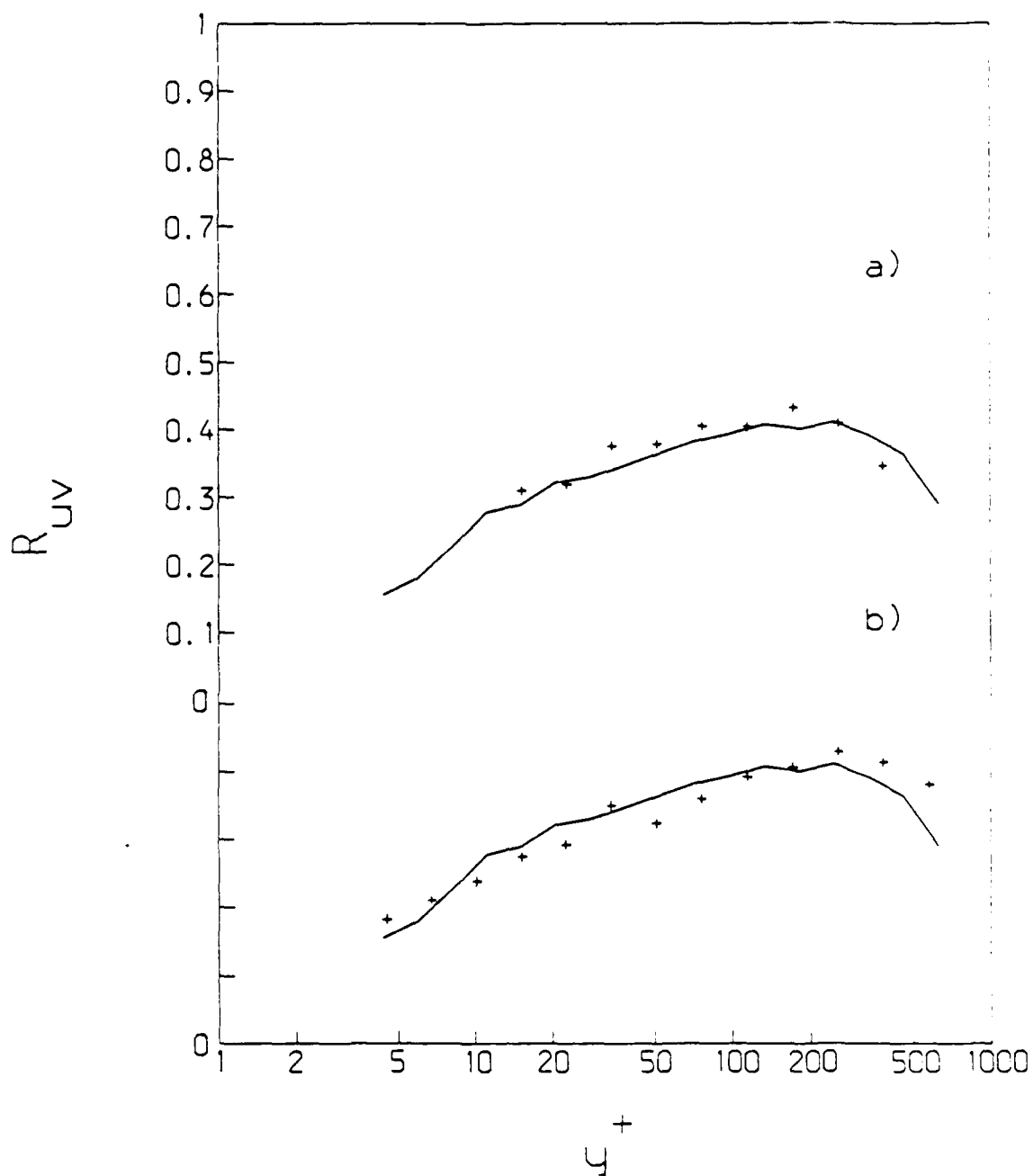


Figure A.13. Correlation coefficient profiles for 6.0 cm channel: a) $\frac{d\bar{U}}{dy}|_w = 1000$ s^{-1} , 5 ppm polymer flow; b) 3 ppm polymer flow; — water flow at equal τ_w .

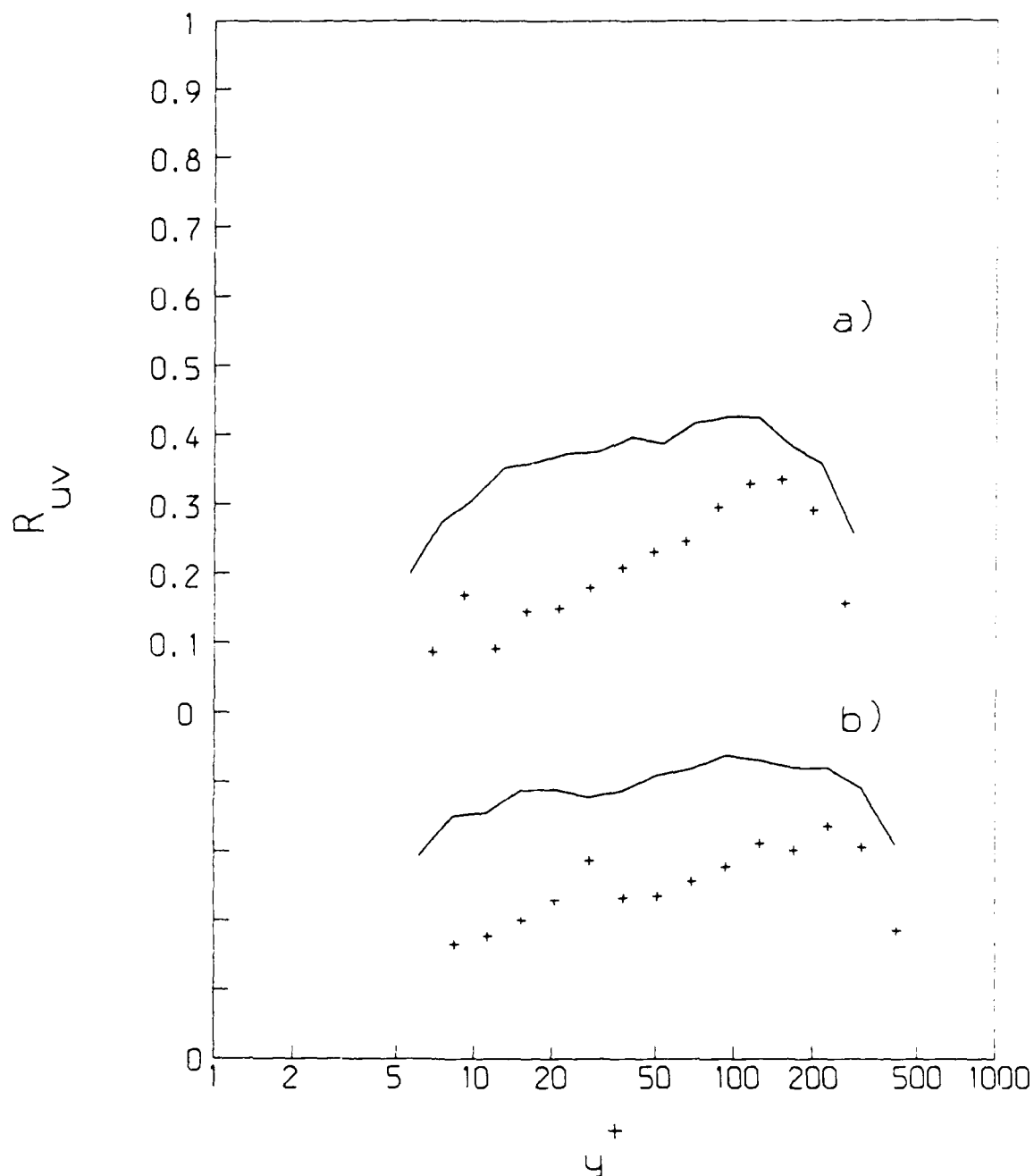


Figure A.14. Correlation coefficient profiles for 2.5 cm channel: a) $\left. \frac{d\bar{U}}{dy} \right|_w = 1000 \text{ s}^{-1}$, 5 ppm polymer flow; b), $\left. \frac{d\bar{U}}{dy} \right|_w = 2500 \text{ s}^{-1}$, 4 ppm polymer flow; —, water flow at equal τ_w .

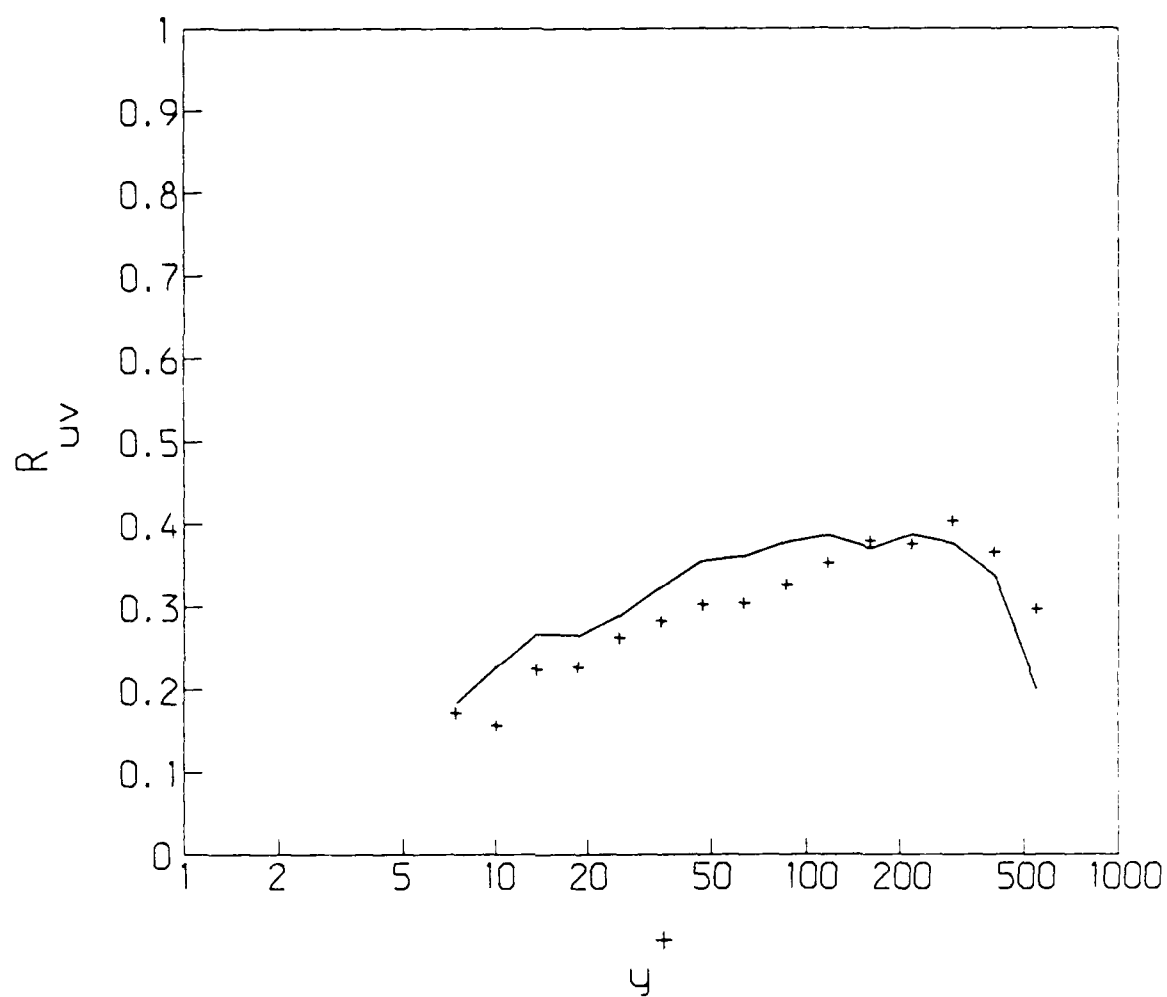


Figure A.15. Correlation coefficient profiles for 2.5 cm channel, $\frac{d\bar{U}}{dy} \Big|_w = 4000$ s⁻¹: +, 3 ppm polymer flow; —, water flow.

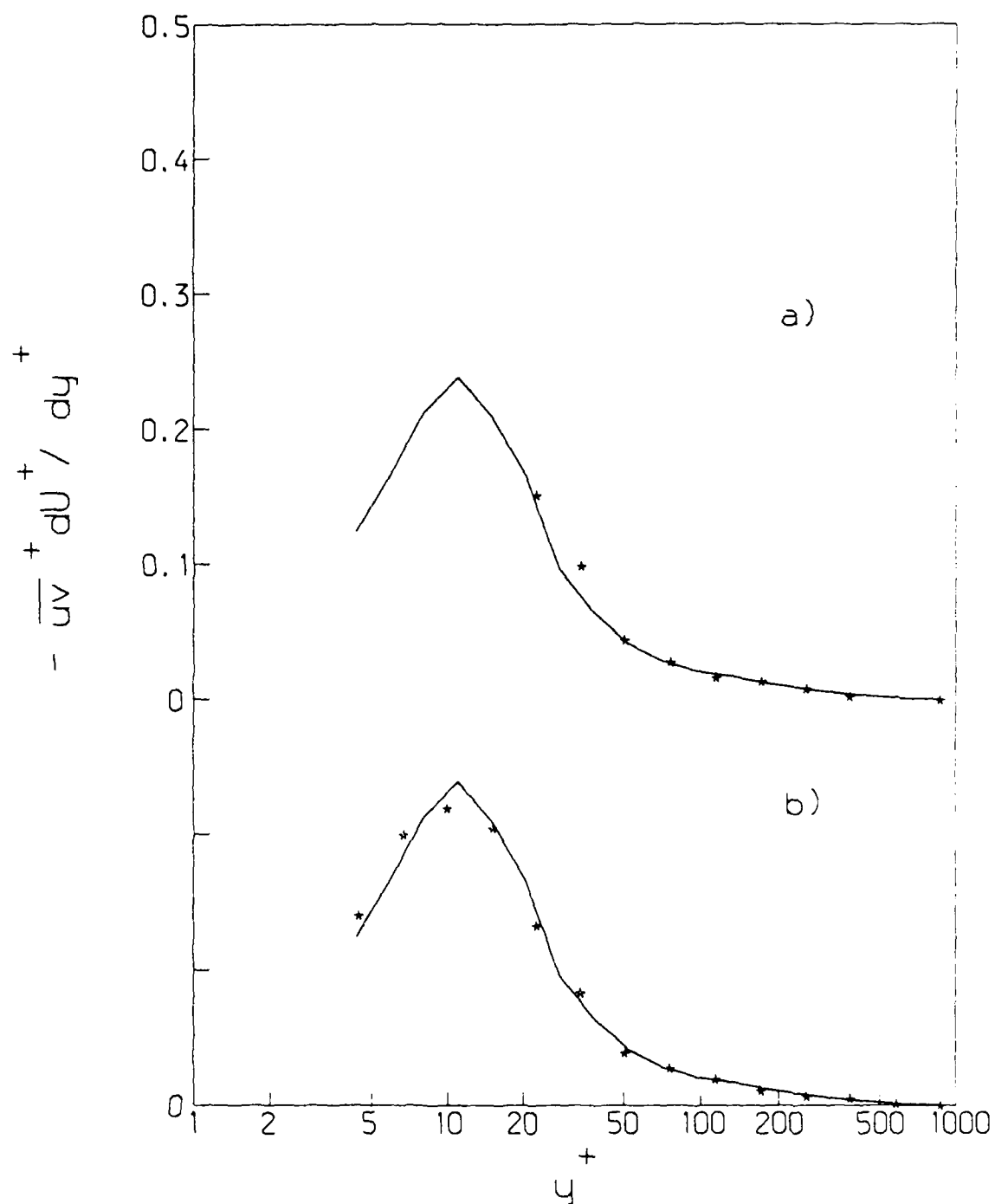


Figure A.16. $\overline{u^2}$ production profiles for 6.0 cm channel, $\frac{d\bar{U}}{dy}|_w = 1000 \text{ s}^{-1}$: a) 5 ppm polymer flow; b) 3 ppm polymer flow; —, water flow.

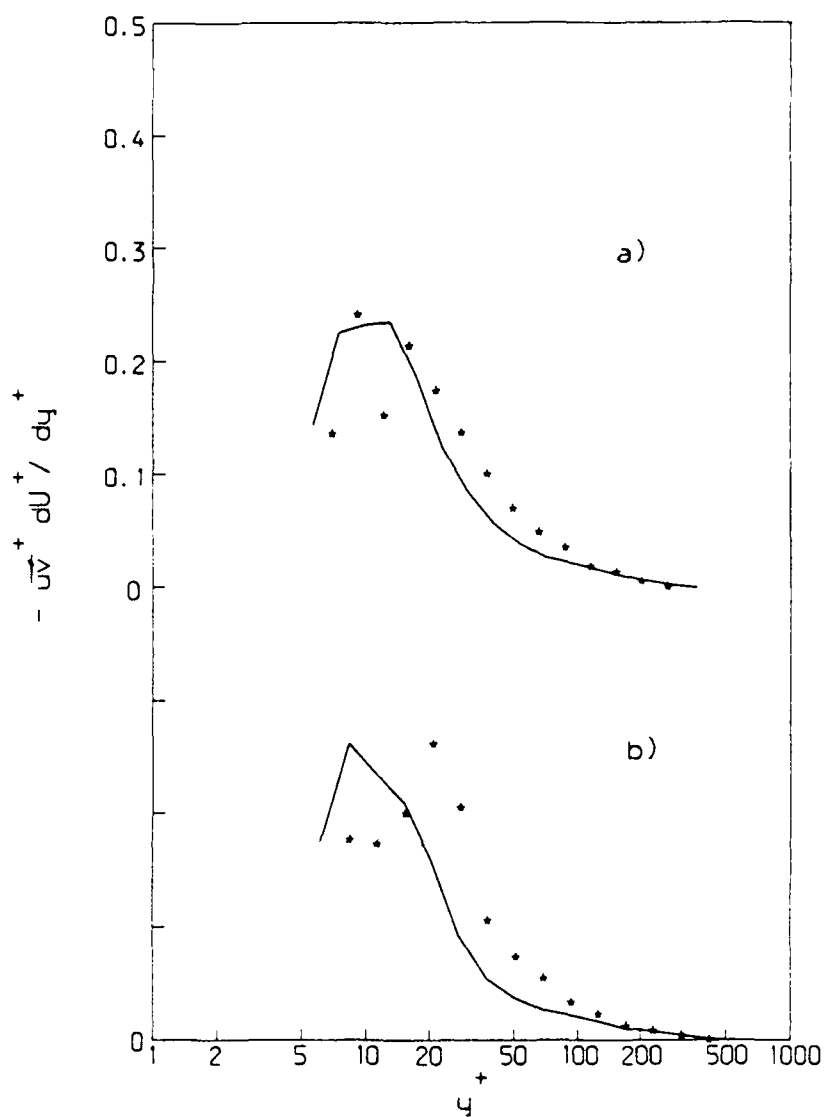


Figure A.17. $\overline{u^2}$ production profiles for 2.5 cm channel: a) $\frac{d\overline{U}}{dy}|_w = 1000 \text{ s}^{-1}$, 5 ppm polymer flow; b) $\frac{d\overline{U}}{dy}|_w = 2500 \text{ s}^{-1}$, 4 ppm polymer flow: —, water flow at equal τ_w .

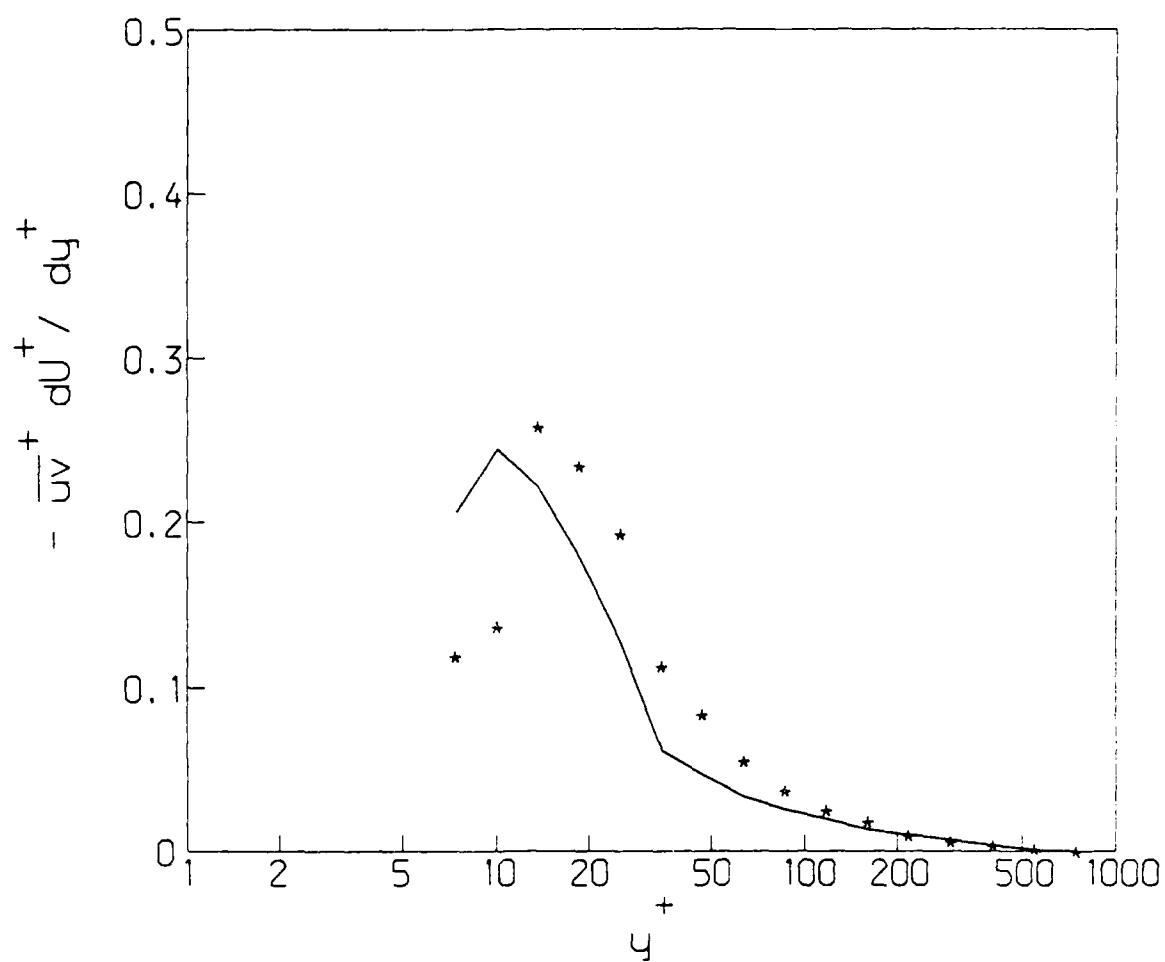


Figure A.18. $\overline{u^2}$ production profiles for 2.5 cm channel, $\frac{d\overline{U}}{dy} \Big|_w = 4000 \text{ s}^{-1}$: * , 3 ppm polymer flow; —, water flow.

DISTRIBUTION LIST

Dr. Michael M. Reischman, Code 1132F
Office of Naval Research
800 North Quincy Street
Arlington, VA 22217

Defense Technical Information Center
Building 5, Cameron Station
Alexandria, VA 22314
(12 copies)

Office of Naval Research
Resident Representative
536 S. Clark Street, Rm. 286
Chicago, IL 60605-1588

Mechanical Engineering Business Office
Purdue University
West Lafayette, IN 47907

Director
Naval Research Laboratory
Attn: Code 2627
Washington, DC 20375
(6 copies)

Professor D.G. Bogard
Department of Mechanical Engineering
The University of Texas
Austin, TX 78712

Dr. O. Kim, Code 6124
Naval Research Laboratory
Washington, DC 20375

Dr. Steve Deutsche
ARL
Pennsylvania State University
P.O. Box 30
State College, PA 16801

Professor S.J. Kline
Thermosciences Division
Department of Mechanical Engineering
Stanford University
Stanford, CA 94305

James H. Green, Code 634
Naval Ocean System Center
San Diego, CA 92152

G. Leal
Department of Chemistry and
Chemical Engineering
California Institute of Technology
Pasadena, CA 91125

Professor T.J. Hanratty
Department of Chemical Engineering
1209 West California Street
Box C-3
Urbana, IL 61801

Justin H. McCarthy
Code 1540
David Taylor Naval Ship R&D Center
Bethesda, MD 20084

Dr. R.J. Hansen, Code 1215
Office of Naval Research
800 North Quincy Street
Arlington, VA 22217

Professor E.W. Merrill
Department of Chemical Engineering
Massachusetts Institute of Technology
Cambridge, MA 02139

E.W. Hendricks, Code 4420
Naval Research Laboratory
Washington, DC 20375

Dr. J.H. Haritonidis
Room 37-461
Massachusetts Institute of Technology
Cambridge, MA 02139

Dr. D.L. Hunston
Polymer Sciences & Standards Division
National Bureau of Standards
Washington, DC 20234

Mr. G.W. Jones
Code 55W3
Naval Sea Systems Command
Washington, DC 20362

Dr. John Kim
M.S. 202A-1
NASA - Ames Research Center
Moffett Field, CA 94035

Dr. C.L. Merkle
Department of Mechanical Engineering
Pennsylvania State University
State College, PA 16801

Dr. T.E. Pierce
Code 63R31
Naval Sea Systems Command
Washington, DC 20362

Steve Robinson
M.S. 229-1
NASA - Ames Research Center
Moffett Field, CA 94035

Professor W.W. Willmarth
Department of Aerospace Engineering
University of Michigan
Ann Arbor, MI 48109